

Letter of Intent for J-PARC Heavy-Ion Program (J-PARC-HI)

J-PARC-HI Collaboration

Spokesperson H. Sako^{*1,2},

J.K. Ahn³, O. Busch⁴, T. Chujo⁴, P. Cirkovic⁵, T. Csörgő^{6,7}, G. David⁸,
D. Devetak⁵, M. Djordjevic⁵, S. Esumi⁴, P. Garg⁹, T. Gunji¹⁰,
T. Hachiya¹¹, H. Hamagaki¹², S. Hasegawa^{1,2}, B. Hong³, S.H. Hwang¹³,
Y. Ichikawa¹, K. Imai^{1,2}, M. Inaba¹⁴, M. Kaneta¹⁵, B.C Kim⁴,
E.-J. Kim¹⁶, X. Luo¹⁷, H. Masui⁴, Y. Miake⁴, J. Milosevic⁵,
D. Mishra¹⁸, L. Nadjdjerdj⁵, S. Nagamiya^{1,11,19}, T. Nakamura¹⁹,
M. Naruki²⁰, K. Nishio¹, T. Nonaka⁴, K. Oyama¹², K. Ozawa²¹,
T.R. Saito^{22,23}, A. Sakaguchi²⁴, T. Sakaguchi⁸, K. Sato⁴, S. Sato^{1,2},
S. Sawada²¹, K. Shigaki²⁵, S. Shimansky²⁶, M. Shimomura²⁷,
M. Stojanovic⁵, H. Sugimura¹, H. Tamura¹⁵, K.H. Tanaka²¹,
Y. Tanaka¹², K. Tanida¹, N. Xu^{17,28}, S. Yokkaichi¹¹, I.-K. Yoo²⁹,

M. Kitazawa^{21,24}, H. Fujii³⁰, K. Fukushima³¹, M. Harada³²,
T. Hatsuda¹¹, T. Hirano³³, K. Itakura²¹, T. Maruyama¹, K. Morita³⁴,
K. Murase³¹, Y. Nara³⁵, C. Nonaka³², A. Ohnishi³⁴, M. Oka^{1,36},

H. Harada², H. Hoshi², J. Kamiya², S. Kato², M. Kinsho²,
A. Kovalenko²⁶, Y. Liu²¹, K. Okabe², M. Okamura⁸, P.K. Saha²,
Y. Shobuda², F. Tamura², J. Tamura², N. Tani², Y. Watababe²,
M. Yamamoto², M. Yoshii²¹, and M. Yoshimoto²

¹Advanced Science Research Center (ASRC), Japan Atomic Energy Agency (JAEA), Tokai, Japan

²J-PARC Center, Japan Atomic Energy Agency (JAEA), Tokai, Japan

³Department of Physics, Korea University, Seoul, Korea

⁴Center for Integrated Research in Fundamental Science and

- Engineering (CiRfSE), University of Tsukuba, Tsukuba, Japan
- ⁵Faculty of Physics and Vinca Institute of Nuclear Sciences, University of Belgrade, Belgrade, Serbia
- ⁶Wigner RCP, H-1525 Budapest 114, POBox 49, Hungary
- ⁷KRF, H-3200 Gyöngyös, Mátrai út 26, Hungary
- ⁸Physics Department, Brookhaven National Laboratory (BNL), Upton, NY, USA
- ⁹Department of Physics and Astronomy, Stony Brook University
- ¹⁰Center for Nuclear Study (CNS), University of Tokyo, Wako, Japan
- ¹¹RIKEN, Wako, Japan
- ¹²Department of Engineering, Nagasaki Institute of Applied Science (NIAS), Nagasaki, Japan
- ¹³Korea Research Institute of Standards and Science (KRISS), Daejeon, Korea
- ¹⁴Department of Industrial Information, Tsukuba University of Technology, Tsukuba, Japan
- ¹⁵Department of Physics, Tohoku University, Sendai, Japan
- ¹⁶Division of Science Education, Physics, Chonbuk National University, Jeonju, Korea
- ¹⁷College of Physical Science and Technology, Central China Normal University, Wuhan, China
- ¹⁸Nuclear Physics Division, Bhabha Atomic Research Centre, Mumbai, India
- ¹⁹High Energy Accelerator Research Organization (KEK), Tsukuba, Japan
- ²⁰Department of Physics, Kyoto University, Kyoto, Japan
- ²¹J-PARC Center, High Energy Accelerator Research Organization (KEK), Tsukuba, Japan
- ²²Johannes Gutenberg University Mainz, Mainz, Germany
- ²³GSI, Darmstadt, Germany
- ²⁴Department of Physics, Osaka University, Osaka, Japan
- ²⁵Department of Physical Science, Hiroshima University, Hiroshima, Japan
- ²⁶Joint Institute for Nuclear Research, Dubna, Russia
- ²⁷Division of Natural Sciences, Research Group of Physics, Nara Woman's University, Nara, Japan

- ²⁸Nuclear Science Division, Lawrence Berkeley National Laboratory,
Berkeley, USA
- ²⁹Department of Physics, Pusan National University, Pusan, Korea
- ³⁰Institute of Physics, University of Tokyo, Komaba, Tokyo, Japan
- ³¹Department of Physics, University of Tokyo, Tokyo, Japan
- ³²Department of Physics, Nagoya University, Nagoya, Japan
- ³³Department of Engineering and Applied Sciences, Sophia University,
Tokyo, Japan
- ³⁴Yukawa Institute for Theoretical Physics (YITP), Kyoto University,
Kyoto, Japan
- ³⁵Faculty of International Liberal Arts, Akita International University,
Akita, Japan
- ³⁶Department of Physics, Tokyo Institute of Technology, Tokyo, Japan

July 25, 2016

Contents

1	Motivation for J-PARC-HI	11
2	Physics goals	12
2.1	Event selection	16
2.2	Leptons and photons	18
2.3	Hadrons	22
2.4	Event-by-event fluctuations	24
2.5	Particle correlations	25
2.6	Collective flow	26
2.7	Charmed hadrons	28
2.8	Hypernuclei	28
3	Extension of hadron and nuclear physics at J-PARC towards high density	29
4	Heavy-ion acceleration scheme at J-PARC	32
4.1	Accelerator design overview	32
4.2	A heavy-ion linac and a booster ring	34
4.3	Heavy-ion acceleration scheme in the RCS and the MR	35
4.4	Simulation in the RCS	36
4.5	Expected beam rate in the MR	38
5	Comparison of J-PARC-HI with heavy-ion projects in the world	40
6	Multi-purpose heavy-ion spectrometer (JHITS)	42
6.1	Physics goals and observables	42
6.2	Detector requirements	43
6.3	Spectrometer design	46
6.4	Silicon vertex trackers (SVT)	48
6.5	GEM trackers	48
6.6	Ring-imaging Cherenkov counter (RICH)	50
6.7	Time-of-flight counters (TOF)	53
6.8	Electro-magnetic calorimeter (EMCAL)	53
6.9	Neutron and anti-neutron detector	54
6.10	Muon tracker system (MUT)	55
6.11	Triggers and centrality counters	57
6.12	Readout electronics and data acquisition system	61
6.13	Radiation tolerance	63
6.14	Beamline and experimental facility	64
7	Expected detector performance and physics results	64

8	Project	71
8.1	International collaboration	71
8.2	Staging strategy and other spectrometer options	71
8.3	Cost estimation	72
8.4	Schedule and R&D plan	73
9	Summary	74
A	An alternative experimental plan : Hypernuclear closed geometry spectrometer	75
B	An alternative experimental plan : Dedicated dimuon spectrometer	77

Abstract

We propose a new experimental program at J-PARC using heavy-ion beams (J-PARC-HI). For this program, we propose upgrading the accelerator complex for heavy-ion acceleration. Our goal is twofold : 1) to study QCD phase structures such as the critical point and phase boundary of the chiral phase transition; and 2) to study the properties of hadrons and nuclei at the densities as high as 5 – 10 times the normal nuclear density created in heavy-ion collisions. Some of the most important studies in this program will involve searching for the critical point using event-by-event fluctuations of conserved charges, and searching for the chiral phase transition using lepton pair measurements. The heavy-ion acceleration scheme is designed based on the use of a new linac and booster ring as a heavy-ion injector, combined with the existing the Rapid-Cycling Synchrotron (RCS) and the Main Ring synchrotron (MR). In this scheme, heavy-ion beams up to uranium will be accelerated to 1 – 20 GeV per nucleon, corresponding to a nucleon-nucleon center-of-mass energy of 2 – 6.2 GeV, possibly at the world's highest beam rate of 10^{11} Hz. A large acceptance spectrometer based on toroidal coils was designed to measure dileptons and hadrons, and their fluctuations and correlations. The design of the spectrometer and the detector complex, as well as their simulation studies are discussed. We intend to produce a detailed budget plan by 2018 to meet the budget proposal in 2019, and we aim to start the first heavy-ion experiment in 2025.

Executive summary

We propose a new physics program using heavy-ion beams at J-PARC. For this program, J-PARC-HI, we propose to upgrade the J-PARC accelerators to utilize heavy-ion beams and perform a heavy-ion collision experiment at the Hadron Experimental Facility, wherein dense matter with baryon density 5 – 10 times higher than the normal nuclear density, which is comparable to the density of a neutron star core, will be created. This experiment will focus on the following main physics objectives:

- exploring a QCD phase diagram, that includes the critical point and the first-order phase transition;
- studying chiral symmetry restoration, including a quantitative understanding of chiral condensate as a function of density;
- determining the properties of quark and hadronic matter at extremely high density, in order to develop, *e.g.*, an equation of state (EoS) of dense matter;
- studying multi-strangeness systems, namely, the production of hyperons, hypernuclei, deeply bound kaonic nuclei, and $|S| \geq 3$ hypernuclei and strange quark matter;
- determining the properties of charmed hadrons in dense matter, which are closely related to the chiral symmetry restoration and diquark correlation in high density environments.

It has been theoretically predicted that the QCD phase diagram in the temperature (T)–baryon chemical potential (μ_B) plane has a first-order phase boundary and a critical point as shown in Fig. 1, although the locations and properties of those have not yet been determined. Therefore, one of the major goals of this program is to determine these phase structures experimentally by utilizing high-intensity heavy-ion beams. Although the creation of quark-gluon plasma (QGP) has been established in high-energy heavy-ion collisions at the Relativistic Heavy-Ion Collider (RHIC) and the Large Hadron Collider (LHC), the medium created by these experiments covers a small μ_B region at which the phase transition to QGP is a smooth crossover. In contrast, a medium with large μ_B can be created in lower-energy heavy-ion collisions. Therefore, J-PARC-HI will open up an opportunity for revealing the phase structures in a large μ_B region.

Another important problem in physics at high baryon density is determining the EoS of quark and nuclear matter at high density, which is relevant to neutron stars and neutron star mergers. The matter created in heavy-ion collisions at J-PARC has a similar baryon density and temperature as that which occurs in neutron star mergers and has baryon density similar to that of neutron star cores. Recently, studies of the EoS in neutron star cores have progressed dramatically through the observation of neutron stars with a mass approximately twice the solar mass. Following the recent observation of the gravitational wave of a black hole merger by the Laser Interferometer Gravitational-Wave Observatory (LIGO), gravitational waves emitted by neutron star

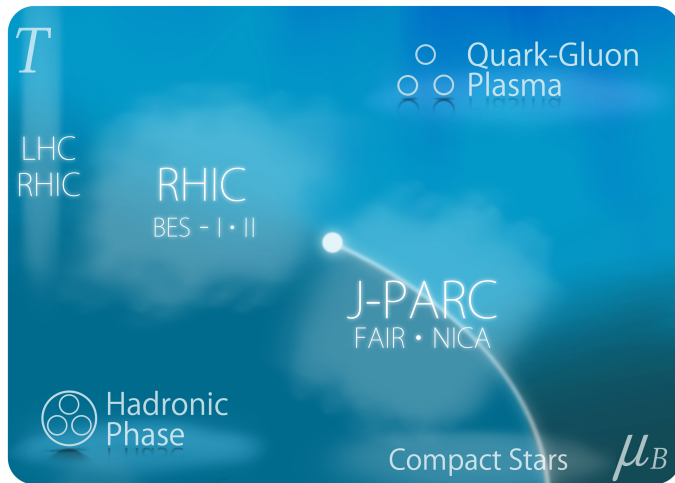


Figure 1: A schematic QCD phase diagram in the temperature (T) and baryon chemical potential (μ_B) plane. Regions that can be explored by heavy-ion collisions at the LHC, RHIC, J-PARC, Facility for Antiproton and Ion Research (FAIR), and Nuclotron-based Ion Collider Facility (NICA) are also shown. The critical point is shown as a filled circle between the RHIC and J-PARC regions, and the first-order phase transition line is shown by a solid line starting from the critical point. Note that these locations are assumptions.

mergers may also soon be observed, allowing the EoS to be studied. This program will therefore be a unique experiment to study the EoS under extreme environments similar to those in neutron star mergers and neutron star cores.

At the current J-PARC accelerators, only protons can be accelerated. By accelerating heavy-ion beams, we can open up new and rich research fields. Ongoing experiments at the J-PARC Hadron Experimental Facility utilize proton and secondary meson beams and measure lepton pairs, hypernuclei, exotic hadrons, baryon-baryon interactions, etc. These experiments are aimed at studying hadron and nuclear properties at a density similar or lower to the normal nuclear density. Using heavy-ion collisions, we will be able to extend these physics to higher baryon densities.

Worldwide, there are several other ongoing or planned heavy-ion programs at around J-PARC energies, including RHIC, NICA, and FAIR. The collision energy range of RHIC is higher than that of J-PARC, while the range of NICA is slightly lower. These experiments will be complementary to J-PARC, which has an energy range similar to that of the SIS-100 synchrotron at FAIR, and both will have extremely high interaction rates. Because of its higher maximum energy and beam rates, J-PARC would have an advantage over the FAIR SIS-100 for heavy-ion experiments.

We propose a heavy-ion acceleration scheme at J-PARC, using a new heavy-ion injector comprising a linac and a booster synchrotron, in addition to the existing the Rapid-Cycling Synchrotron (RCS) and the Main Ring synchrotron (MR), as shown in Fig. 2. The heaviest ions that can be accelerated are uranium ions with a highest energy of 20 AGeV. The high-intensity performance of the RCS and MR, which has

already been established by proton acceleration would enable the acceleration of world's highest intensity heavy-ion beams at the rate of 4×10^{11} per MR cycle. We will operate proton beams for the Material and Life sciences Facility (MLF) and heavy-ion beams for the MR in parallel with the RCS. The heavy-ion beams from the MR will be slowly extracted and transported to the Hadron Experimental Facility via the high-momentum beam line.

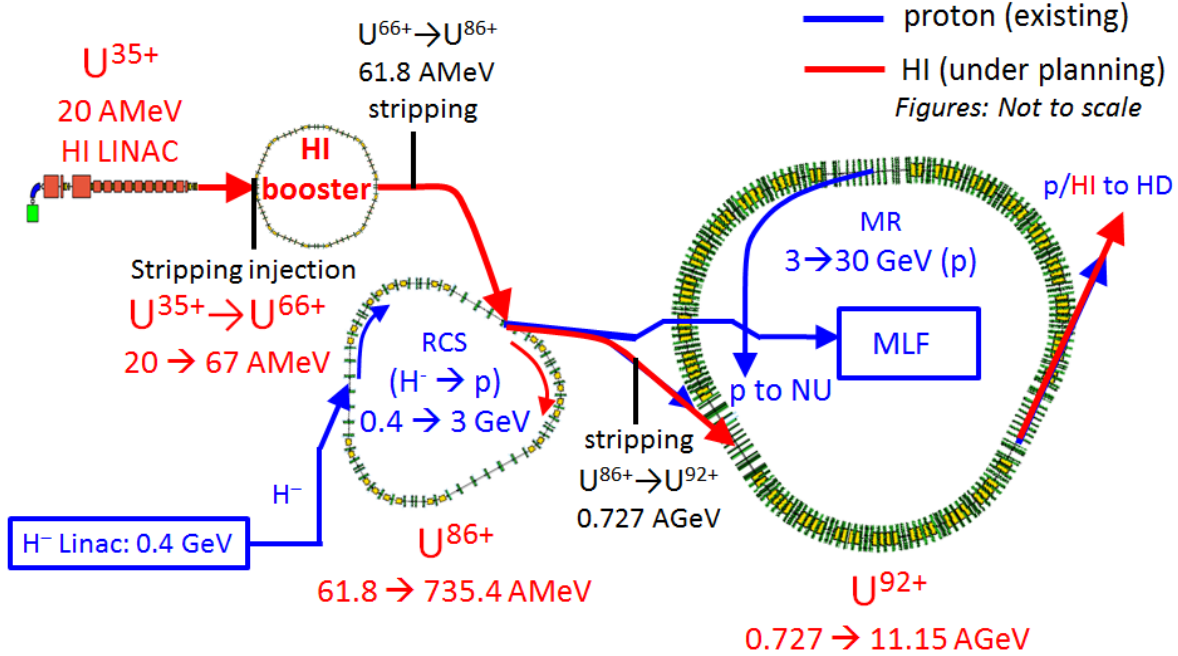


Figure 2: A possible heavy-ion acceleration scheme for adaption in the existing J-PARC facilities. The present J-PARC accelerator scheme and experimental facilities that make use of proton beams are shown in blue; the possible heavy-ion acceleration scheme is shown in red.

In J-PARC-HI, we will search for the QCD critical point by measuring event-by-event fluctuations of conserved charges such as baryon number, electric charge, and strangeness, and search for chiral symmetry restoration by measuring dileptons and charmed hadrons. We will measure collective flow and correlations to study the EoS of dense matter and search for the critical point and the phase transition. In addition, we will measure multi-strangeness hadrons and hypernuclei with strangeness $|S| \geq 2$ and search for strange quark matter (strangelets). These measurements will be made possible by taking advantage of high intensity heavy-ion beams at 10^{11} Hz produced at J-PARC.

In order to produce this variety of physics, we are planning to construct a large acceptance spectrometer for lepton, photon, charm, and hadron measurements. The spectrometer will comprise forward and barrel silicon vertex trackers around the target, a ring-imaging Cherenkov detector, twelve-fold toroidal coils to form the magnetic field along the ϕ -direction, time-of-flight counters, electro-magnetic calorimeters, neutron counters, a muon tracker system, and Gaseous Electron Multiplier (GEM) trackers to

enable precise track reconstruction.

We intend to prepare a budget plan by 2018 to meet the budget proposal in 2019, with the aim of starting the first heavy-ion experiment in 2025.

1 Motivation for J-PARC-HI

Heavy-ion collisions with nucleon-nucleon center-of-mass energies $\sqrt{s_{\text{NN}}}$ higher than a few GeV (*relativistic* heavy-ion collisions) create an extremely hot and dense medium. Heavy-ion experiments in this relativistic energy regime have been performed worldwide over the last three decades at accelerator facilities such as Bevalac, the Alternative Gradient Synchrotron (AGS), the Super Proton Synchrotron (SPS), RHIC and the LHC.

Heavy-ion collisions at the intermediate energy were studied at the AGS in 1986-1995 and have also been studied at the SPS since 1986. After the completion of heavy-ion experiments at the AGS, most of the theorists and experimentalists who studied physics there immediately moved to studies at RHIC (2000-) at the much higher energy of $\sqrt{s_{\text{NN}}} = 200$ GeV in order to search for unambiguous signatures of QGP formation; therefore, they did not have sufficient time to study the dense matter created at the AGS in detail.

The development of an intermediate-energy heavy-ion beam facility has been a long-held dream of Japanese hadron/nuclear physicists. A number of experimental programs have been proposed including several involving the use of intermediate-energy heavy-ion beams. Both the Numatron Project in 1976 and the Japan Hadron Project in 1987 (led by Nagamiya), were canceled. The J-PARC project stopped implementation of a heavy-ion program when KEK's Japan Hadron Facility and JAEA's Research Facility Complex for Neutron Science were unified as J-PARC.

After the AGS experiments terminated in 1998, a modern picture of the QCD phase diagram with a smooth crossover at low baryon density, first-order phase transition, and a critical end point at the high-density region was predicted in a paper by Stephanov *et al.* [1], based on the results by lattice QCD calculations at $\mu_B = 0$. The paper also pointed out that the critical point can be experimentally measured using observables such as event-by-event fluctuations. Unfortunately, the existence of a critical point in the high baryon density region was unknown in the AGS era, and therefore no experimental study aiming at a critical point search was conducted.

In 2010, heavy-ion collisions started at the LHC with $\sqrt{s_{\text{NN}}} = 2.76$ TeV. The regions studied at RHIC and the LHC are at high temperature, but have low baryon density. Many interesting physics phenomena have been observed at these facilities, in particular the formation of QGP [2, 3]. However, no evidence of either a critical point or a first-order phase transition has been found, although many experimental observables at the two facilities support the cross-over transition.

As the properties of QGP have been revealed at RHIC and the LHC, studies of high-density regions with intermediate-energy heavy-ion collisions have begun to attract more attention from theorists and experimentalists interested in conducting a systematic understanding of the properties of QGP and QCD phase structure as a function of collision energy. There are many important subjects left in the intermediate energy region ($\sqrt{s_{\text{NN}}} = 3 - 20$ GeV) for which the J-PARC energy range ($\sqrt{s_{\text{NN}}} = 2 - 6.2$ GeV) is best suited.

Although the previous work at the AGS provided insights into the basic properties of dense matter, further experiments will be required to start to build a deeper under-

standing of the subject. As described above, a search for the critical point through analysis of event-by-event fluctuations should be performed at intermediate energies. Lepton pairs, which are known to be a good probe for studying the properties of hot and dense matter such as chiral transition, thermodynamics, and the EoS of the matter, were not measured at the AGS, although a proposal to do so was put forward there but not approved [4]. Studies at J-PARC using the latest experimental technology and much higher statistics would therefore be a useful bridge to better understand the dense matter.

In this letter of intent, we propose a new program using heavy-ion beams at J-PARC (J-PARC-HI). At present, the synchrotrons at J-PARC are used only to accelerate proton beams; the addition of heavy-ion beams at the facility will enrich research. In J-PARC-HI, a fixed target experiment will be performed with heavy-ion beams from the MR at $\sqrt{s_{\text{NN}}} = 2.0 - 6.2$ GeV. An extremely dense medium with baryon density of 5 – 10 times the normal nuclear density is expected to be created at the highest beam energy. Study of the medium’s properties in an extremely dense environment, which would include a search for the critical point and the first-order phase transition of chiral symmetry restoration as well as the development of an EoS relevant to the physics of neutron stars and neutron star mergers, would be one of the central subjects of this program.

Taking advantage of the high performance of the accelerators and the fixed-target experiment, the J-PARC-HI would be able to achieve the highest collision rate of all existing and past heavy-ion experiments. Precise measurements of a variety of observables for the first time at J-PARC-HI will produce reveal an abundance of new physics in various research fields.

Several other heavy-ion projects are currently operating or planned at intermediate energy ranges. The collider experiments with $\sqrt{s_{\text{NN}}} = 7.7 - 60$ GeV known as the beam-energy scan (BES) program at RHIC have been completed through their first stage, and a second is planned at a tenfold higher luminosity [5, 6]. Other experimental programs to perform fixed-target and collider experiments at $\sqrt{s_{\text{NN}}} = 2 - 10$ GeV are planned at FAIR in GSI [7, 8] and at NICA in JINR [9], respectively. J-PARC-HI will have the highest collision rates among these programs, which will enable similar studies to be conducted with higher statistics and utilizing rarer probes. Thus, J-PARC-HI will play a central role in attempting to address the physics challenges that have been discussed in this section.

2 Physics goals

The baryon density of the medium created in heavy-ion collisions at J-PARC is expected to reach five to ten times the normal nuclear density (ρ_0). J-PARC-HI will access this extremely dense matter in order to focus, in particular, on the following two main subjects:

1. The search for the QCD critical point and the first-order phase transition of the chiral and deconfinement phase transitions.

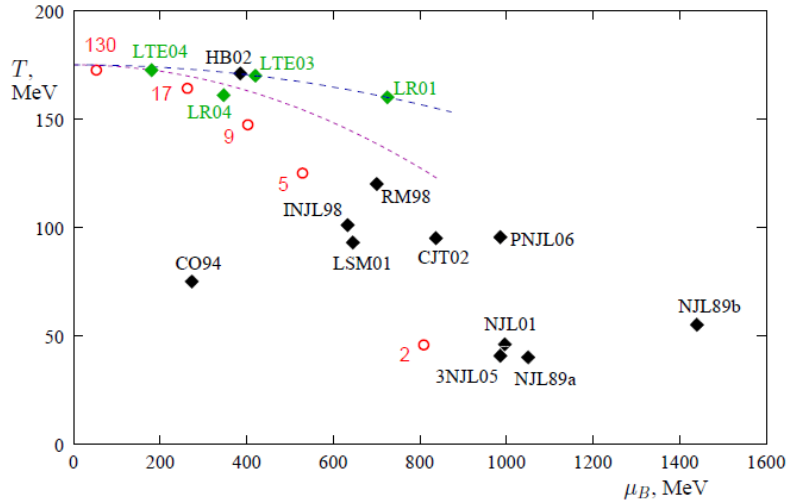


Figure 3: The predicted location of the critical point obtained by various theoretical models (black diamonds) and lattice QCD calculations (green diamonds). Red circles are chemical freezeout points obtained experimentally. See details in [14].

2. The determination of the EoS of a medium with a density higher than ρ_0 , which is relevant to the physics of neutron stars and neutron star mergers.

A strongly-interacting medium is predicted to have various phase transitions at an extremely high temperature T and a high baryon density ρ_B , or a high baryon chemical potential μ_B , as shown in the hypothetical phase diagram in Fig. 1. From lattice QCD calculations, it is known that the phase transition to the QGP from a hadronic medium is a smooth crossover at small μ_B [10]. In contrast, various effective models of the QCD predict that the transition becomes first-order at high μ_B [11]. Therefore, the endpoint of the first-order transition line, *i.e.* the QCD critical point, is expected to be present in the phase diagram as in Fig. 1. It is also conjectured that the medium in a dense environment undergoes various phase transitions to color superconducting [12] and inhomogeneous [13] phases. Unlike the low μ_B region, little is known about the phase structure at high μ_B , where lattice QCD calculations are extremely difficult. Indeed, the location of the critical point predicted by various lattice QCD calculations and models scatters over the phase diagram, as shown in Fig. 3. Therefore, experimental studies of the high-density region, especially a search for the critical point and the first-order transition, are extremely important.

In relativistic heavy-ion collisions, different regions in the phase diagram can be explored by varying $\sqrt{s_{NN}}$. In high-energy heavy-ion collisions at RHIC and the LHC, nucleons in the colliding nuclei pass through each other (“baryon transparency”), because the stopping power for colliding nucleons is not sufficient to decelerate them in the colliding zone. Following collision, matter with high temperature but low ρ_B is created. The QGP was discovered in this type of matter at these facilities.

In contrast, in heavy-ion collisions at J-PARC energies, the initial momenta of

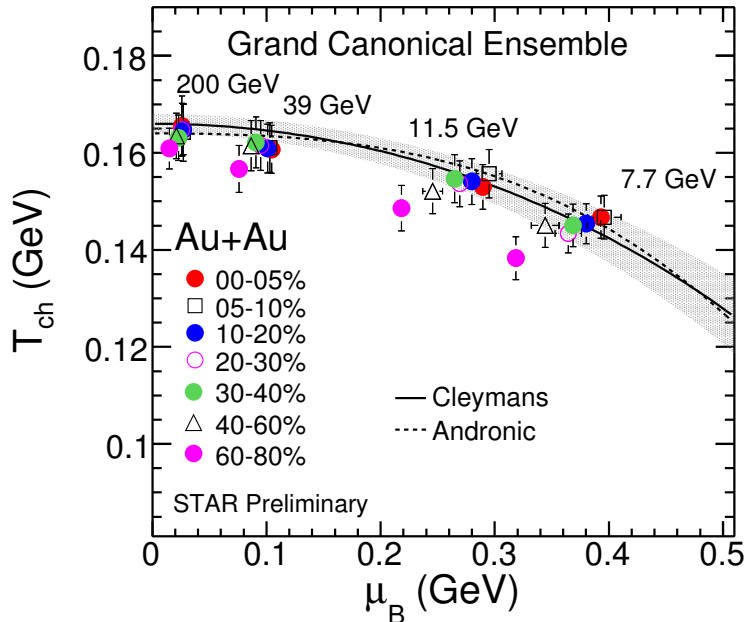


Figure 4: The $\sqrt{s_{\text{NN}}}$ dependence of temperature and baryon chemical potential at chemical freezeout [15].

nucleons produced by nuclei are sufficiently decreased by the interaction that they overlap at the colliding point (“baryon stopping”), producing a medium at high μ_B . In this way, the μ_B of the medium created in the collisions changes depending on the collision energy. This $\sqrt{s_{\text{NN}}}$ dependence of the collision dynamics is clearly observed in the rapidity distribution of the net-proton number [16]. The thermal parameters determined by chemical freezeout shown in Fig. 4 [15] also support the change of the freezeout point in the T - μ_B plane. Experimental studies of the QCD phase diagram are therefore possible by varying the collision energy.

The chemical freezeout picture for hadron yields suggests that the maximum baryon density at freezeout is achieved at $\sqrt{s_{\text{NN}}} = 3 - 5$ GeV [19]. This energy range will be covered by J-PARC-HI. Analyses based on dynamical models indicate that the highest baryon density of $\rho/\rho_0 \gtrsim 5$ at the equilibration time is achieved in collision energies. As an example of such model analysis, we show a time evolution of the baryon density calculated by the JAM model [17] in the left panel of Fig. 5. At the equilibrium time defined as the time when transverse and longitudinal temperatures become similar, the baryon density reaches a maximum of around $5\rho_0$ at $E_{\text{lab}} = 8 - 30$ AGeV, as shown in the right panel of Fig. 5. We remark that this estimation is obtained by a hadronic cascade model (JAM) that does not include the phase transition to a deconfined medium. If the medium undergoes a phase transition, the EoS of the medium should become softer, which makes compression of the medium easier and in turn, leads to a much higher maximum density.

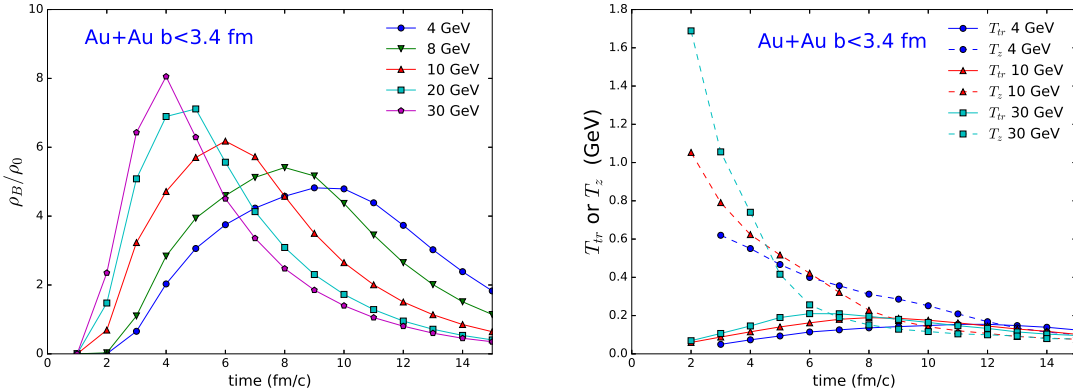


Figure 5: Baryon densities (left) and transverse and longitudinal temperatures (right) as functions of elapsed time from the first overlapping of two nuclei (fm/c) calculated by the JAM model [17, 18] in Au+Au collisions at the beam energies of 4, 8, 10, 20, and 30 AGeV/c.

Compared with higher energy collisions, the dynamics of heavy-ion collisions in the J-PARC energy region, $\sqrt{s_{NN}} \simeq 2 - 6$ GeV, are not well understood. Previous experiments at the AGS measured only hadron production, which did not allow for the extraction of the full evolution of the system and the properties of the created medium. Neither lepton measurement nor fluctuation measurement were performed at AGS. There have also been significant developments in the theoretical and experimental techniques used at RHIC and the LHC for understanding the properties of the hot and dense medium utilizing many observables. Thanks to the progress of accelerator technology and high-rate capability experimental technologies, high-rate heavy-ion experiments at J-PARC will be able to shed light on new physics at high baryon densities by measuring new probes such as fluctuations, photons and leptons, heavy quarks, etc.

Another approach of research at J-PARC-HI will be the experimental analysis of the QCD phase structure. The first-order phase boundary and the critical point are expected to appear in the temperature and density region accessible at intermediate energies. Experimental observation of these landmarks of the QCD phase diagram is an intriguing prospect in relativistic heavy-ion collision experiments. Verification of the threshold collision energy at which the formation of the QGP is realized is another important issue. The intermediate energy of heavy-ion collisions is extremely important for pursuing these goals, which cannot be accomplished at the highest heavy-ion collision energies.

Heavy-ion collisions at intermediate energy ($\sqrt{s_{NN}} \simeq 3 - 20$ GeV) will also become a unique experimental tool for creating and studying dense media with baryon densities of $5\rho_0 - 10\rho_0$, which is comparable to conditions at the cores of neutron stars [20]. The onsets of exotic phases, such as hyperons and strange quark matter, are expected to occur in this region. Understanding the properties of dense media, especially the EoS, is important in constraining the mass-radius relation of neutron stars. Phenomena more

directly connected to heavy-ion collisions at J-PARC-HI include neutron-star mergers, which have recently gained much attention as a source of gravitational waves [21] and as a stage of nucleosynthesis of heavy nuclei [22]. Numerical simulations indicate that the temperature exceeds 100 MeV during neutron-star merger [20, 23]; these temperatures and baryon densities are close to those attained by heavy-ion collisions. J-PARC-HI will thus provide new insights into neutron-star mergers through a “heavy-ion merger” experiment performed on Earth. Although the core of a neutron star is typically cold, with a temperature $T < 10^{-2}$ MeV, J-PARC-HI will also allow us constrain the EoS of this cold nuclear matter.

To explore the properties of dense matter in heavy-ion collisions, it is important to select observables sensitive to the medium properties in the early stage of time evolution. Fortunately, there are various observables in heavy-ion collisions, some of which are relatively sensitive to the primordial stage and some of which reflect the physics around the freezeout time. By combining these, we will be able to deepen our understanding of the overall dynamics of heavy-ion collisions at the J-PARC energy. In the following sections, we describe some of these observables and explore their relation to the physics at J-PARC-HI.

2.1 Event selection

Utilizing the high interaction rates at J-PARC-HI, we can perform various event selections (either online or offline), in particular, to enhance rare events, which has not been possible in current and previous heavy-ion experiments.

In Fig. 6, we show the event-by-event distribution of the baryon density in the early stage of a collision for the most central collisions at the J-PARC energy calculated using the JAM model [24, 25]. As the figure shows, the baryon density in the early stage has

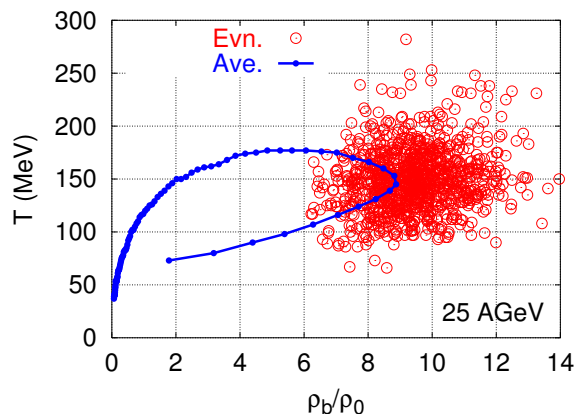


Figure 6: Time evolution of average temperature and baryon density. Circles show the event-by-event distribution just after collision calculated by JAM for $E_{\text{lab}} = 25$ AGeV [24, 25].

large event-by-event fluctuations. This suggests that a “baryon density scan” analysis

is feasible, by classifying collision events with maximum baryon density, *e.g.*, the baryon density dependences of collective flow and photon and dilepton production will provide crucial information on the EoS of dense media, chiral condensate as a function of baryon density, and the existence of the first-order phase boundary. The fluctuation of the density shown in Fig. 6 should be much more amplified if the medium undergoes first-order phase transition, which is not considered in JAM. It would be useful to measure neutrons to improve the quality of the fluctuation measurements. Another possible measure to use for event selection is the production yield of strangeness, as this would enable the analysis of the strange chemical potential dependence of the EoS.

Selection of events with an extremely high baryon number or strangeness will cause the system to shift towards a higher density, as shown in the phase diagram in the left plot of Fig. 7. If the system is sufficiently close to the phase boundary, it could cross the phase boundary as a result of such event selection, in which case the $\sqrt{s_{NN}}$ dependence of the mean transverse energy should change dramatically, as shown in the right plot of Fig. 7. The mean transverse energy may have a clear non-monotonic dependence that signals the phase transition.

To perform the above analyses, a large number of collision events will be indispensable. The high collision rate of J-PARC-HI will make it best suited to perform such statistics-demanding analyses.

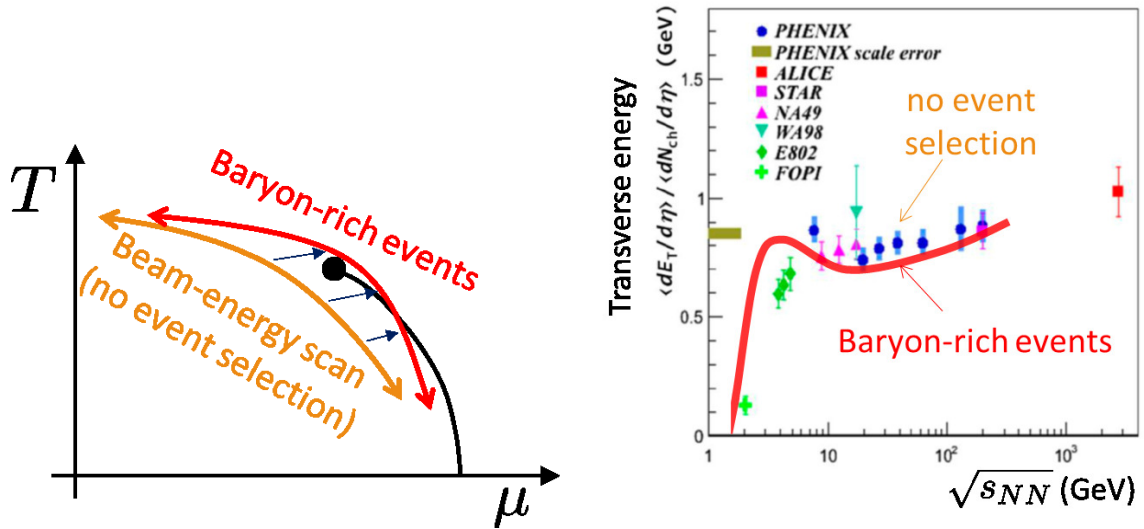


Figure 7: Left: The trajectory of energy dependence of the chemical freezeout point in the QCD phase diagram with (red) and without (orange) event selection with high net-baryon numbers. At the assumed critical point and the phase boundary line, the data cross the phase boundary with event selection. Right: Collision energy dependence of the transverse energy without event selection, with (red) and without (points) event selection with high net-baryon numbers.

2.2 Leptons and photons

Leptons and photons are unique observables in relativistic heavy-ion collisions. Because these particles do not carry color charges, once they are produced in the hot medium, they penetrate it unscathed by strong interactions. Therefore, these observables become a direct signal of medium properties in the early stage of heavy-ion collisions, such as temperature and the degree of freedom of the system. Measurements of these observables will be one of the central tasks in J-PARC-HI. At the AGS, leptons and photons were not measured, while they were measured at the SPS, RHIC, and the LHC. Thus, it will be extremely important to complete the studies of systematic energy dependence of these observables at J-PARC-HI.

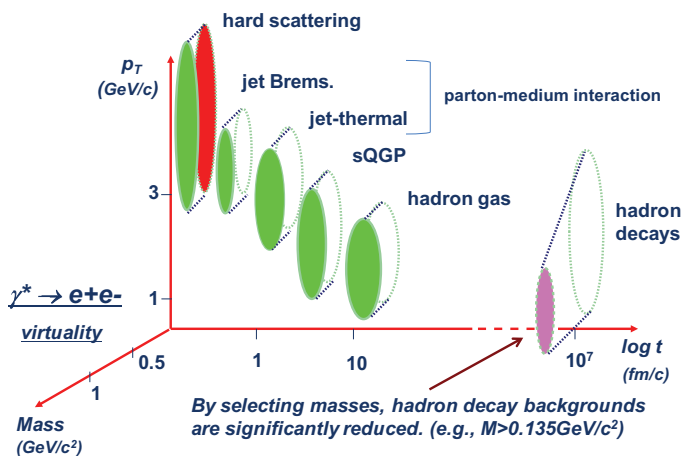


Figure 8: Sources of photons observed at RHIC and LHC energies [26].

We will first discuss the measurement of photons. An important purpose of photon measurements is the observation of thermal radiation of the hot medium. However, other than thermal radiation, there are various contributions to photon radiation produced in relativistic heavy-ion collisions. Figure 8 illustrates the most up-to-date understanding of photon sources as a function of p_T and time t of emission following collision [26]. As shown in the figure, the high p_T photons are dominated by hard contributions, *i.e.* hard scattering and secondary interaction of hard scattered partons. These contributions become stronger as $\sqrt{s_{NN}}$ becomes larger. The isolation of thermal emissions from these components is an important procedure for the measurement of thermal photons especially in high-energy collisions. In Fig. 9, we show the direct photon spectra measured by PHENIX in 200 GeV Au+Au collisions [27] and ALICE [28] in 2.76 TeV Pb+Pb collisions. These measurements were performed using dielectrons from internal conversions of virtual photons at low p_T . The inverse slopes of the spectra for $1 < p_T < 3$ GeV/ c are obtained as 220 MeV for PHENIX [29], and 304 MeV for ALICE [28].

Recently, the second- and third-order anisotropies of the emission angle of photons with respect to the event plane (v_2 and v_3 , respectively) were measured. These flow parameters were found to be positive in $1 < p_T < 3$ GeV/ c and to increase as p_T

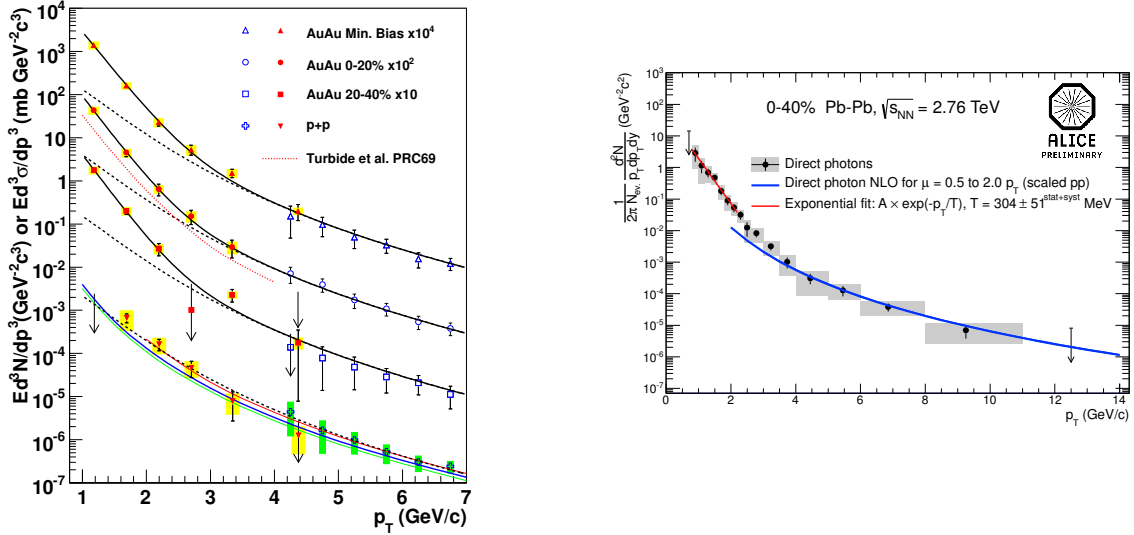


Figure 9: Left : PHENIX results on invariant yields of direct photons in 200 GeV Au+Au collisions at various centralities together with that in $p + p$ collisions. Lines show the N_{coll} -scaled $p + p$ fit functions with exponential functions [27]. Right : ALICE results on invariant yields of direct photons in 2.76 TeV Pb+Pb collisions [28]. These measurements were done using dielectrons from internal conversion of virtual photons at low p_T .

increases. The flow of thermal photons should follow the expansion of the system, and is thus positive. The magnitude of the flow is proportional to the lifetime of the partonic matter.

Under the current theoretical understanding of the flow of thermal photons, they are dominantly produced not in the QGP phase but in the hadronic phase though the rescattering of π and ρ mesons. This clearly indicates that understanding of thermal photon production as a function of collision energy is extremely important for deriving a quantitative model of photon production both in the QGP and the hadronic phases. At J-PARC energies, the background from hard scattering processes should be strongly suppressed. Therefore, photons from the low p_T region ($p_T < 3$ GeV/c) are suitable for the study of medium radiation at J-PARC. The simultaneous measurements of spectra and flow in this experiment will shed lights on their formation mechanism.

Next, we focus on dileptons. Because the invariant-mass spectrum of dileptons is directly connected to the spectral function in the vector channel, various relevant physical phenomena can be studied using this observable. An important physics target among them is the medium modification of vector mesons. In particular, the modification of ρ mesons is a central subject in this field and has long been actively discussed in connection with the restoration of chiral symmetry [30]. These phenomena can be explored by the study of the low-mass region (LMR; $0.15 < m_{ll} < 0.75$ GeV/c², with invariant mass m_{ll}) of the dilepton spectrum.

The STAR experiment recently measured the e^+e^- invariant mass spectra in Au+Au collisions at $\sqrt{s_{NN}} = 19.6, 62.4,$ and 200 GeV as shown in Fig. 10 [31]. STAR observed

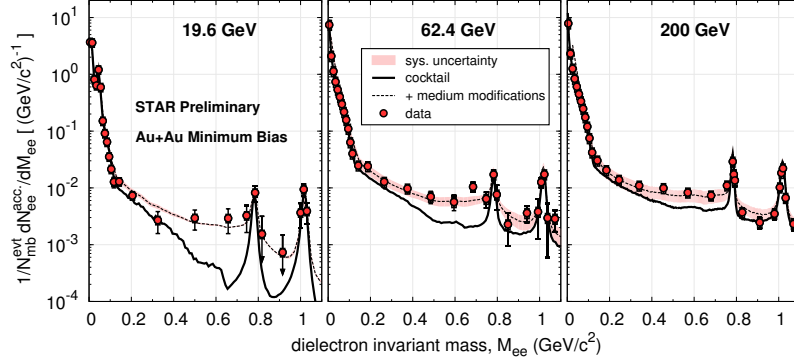


Figure 10: e^+e^- mass spectra measured by the STAR experiment in 19.6, 62.4 and 200 GeV Au+Au collisions, together with cocktail calculations and a theoretical model assuming in-medium modification of the ρ spectral function [31].

a significant excess in the LMR, similarly to that observed at the CERES experiment for Pb+Au collisions at $\sqrt{s_{NN}} = 17.2$ GeV [32]. Based on these experimental results and theoretical analyses [33, 30], we expect larger excess at the J-PARC energy. With the lower collision energies at J-PARC, charm quark production is heavily suppressed resulting in a significantly reduced background in the intermediate mass region ($1.1 < m_{ll} < 2.9$ GeV/ c^2). The main contributor at the intermediate mass region may become thermal radiation from the partonic phase [34]; therefore, we will look for thermal radiation in this mass region.

Figure 11 shows the low mass enhancement factor, which is the ratio of the measured dilepton yield to the cocktail, from known hadron decays in the low-mass region. Obtaining corresponding data in the J-PARC energy range of $\sqrt{s_{NN}} = 2 - 6$ GeV will be extremely important because this region represents the last missing piece needed to complete the energy dependence study. The existing data show a tendency suggesting a maximum in the J-PARC energy range, where the baryon density may also reach a maximum. Precise data from J-PARC and a derived relation to baryon density may reveal insights into chiral restoration.

The dilepton statistics of J-PARC will be the highest produced by all current and past experiments. For instance, the statistics will be higher than CERES data [32] by two to three orders of magnitude. Taking advantage of these high statistics, dilepton measurements at J-PARC will not only have high accuracy but will also allow for the selection of various types of events. Precise data on the centrality dependence of the dilepton production yield, for example, will play a valuable role in discriminating various models describing system evolution. The availability of high-statistics data will also open up new analysis methods, such as the moment analysis of invariant mass. Such a measured moment could be directly related to physical parameters such as quark and gluon condensates via QCD sum rules [35], that could be used as order parameters for the chiral phase transition.

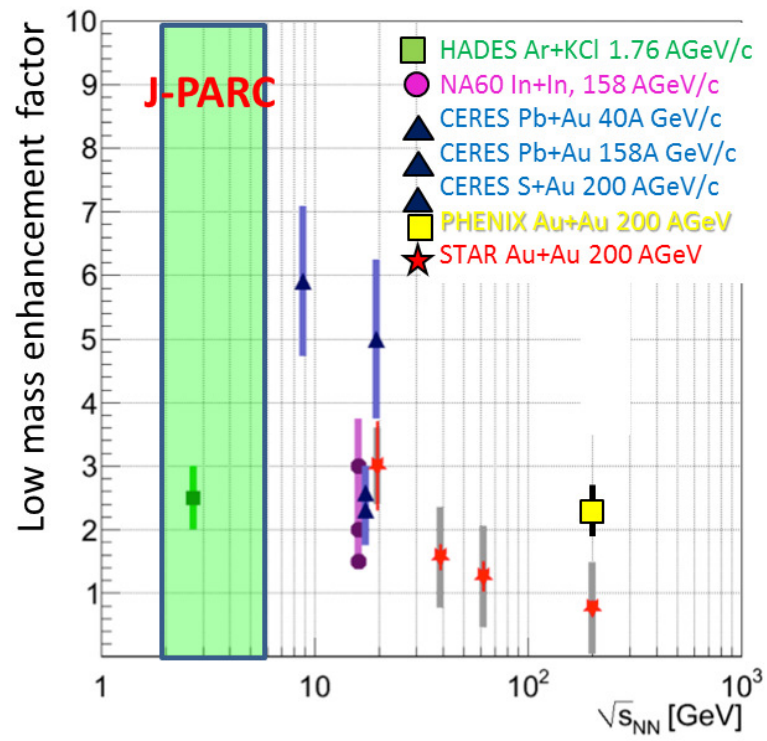


Figure 11: Energy dependence of low mass enhancement factor from GSI-SIS-18 to LHC.

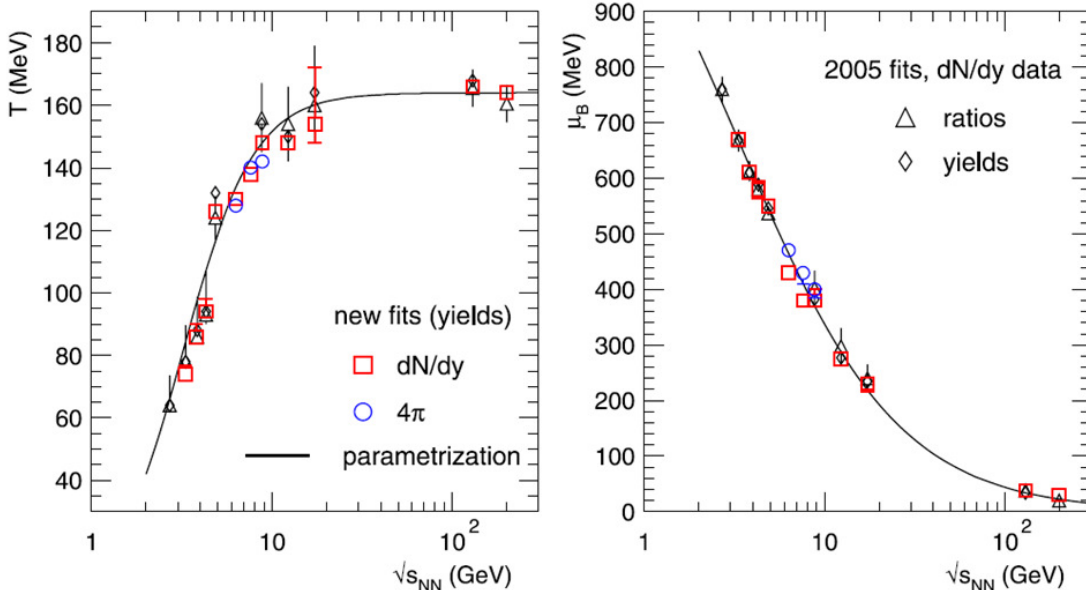


Figure 12: Temperature (left) and baryon chemical potential (right) at the chemical freezeout as a function of the nucleon-nucleon center-of-mass energy [36].

2.3 Hadrons

The abundances of hadrons produced in heavy-ion collisions are important observables. It is well known that the ratios between various particle yields are nicely reproduced by a thermal model with only a few fitting parameters over a wide range of $\sqrt{s_{\text{NN}}}$ from the AGS to the LHC. This result suggests the chemical freezeout picture, namely, that particle yields are fixed in a hot medium under chemical equilibration. From this picture, it is possible to extract T and μ_B at chemical freezeout; as a function of $\sqrt{s_{\text{NN}}}$, as shown in the T - μ_B plane as shown in Fig. 4. The chemical freezeout temperature and the baryon chemical potential are also shown in Fig. 12 as a function of $\sqrt{s_{\text{NN}}}$ [36].

Detailed analysis of the $\sqrt{s_{\text{NN}}}$ dependence of chemical freezeout parameters might enable us to determine a signal of the first-order phase transition and the critical point. From the isentropic time evolution of the created matter, it is known that trajectories on the phase diagram are bent toward the critical point in the T - μ_B plane when the medium passes through the first-order transition line [1]. A similar “focusing effect” is expected to occur even on the crossover side of the QCD critical point [37], although the focusing effect on the crossover side may be a model-dependent phenomena [38]. Therefore, if the critical point exists near the chemical freezeout line, the $\sqrt{s_{\text{NN}}}$ dependence of the freezeout parameters would be affected. A non-monotonic behavior of the chemical freezeout T induced by the critical point has also been suggested [1]. With the current statistics, the $\sqrt{s_{\text{NN}}}$ dependence of the chemical freezeout parameters is smooth as shown in Fig. 12. The errors of the experimental data, however, are still large, especially at the J-PARC energy ($\sqrt{s_{\text{NN}}} = 2 - 6$ GeV), and their centrality dependence is not well understood. More precise measurements of the freezeout pa-

rameters at J-PARC-HI may reveal a signal of the phase transition hidden in the $\sqrt{s_{\text{NN}}}$ dependence of freezeout parameters.

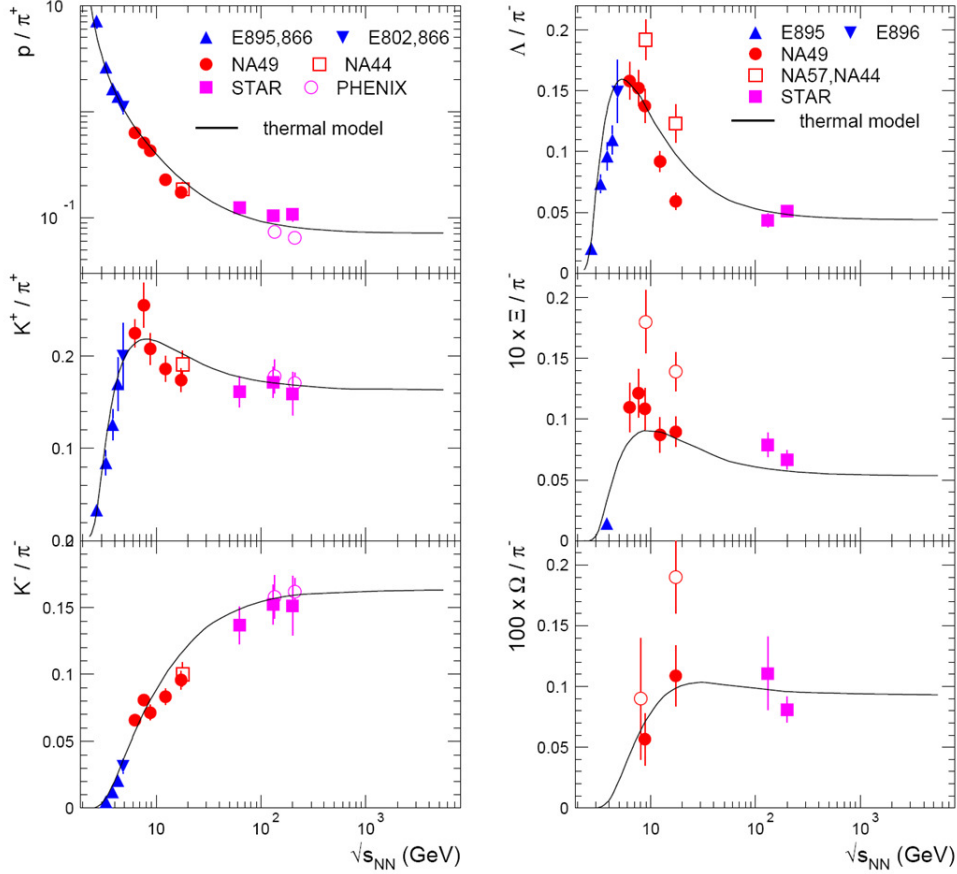


Figure 13: Hadron yields normalized by pion yield as a function of nucleon-nucleon center-of-mass energy (GeV) [36].

The abundances of strange hadrons are further interesting observables that carry information on the dynamics of heavy-ion collisions. For these collisions, a thermal model with a chemical freezeout picture requires an additional parameter representing the pre-equilibrium character of the strange degrees of freedom in order to reproduce the yields of strange hadrons. Because of its non-equilibrium nature, strangeness can be used as an observable to understand the dynamical history of the hot medium, including factors such as the lifetime and density of the medium and its microscopic production mechanism. The abundances of strange hadrons are known to have characteristic behaviors at intermediate collision energies. As shown in Fig. 13, yield ratios K^+/π^+ and Λ/π^- have a peak called the “horn” at $\sqrt{s_{\text{NN}}} = 5 - 10$ GeV. Much conjecture and discussion have connected these structures with the onset of the deconfinement phase transition [36]. The J-PARC energy $\sqrt{s_{\text{NN}}} = 2 - 6$ GeV corresponds to the slightly lower side of the peak. Detailed analyses of yield ratios such as the baryon density dependence in this energy range will provide valuable information to help resolve this

longstanding issue.

Multi-strangeness hyperons are important for understanding the chemical equilibrium of strangeness and may also be sensitive to the formation of the QGP. Thanks to the high intensity heavy-ion beams at J-PARC, detailed studies of Ξ and Ω production that were not possible at the AGS will become feasible in J-PARC-HI.

2.4 Event-by-event fluctuations

Fluctuation observables are important probes that can retain information on the degree of freedom of the QGP phase. In particular, the $\sqrt{s_{\text{NN}}}$ dependence of the event-by-event fluctuations of various conserved charges may be promising observables in the search for the QCD critical point and the onset of the deconfinement phase transition [39]. Recently, non-Gaussian fluctuations of conserved charges characterized by higher-order cumulants have been of particular interest [40]. Analyses of higher-order cumulants of conserved charges are also performed intensively in lattice QCD calculations [10].

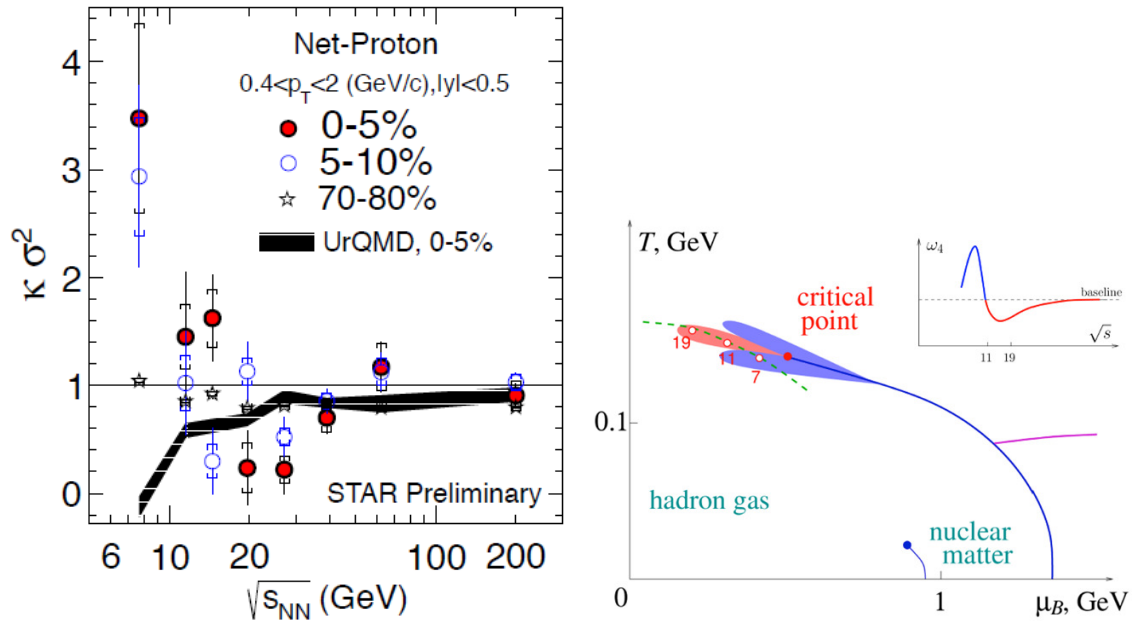


Figure 14: Left : Fourth-order cumulants of the net-proton number as functions of $\sqrt{s_{\text{NN}}}$ (GeV) for different centrality ranges [41]. Right : Theoretical model predictions of fourth-order cumulants near the critical point [42].

In the left plot of Fig. 14, we show experimental results on the fourth-order cumulants, $\langle N_p^n \rangle_c$, of the net-proton number obtained by STAR [43]. In the figure, the cumulant is plotted with the following normalization:

$$\kappa\sigma^2 = \frac{\langle N_p^4 \rangle_c}{\langle N_p^2 \rangle_c}. \quad (1)$$

This ratio should be unity if the fluctuation is consistent with that in the equilibrated hadronic medium. However, the observed cumulant clearly shows deviation from unity, suggesting the existence of non-hadronic or non-thermal effects. In particular, non-monotonic energy dependence is observed with strong enhancement at the lowest energy of $\sqrt{s_{\text{NN}}} = 7.7$ GeV. This behavior is predicted by a model wherein the criticality of cumulants is near the critical point, as shown in the right plot of Fig. 14 [42]. Therefore, measurements of fluctuations at the J-PARC energy ($\sqrt{s_{\text{NN}}} = 2 - 6$ GeV) can be used to conclude whether there is a maximum corresponding to the critical point.

An interesting approach to studying the location of the phase boundary at higher density based on experimentally measured fluctuations of conserved charge has also been proposed [44].

Experimentally, the event-by-event analysis of fluctuation observables requires significant statistics, especially for higher-order cumulants [45, 40]. In this respect, J-PARC-HI is highly suitable for performing the event-by-event analysis of non-Gaussian fluctuations and cumulants at the J-PARC energy ($\sqrt{s_{\text{NN}}} = 2 - 6$ GeV).

Current heavy-ion experiments do not measure neutrons but instead evaluate the cumulants of the proton number as a proxy of the baryon number, resulting in large uncertainties [40, 46]. The event-by-event measurement of neutrons together with protons enables direct analysis of baryon number cumulants. At J-PARC-HI, neutron fluctuations will be measured for the first time.

2.5 Particle correlations

Hanbury-Brown and Twiss (HBT) analysis [47] is used to extract the source size of a hot and dense medium from the momentum correlation between two identical particles. The lifetime of the fireball becomes longest at the phase transition [48, 49], which can be found through HBT analysis. The collision energy dependence of some of the source size parameters from the SPS to the LHC shows a non-monotonic behavior, which some believe to be an indication of the QCD critical point [50]. By measuring the exponent of the HBT correlation functions, one of the critical exponents could be measured if the critical point is close [51]. We can also search for critical opalescence, by finding the maximum of the nuclear modification factor per unit length traversed in the medium [52].

Studies of hyperon-nucleon (YN) and hyperon-hyperon (YY) interactions can provide invaluable information essential for understanding the EoS of dense matter and the interiors of neutron stars. Recently, HBT analysis in heavy-ion collisions was found to be a powerful tool for studying YN and YY interactions because the tool can in principle be used to study any type of particle pair. The left plot of Fig. 15 shows the $\Lambda\Lambda$ correlation function measured by STAR [53]. The measured correlation function is compared to a theoretical model including a $\Lambda\Lambda$ potential, from which the scattering length and the effective range characterizing the $\Lambda\Lambda$ interaction are derived. The extracted parameters are compared to other experimental results in the right plot of Fig. 15. It is interesting that an approach that completely differs from the decay kinematics of a hypernucleus (“NAGARA events”) results in similar parameter values.

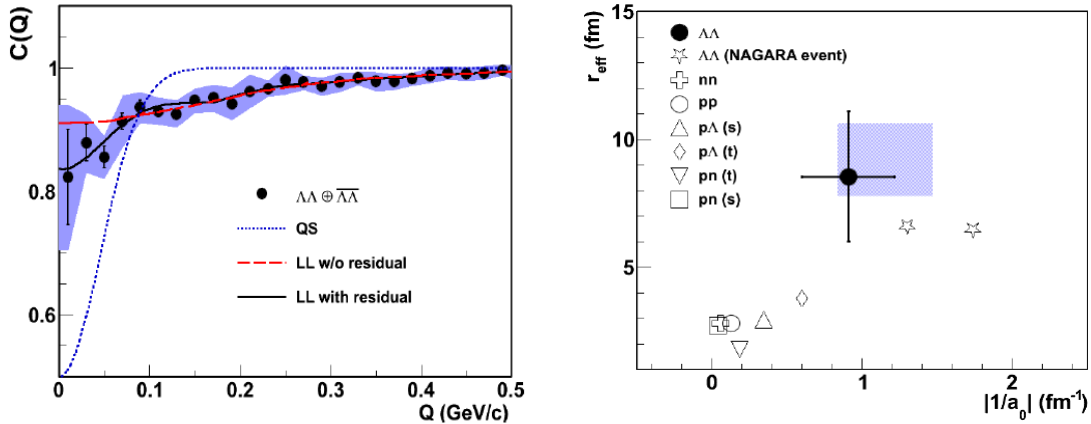


Figure 15: Left: The combined $\Lambda\Lambda$ and $\bar{\Lambda}\bar{\Lambda}$ correlation function measured by STAR (filled circles), where Q is the invariant relative 4-momentum. [53]. Solid and dashed lines correspond to fits using an analytical model. The dotted line corresponds to quantum statistics. See details in Ref. [53]. Right: A plot between the inverse of the scattering length (fm^{-1}) and the effective range (fm) for $\Lambda\Lambda$ by STAR (filled circle), compared to other experimental results for various baryon-baryon pairs [53].

At J-PARC-HI, we will not only improve the statistics of $\Lambda\Lambda$ interaction but will also be able to measure other rarer pairs such as ΞN and ΩN . The feasibility of conducting such measurements at J-PARC-HI will be investigated in near future.

2.6 Collective flow

Collective flow is another basic observable in relativistic heavy-ion collisions. The collective flow carries a wide range of information on the dynamical evolution of the hot medium created by heavy-ion collisions. In particular, the collective flow is tightly related to the EoS in the early stage because the pressure gradient of the medium is one of the sources of the flow. Precise measurements of the flow would therefore provide us with insights into the EoS of the hot and dense medium, which would in turn be directly related to the phase transition and to the physics of neutron stars and neutron star mergers.

The azimuthal distribution of the collective flow is characterized by the Fourier coefficients of particle numbers $dN(\phi)/d\phi$ as

$$\frac{dN(\phi)}{d\phi} = 1 + \sum_{n=1}^{\infty} 2v_n \cos(n\phi), \quad (2)$$

where ϕ is the azimuthal angle with respect to the reaction plane. The first two components representing anisotropy, v_1 and v_2 , are called the directed and elliptic flows, respectively.

At the mid-rapidity $y = y_{\text{cm}}$ in the center-of-mass frame, v_1 vanishes owing symmetry. This quantity, however, can become nonzero at $y \neq y_{\text{cm}}$. The slope of v_1 as a

function of y , $F = \left. \frac{dv_1}{dy} \right|_{y=y_{cm}}$, is a quantity that is widely used to characterize the magnitude of the directed flow. Interestingly, the F of the net-proton number measured by STAR [54] has sign changes at $\sqrt{s_{NN}} \simeq 10$ and 30 GeV in $\sqrt{s_{NN}}$. The relation between negative F and the first-order phase transition has been widely discussed [55, 56, 57]. It is also known that the elliptic flow v_2 changes sign at $\sqrt{s_{NN}} \simeq 5$ GeV [58].

For high energy collisions, v_2 for various particle species is known to obey “quark-number scaling” [59], which is one of the most lucid signals for the formation of the QGP in heavy-ion collisions. Therefore, at J-PARC we would be able to study the energy dependence of quark-number scaling and find the critical energy for the onset of the QGP, where the scaling is violated. The energy dependence of the elliptic flow has been measured by STAR at $7.7 < \sqrt{s_{NN}} < 200$ GeV [60]. Although the violation of quark number scaling in the strange and anti-particle sectors is indicated in this study, many more statistics will be required to see a clear violation.

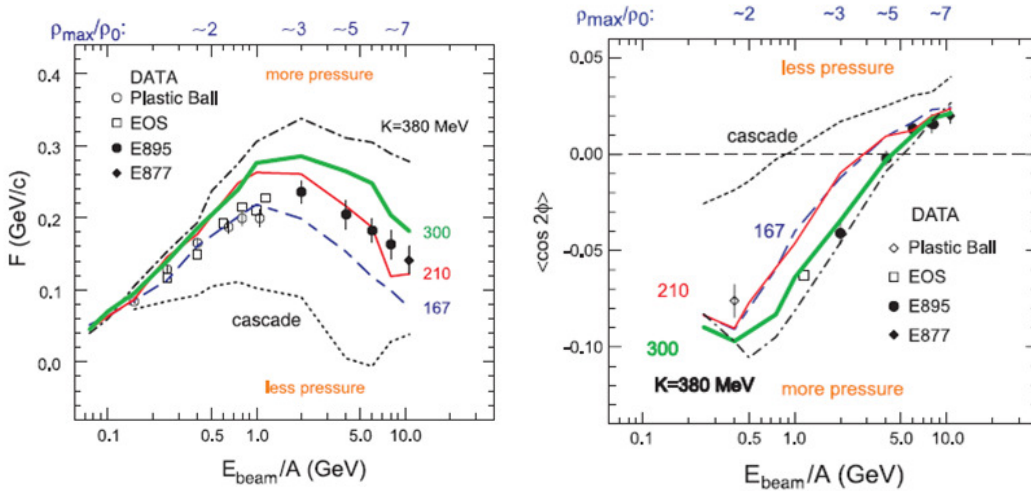


Figure 16: Beam energy dependence of the directed (left), and the elliptic flow (right) of protons, based on a model analysis for various incompressibilities K [61].

Experimental results on directed and elliptic flows can be used to constrain the incompressibility $K = 9dp/d\rho$, which is a crucial parameter of the EoS of dense nuclear matter [61]. The model calculation performed in this study indicated that both the directed and elliptic flows become stronger with larger K as shown in Fig. 16. This monotonic dependence makes it possible to constrain the value of K from flow observables [61]. The precise measurements of the directed and elliptic flows at J-PARC will enable us to proceed further with this type of analysis of the EoS.

It is believed that a very strong magnetic field is created during non-central heavy-ion collisions via two large positively charged ions passing through each other. In non-central heavy-ion collisions at J-PARC, the maximum magnetic field (B) reaches $0.04m_\pi^2$, or 4×10^{16} G, where m_π is the pion mass [62]. This magnetic field exceeds that of neutron stars of $10^{10} - 10^{13}$ G, and that of a magnetar of 10^{15} G [63].

In such a strong magnetic field, parity-violating domains could possibly be formed in systems with chiral symmetry restoration such as the quark-gluon plasma [64, 65]. Experimentally, electric-charge dependence and/or separation of azimuthal anisotropic flow and correlation with respect to the reaction plane has been observed in heavy-ion collisions [66, 67]. Baryon-charge separation across the reaction plane would also be expected from the chiral vortical effect caused by hydrodynamic fluid with vorticity and baryon chemical potential. These effects, *i.e.* the chiral magnetic effect (CME) [64], chiral magnetic waves (CMW) [68], and the chiral vortical effect (CVE) [69], are being studied actively at RHIC [70, 71] and LHC [72] energies. The beam energy and centrality dependence of these signals is an important tool for investigating the phase transition to the QGP and to search for the critical point in the QCD phase diagram.

2.7 Charmed hadrons

A charmed quark pair ($c\bar{c}$) produced in the initial stage of a heavy-ion collision may be sensitive to the properties of the hot and dense medium in which they propagate. It is also interesting that the D meson mass can change at higher baryon densities owing to chiral restoration [73]. As the J-PARC energies are just above the production energy thresholds, the production cross sections are very small. However, with the high beam rates of J-PARC, the expected yields of D mesons and J/Ψ per one-month experimental period are $10^5 - 10^6$ at 20 AGeV/ c (See Fig. 29). We could measure J/Ψ decays into dileptons, and off-vertex hadronic decays and semileptonic decays of D mesons which requires vertex trackers with high-position resolution of several ten μm .

2.8 Hypernuclei

A hypernucleus is a nucleus that contains hyperons *ite.g.* Λ , Σ , and Ξ . Hypernuclei may be an important constituent of neutron stars and could provide information on hyperon-nucleon and hyperon-hyperon interactions. In addition, weak decays of hypernuclei, for instance $\Lambda + N \rightarrow N + N$, could be used to study weak interactions in hadronic many-body systems, which may be different from those in free space.

In the past, hypernuclei have been studied mainly with meson (π and K) [74] or electron beams [75]. However, heavy-ion beams have advantages in terms of hypernuclear production. The goals of hypernuclear research in heavy-ion collisions are summarized as follows.

- Discovery of new hypernuclei and extension of the hypernuclear chart, particularly for $|S| \geq 3$, proton-rich, and neutron rich hypernuclei
- Study of mesonic and non-mesonic weak decays at beam rapidity
- Measurement of the magnetic moment

Recently, the HypHI collaboration at GSI reported hypernuclear production in Li induced reactions [76]. In meson or electron-induced reactions, hypernuclei with $S = -1$ or -2 are mainly produced. As these reactions produce hypernuclei from

the target nucleus, most of the hypernuclei produced in the target rapidity region are similar to the target nucleus.

In contrast, hypernuclei in heavy-ion collisions are produced in the mid-rapidity, target, and beam rapidity regions. In the mid-rapidity region, a few nucleons and hyperons generally coalesce to form a small hypernucleus. As described in Section 3, the yields of hypernuclei in the mid-rapidity region become maximum at around the J-PARC energy. In the target and beam rapidity regions, fragments are embedded with hyperons produced in nucleon-nucleon collisions to form relatively large hypernuclei. Therefore, in heavy-ion collisions, a variety of hypernuclei may be produced at a different sizes, with $S = -1, -2, -3, \dots$ and with different proton/neutron constitutions. Hypernuclei with $|S| \geq 3$ as well as proton and neutron-rich hypernuclei are of particular interest.

In contrast, the presence of background particles makes identification of hypernuclei in heavy-ion collisions more difficult than in meson or electron-induced productions. For mesonic production, the missing mass technique can be used to cleanly reconstruct the hypernucleus mass. For instance, in a (K^-, π^-) reaction the missing mass calculated with the 4-momenta of π^- and K^- corresponds to the produced hypernuclear mass. However, this method cannot be applied to heavy-ion collisions owing to the presence of many background particles, and therefore, weakly decayed particles from a hypernucleus must be reconstructed. The weak decay into π^- and a nucleus (mesonic decay) is commonly used to identify a hypernucleus in heavy-ion collisions [76].

Hypernuclei produced in the beam rapidity region has a momentum close to that of the projectile nucleus. Thus, it flies for a few meters before weak decay owing to a longer lifetime, which is useful for studying weak decays and the magnetic moment. In meson-induced production, the hypernucleus has a small momentum and decays near its production point.

Despite its importance, the hypernuclear magnetic moment has never been measured. The magnetic moment of a hypernucleus is sensitive to its internal hyperon wave functions, its spin and angular momentum structure, and spin-dependent hyperon-nucleon interactions.

In Appendix A, we show a detailed design of a hypernuclear spectrometer for measuring weak decays and magnetic moments at the beam rapidity.

3 Extension of hadron and nuclear physics at J-PARC towards high density

At J-PARC, many types of hadron and nuclear experiments (J-PARC hadron experiments) have been performed or are planned. Experimental and theoretical research related to these is a very active pursuit in Japan and includes hypernuclear studies, search for exotic hadrons, and a dilepton study on chiral symmetry restoration. J-PARC hadron experiments in meson and primary proton-induced reactions have a strong relation to the mission of J-PARC-HI, as they aim to study hadron and nuclear properties at baryon density equal to or less than the normal nuclear density, whereas J-PARC-HI will study them at higher baryon density.

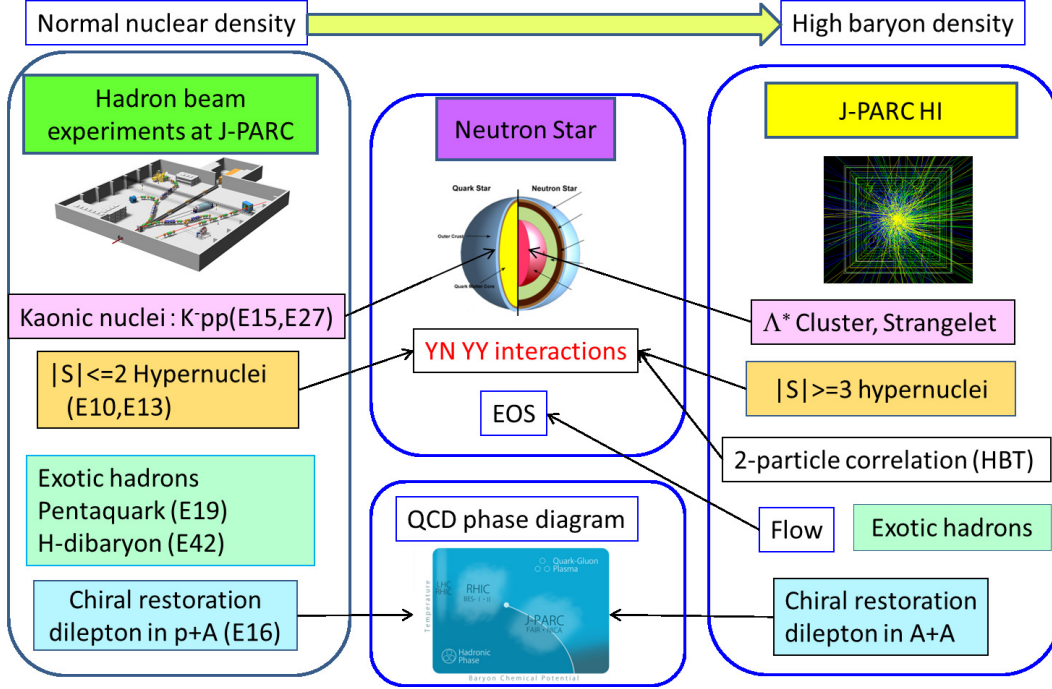


Figure 17: Schematic showing correspondence between hadron nuclear physics using hadron beams and that using heavy-ion beams at J-PARC.

Figure 17 shows the relations between the physics observables that can be measured by the J-PARC and the J-PARC-HI hadron nuclear experiments.

While the lightest Kaonic-nucleus, the K^-pp bound state [77, 78, 79], was studied in J-PARC hadron experiments, larger Kaonic systems of Λ^* matter [80] or light strange quark matter (strangelets) will be searched for at J-PARC-HI.

Hypernuclei with $S = -1$ or -2 [74] are measured or searched for in J-PARC hadron experiments; these will also be measured at J-PARC-HI in addition to $|S| \geq 3$ hypernuclei (see Section 2.8). Hyperon-nucleon (YN) and hyperon-hyperon (YY) interactions from hypernuclei can be studied at the normal nuclear density. At J-PARC-HI, we will be able to study various YN and YY interactions ($Y = \Lambda, \Xi$, and Ω) at potentially higher baryon densities using two-particle correlation analysis as described in Section 2.5.

Studies of kaonic-nuclei, strange quark matter, and hypernuclei at J-PARC-HI could directly relate to the properties of neutron star cores. In addition, we could study the EoS at high densities using collective flow (See Section 2.6).

Exotic particles such as $\Lambda(1405)$ [81], pentaquarks [82, 83], and H-dibaryon [84] are searched for or measured in J-PARC hadron experiments; in addition to these, we can also search for other exotic particles at J-PARC-HI, with the possibility of clarifying their internal structures via production yields (see below). Other exotic particles that could possibly be measured at J-PARC-HI include dibaryons of $\Delta\Delta$ [85], ΞN , and ΩN [86], in addition to other pentaquarks.

Dileptons in p+A collisions will be measured in J-PARC E16 experiment [87], while

dileptons in A+A collisions would be measured at J-PARC-HI, in order to study chiral restoration at normal nuclear density and higher baryon densities, respectively.

Taking advantage of its high collision rate will enable J-PARC-HI to become a powerful experimental facility for studying rarely produced particles such as hyperons, exotic hadrons, kaonic nuclei, and even strangelets [88], and another advantage of the J-PARC energy is its large yields of some of these rare particles.

In Fig. 18, the yields of hypernuclei at the mid-rapidity calculated in a thermal model are plotted [89]. The yields of various hypernuclei, some of which have not yet been observed, have a maximum at around the J-PARC energy.

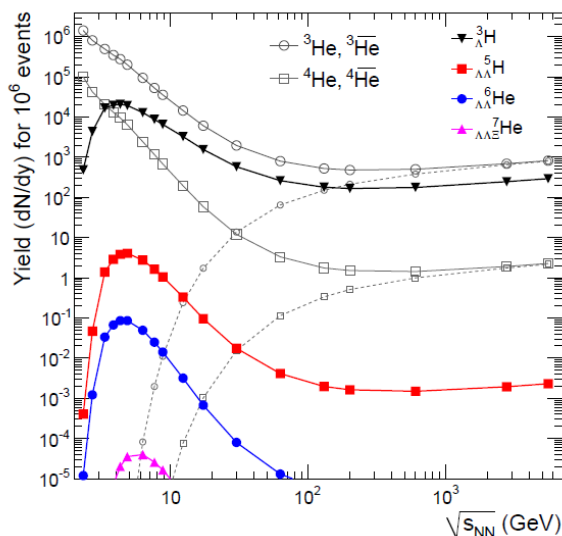


Figure 18: Hypernuclear yields at the mid-rapidity of ${}^3_{\Lambda}\text{H}$, ${}^5_{\Lambda\Lambda}\text{H}$, ${}^6_{\Lambda\Lambda}\text{He}$, and ${}^7_{\Lambda\Lambda\Xi}\text{He}$ calculated by a thermal model as functions of $\sqrt{s_{\text{NN}}}$ (GeV) [89].

The lightest $|S| \geq 3$ hypernucleus is believed to be ${}^7_{\Lambda\Lambda\Xi}\text{He}$ with $S = -4$, while the lightest $S = -3$ hypernucleus is believed to be ${}^{14}_{\Lambda\Lambda\Lambda}\text{C}$ because the third Λ is on the p-shell, which is only bound in a nucleus with $A \geq 11$ [90]. Recently, a resonance state of a tetra neutron ($nnnn$) was observed [91], and the possibility of neutral hypernuclei has also been discussed [92, 93]. These could be observed in J-PARC-HI.

A strangelet is a hypothetical stable or meta-stable (with a weak-decay lifetime) particle comprising almost equal numbers of u , d , and s quarks that was proposed many years ago [94, 95]. Such “strange quark matter” in a macroscopic extension of strangelets could exist inside neutron stars. Many experimental searches have been performed in cosmic rays [96], in terrestrial materials [97], and in heavy-ion experiments [98, 99, 100]. However, no strangelet has been discovered, and the existence of such a particle remains controversial. At J-PARC-HI, we could search for strangelets using the best sensitivities of past heavy-ion experiments.

Kaonic nuclei made of a few nucleons and one or two K^- 's are predicted to be strongly bound [102, 103, 104]. Their yields calculated with a thermal model [101] are

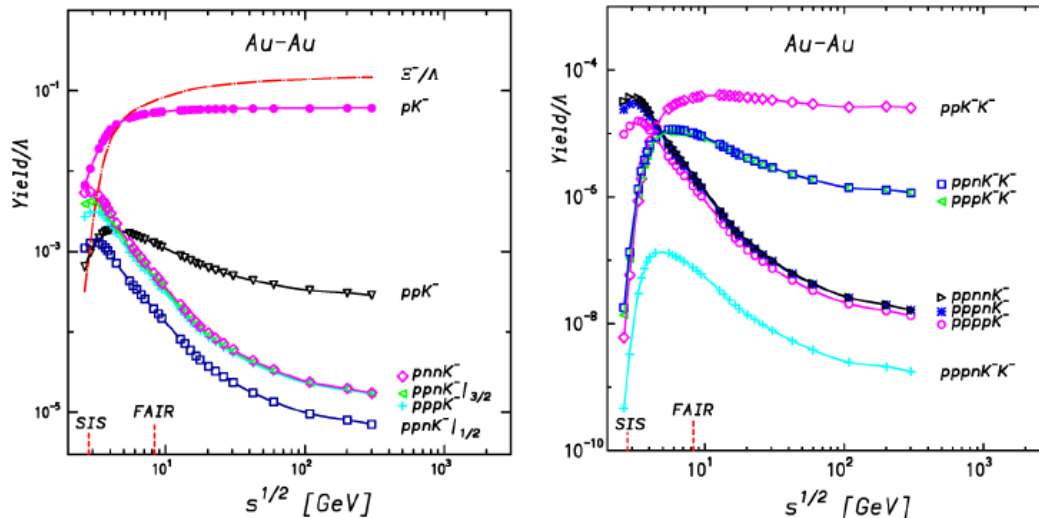


Figure 19: The yields of various kaonic nucleus as a function of $\sqrt{s_{\text{NN}}}$ (GeV) [101].

shown in Fig. 19, which shows that J-PARC-HI could cover the peak energies of both K^- nucleus and K^-K^- nucleus.

In addition to the observation of exotic particles and nuclei, the study of their properties is an intriguing but challenging prospect. One of the most important challenges in hadron physics is the clarification of the internal constitution of exotic hadrons such as $\Lambda(1405)$, which could be either a $\bar{K}N$ molecular state, or a pentaquark state. As the production mechanism of an exotic hadron depends on its internal structure, for example on whether it is in a widely spread hadron molecular-like state or a compact multi-quark state, it would be possible to experimentally determine the internal structure from the production yields. Figure 20 shows ratios of exotic hadron yields assuming various constitutions based on a coalescence model to those of a statistical model at RHIC or LHC energies [105, 106, 107]. The figure shows that the yields of exotic hadrons change drastically depending on their structure, *i.e.* as a hadron molecular, normal hadron, or exotic quark state.

4 Heavy-ion acceleration scheme at J-PARC

4.1 Accelerator design overview

We designed a feasible acceleration scheme for high intensity heavy-ion beams at J-PARC along with the existing proton acceleration scheme as shown in Fig. 2. In order to achieve the required world record of high beam intensity at more than 10 AGeV (GeV/nucleon) for a U^{92+} beam, we aim to utilize the high performance 3-GeV RCS as well as the 50-GeV MR, approaching to the designed beam power for operation [108, 109, 110]. The numerical parameters depicted in the figure correspond to a particular heavy ion species of U^{92+} . Another goal is to accelerate other ion species as interested

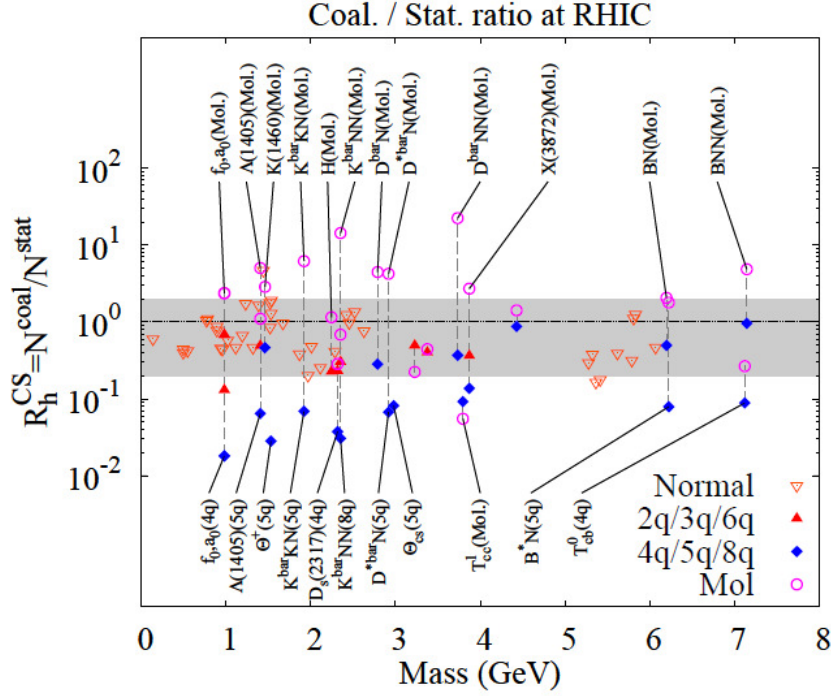


Figure 20: Ratios of yields of exotic hadrons calculated with a coalescence model assuming different constitutions to those of the statistical model. [105, 106, 107]

from the experimental point of view. The existing accelerator facility comprising a 400 MeV H^- linac, the 3-GeV RCS, and the 50-GeV MR (operated at 30 GeV at present).

The RCS simultaneously delivers a 3 GeV proton beam to the MLF and to the MR. The MR operates for either Fast Extraction (FX) for the Neutrino Experimental Facility (NU) or Slow Extraction (SX) for the Hadron Experimental Facility (HD). The MR cycles for FX and SX operation are currently 2.48 s and 5.52 s, respectively, but the cycles will be shortened at least by 1 s from the present values in near future.

The largest advantage of using the RCS and the MR for the heavy-ion acceleration is that we have already understood and optimized performance of each machine for the designed or nearly the designed beam power. The RCS has been already successfully demonstrated an extraction of 1 MW equivalent beam power (8.33×10^{13} /cycle). In the MR, the FX beam and the SX beam power has been reached 400 kW (2×10^{14} /cycle) and 50 kW (0.6×10^{14} /cycle), respectively. Those values are already more than a half and just a half from the designed beam power for the FX and SX operation, respectively. It thus enables us for realistic discussions on beam dynamics issues and measures to aim at the world's most intensive heavy-ion beams. On the other hand, the uses of existing buildings and devices make very much reduction of the construction cost. The primary goal is to achieve a more than 10^{11} U^{92+} ions per MR cycle. Table 1 shows a summary of key parameters and required accelerator performance for the heavy-ion physics program by using U^{92+} beam.

Table 1: Key parameters and accelerator performance for the U^{92+} beam. The numbers in the parentheses are by considering the designed MR extraction energy of 50 GeV for proton.

Parameter	Value
Beam energy	0.727 – 11.2(20) AGeV
$\sqrt{s_{NN}}$	1.9 – 4.9(6.2) AGeV
Beam rate	4×10^{11} (/ MR cycle)
MR cycle	~ 4.5 s
Average beam rate	1×10^{11} (Hz)
Extraction scheme	Slow extraction

4.2 A heavy-ion linac and a booster ring

The present strategy to accommodate a heavy-ion accelerator scheme in J-PARC is by utilizing the existing RCS and the MR without any major modification or upgrade. In order to realize such a condition, we have studied several options for the acceleration design. The best solution so far requires a higher charge state and a higher injection energy as well for the RCS as explained later. The higher injection energy is also useful to achieve a higher extraction energy in order to achieve the maximum yield for the highest charge stage at the final stripping for injecting into the MR.

We propose to newly construct a heavy-ion linac as well as a compact heavy-ion booster ring to connect to the RCS as a heavy-ion injector. We will also have a new ion source dedicated for a high intensity heavy-ion beam of many ion species. Figure 21 shows a design for the heavy-ion linac and the booster ring, both of which can be accommodated in one building of an area only about 3600 m². As for the ion source, a super-conducting ECR (Electron Cyclotron Resonance) is a candidate aiming to produce nearly 10 pμA of U^{35+} beam. The linac has to be designed for acceleration up to 20 AMeV before multi-turn injection into the heavy-ion booster.

The booster plays an important role to achieve the required high intensity heavy-ion beam. It has a four-fold symmetric lattice with the circumference of about 160 m. In contrast to the conventional very limited multi-turn injection scheme of a heavy ion with the same charge state, a charge exchange and practically an unlimited multi-turn injection scheme are under study. It can thus make a flexible condition for the ion source concerning the beam current. The key features of the newly designed heavy-ion booster includes capability of multi-charge states acceleration, a variety of ion species, a variable extraction energy as well as variable extracted beam parameters for suitable beam injection in the RCS. The beam will be accelerated up to nearly 70 AMeV for a U beam.

The merit of having the heavy-ion booster is to reduce the size of the heavy-ion linac in order to achieve a rather high energy of about 70 AMeV for injection into the RCS. The higher energy is required in order to achieve a higher charge state for the RCS injection because of an inadequate vacuum pressure level for lower charge state

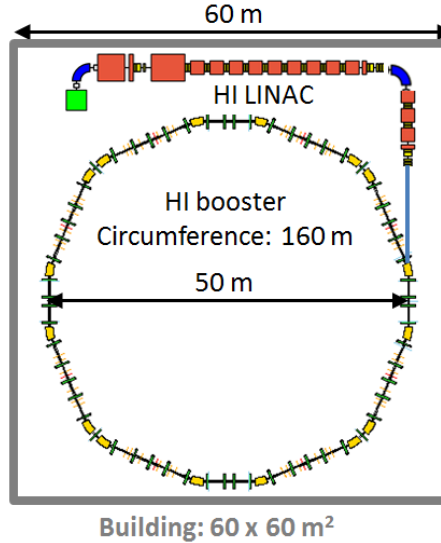


Figure 21: A preliminary design of the heavy-ion linac and the booster ring.

injection. The RCS vacuum pressure level is around 10^{-8} Torr, which is good enough for a proton but limits the lower charge state injection for a heavy-ion in order to avoid any gas stripping in the RCS.

4.3 Heavy-ion acceleration scheme in the RCS and the MR

The RCS plays a key role to satisfy the proposed plan to add a heavy-ion scheme in J-PARC. The RCS has to maintain simultaneous operation with a proton and a heavy ion for the MLF and the MR, respectively, when the MR is operated for the heavy-ion program. Figure 22 shows a layout of the RCS where a heavy-ion injection system is considered to be added at the end of the extraction straight section. However, the heavy-ion injection energy in the RCS has to match the bottom of the magnetic-field cycle pattern determined for the existing 400 MeV H^- case. The main parameters of the RCS, such as magnetic field patterns of the bending and quadrupole magnets, can not be changed from those fixed for the proton beam. If we consider a heavy-ion beam of U^{86+} , the injection energy is calculated to be 61.8 AMeV. The injected U^{86+} will follow the sinusoidal magnetic-field pattern to be accelerated up to 735.4 AMeV.

We consider only one-turn injection from the the booster, which makes a simple injection scheme in order to accommodate within the limited space. The MR however does not require any additional major element except a charge exchange device in the beam transport of the RCS to the MR (3-50BT) for full stripping of the heavy-ion beam before injection into the MR.

Figure 23 shows a RCS beam delivery cycle when the MR operates for the HD experiments (5.52 s cycle). The RCS always accelerates a proton (blue) for MLF users, while either a proton or a heavy ion (red) can be injected in the RCS for the 4 designated MR cycles. Unless otherwise the MR operates with a heavy ion, the RCS as well as the whole accelerator complex runs for a proton as of now. As a result,

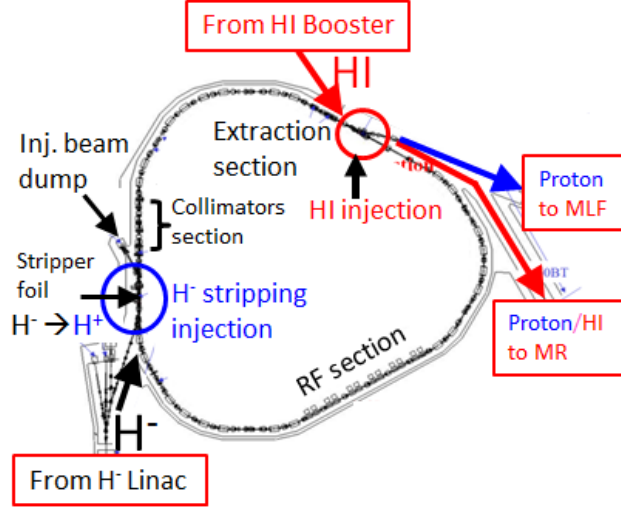


Figure 22: A layout of the J-PARC 3-GeV RCS. The heavy-ion injection system can be added at the end of the extraction straight section.

the upgrade for a heavy-ion beam should not have any conflict with the existing and planned programs that make use of proton beams in J-PARC. The RCS thus should be able to demonstrate acceleration of both a proton and a heavy ion simultaneously.

4.4 Simulation in the RCS

We have performed detailed space charge simulation to demonstrate RCS potential to achieve the required high intensity heavy-ion beam. We used ORBIT code [111] as a simulation tool, which is recently upgraded successfully for realistic beam simulation with space charge including impedance in synchrotrons [112]. Here we present simulation results for U^{86+} acceleration in the RCS. The space charge limit of U^{86+} beam intensity in the RCS can be analytically obtained by calculating the space charge detuning at the injection energy, generally known as the Laslett tune shift (ΔQ) [113] and comparing the value with the designed 1 MW proton beam (4.17×10^{13} particles/bunch). The ΔQ dependence on the beam energy, the ion mass, and the charge state is expressed as following,

$$\Delta Q \propto - \left(\frac{q^2}{A} \right) \frac{1}{\beta^2 \gamma^3} \quad (3)$$

The lower the beam energy, the higher the value of ΔQ because of lower relativistic parameters of β and γ and for the heavy ion we have additionally the first term with the ion charge q and the mass number A . The ΔQ at injection for U^{86+} thus gives a value of more than 300 times larger than that for the proton at the designed 1 MW (4.17×10^{13} particles/bunch). As a result, the bottom line of U^{86+} beam intensity in the RCS can be estimated to be no less than 1.1×10^{11} ions per bunch, which is already one order of magnitude higher than any existing and under construction heavy-ion accelerators in the world.

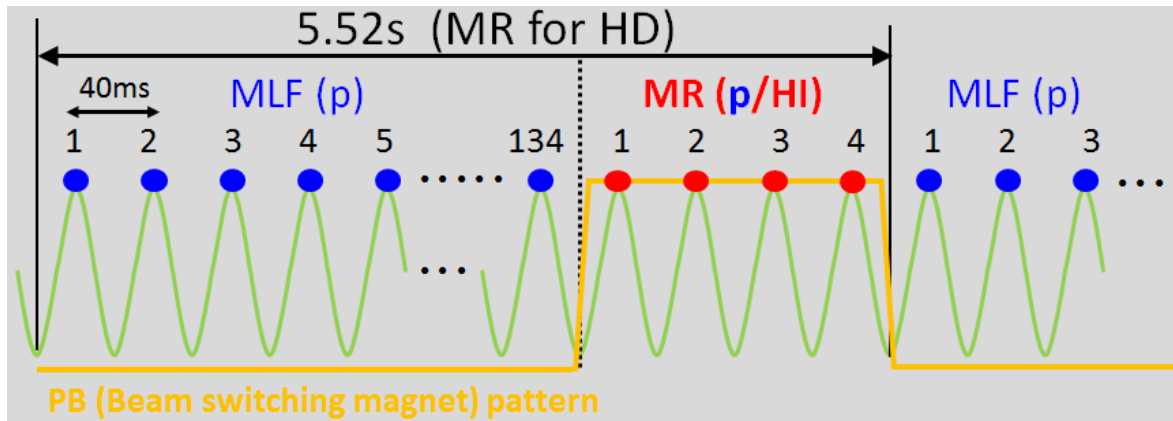


Figure 23: The RCS beam delivery pattern to the MLF and the MR when the MR operates for HD experiments (5.52 s cycle). With adding the heavy-ion scheme in the RCS, either a proton (blue) or a heavy ion (red) can be accelerated in the RCS for the MR cycle depending on MR operation.

As in the practical situation, the bending, quadrupole, and sextupole magnet parameters are kept same as optimized for 1 MW proton beam acceleration. The ramping energy, betatron tunes and the degree of the chromaticity correction are then automatically determined and unchangeable. The injection energy of U^{86+} ion matching the bending magnetic field at the bottom is set to be 0.0618 AGeV, which can be accelerated up to 0.735 AGeV. The horizontal and vertical betatron tunes at injection are set to be 6.45 and 6.42, respectively. Figure 24 (top) shows typical RF voltage patterns for U^{86+} , which are found to be similar to those for a proton and can be changed between cycles. However, the RF system has to be made capable of changing the RF resonant frequency between cycles and/or independent compensation with the beam in each cycle. Similar to a proton, the second harmonic RF voltage is also applied for the present case in order to reduce the space charge effect at a lower energy. The sinusoidal B-field and the corresponding successful acceleration of a single particle U^{86+} ion up to the expected 0.735 AGeV is shown in the bottom plot of Fig. 24.

As detail parameters of the heavy-ion booster are not fixed yet, the transverse and longitudinal beam distributions for RCS injection are considered to be similar to those for protons obtained at the end of injection painting. Figure 25 shows normalized transverse phase space distributions at injection and extraction energies for both horizontal and vertical planes. The emittance at injection was set to be 100π mm mrad, where more than 99.9% of particles at the extraction energy are obtained to be within the collimator aperture (54π mm mrad) at 3-50 BT. Due to relatively smaller aperture and limited capacity of the 3-50 BT collimator, it is very important to have the extracted beam with less halo. Figure 26 shows longitudinal beam distributions along with RF buckets. In order to reduce space charge effect at a lower energy, injected beam is considered to cover nearly 80% of the RF bucket, similar to a proton as obtained at the end longitudinal painting during multi-turn injection.

Figure 27 shows the beam survival studied for 3 different intensities. A more than 99.95% beam survival can be obtained even for injecting 1.1×10^{11} U^{86+} ions in the

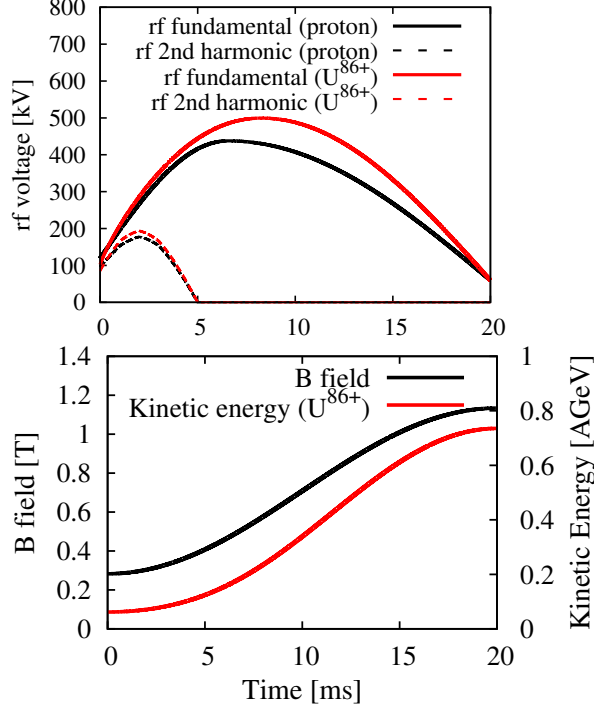


Figure 24: (Top) Typical RF voltage patterns for acceleration of a proton (black lines) and a U^{86+} (red lines) in the RCS are found to be almost similar to each other. (Bottom) The B-field and the corresponding acceleration of U^{86+} as a function of time are shown with respect to the left and right vertical axes.

RCS. Different from the multi-turn H^- charge-exchange injection, there is no stripper foil and beam interaction for the proposed heavy-ion acceleration scheme in the RCS. This results in only a negligible beam losses caused by the space charge effect. As for the 1 MW proton beam, the space charge effect has already been successfully optimized in order to make sure that the remaining beam losses are almost due to the foil-beam interaction during multi-turn injection. The lower the beam intensity, the lower the space charge effect and hence there is practically no beam losses for 2.0×10^{10} U^{86+} ions injection.

The extracted 1.1×10^{11} U^{86+} ions of 0.735 AGeV from the RCS will be fully stripped to U^{92+} in the 3-50BT before injecting into the MR. A total of 4 RCS cycles can be injected in one MR cycle (See Fig. 23). By considering a typical stripping efficiency of 80%, a total of nearly 4×10^{11} U^{92+} ions in principle can be obtained in the MR.

4.5 Expected beam rate in the MR

Similar to the RCS, the space charge limit of the U^{92+} beam intensity in the MR can also be estimated by using Eq. 3. The Laslett value of Q for the U^{92+} at 0.727 AGeV injection energy becomes nearly 600 times as high as that for a proton at 3 GeV injection. Here we may consider the designed proton beam intensity in the MR, which is about 3.4×10^{14} protons/cycle. That gives 750 kW beam power at the designed

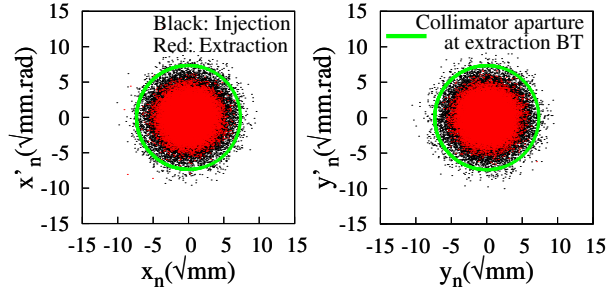


Figure 25: Normalized transverse phase space (black) of a single turn injected U^{86+} beam and the accelerated one at the top energy (red). More than 99.9% of particles at extraction are obtained to be within the 3-50BT collimator aperture as shown as the green circle.

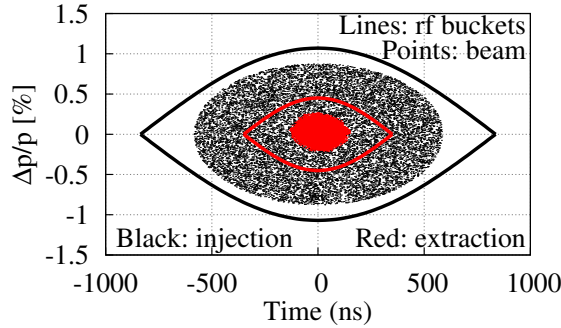


Figure 26: Longitudinal distributions of the U^{86+} beam at injection (black) and extraction energies (red).

50 GeV extraction energy with a repetition rate (cycle) of 3.6 s. It is worth mentioning that the MR extraction energy is 30 GeV at present, while repetition cycles for the fast and slow extractions are 2.48 s and 5.52 s, respectively. The repetition cycles will be reduced by 1 s for both extractions with upgrade of MR magnet power supplies which will be done before construction of J-PARC-HI. One should scale the designed beam power by these two parameters when discussing for the beam power. The beam intensity of 3.4×10^{14} protons/pulse scaled by the Q factor gives an expected U^{92+} beam intensity of about 5×10^{11} /cycle. It can be thus roughly said that a beam intensity of 4×10^{11} delivered by the RCS can be successfully accelerated in the MR and this number of beam rate already satisfies the required beam intensity as shown in Table 1. However, detailed numerical simulations with space charge including beam instabilities have to be carried out for further realistic discussions on heavy-ion acceleration in the MR.

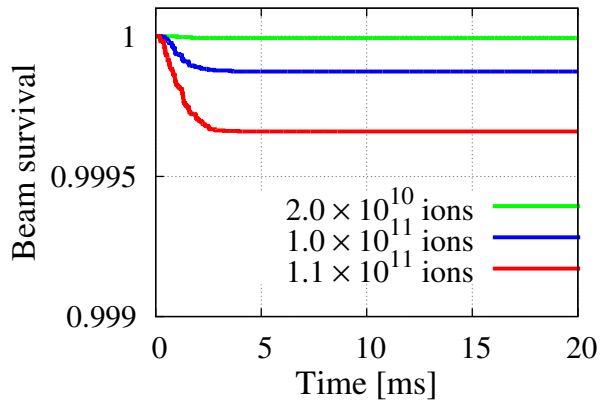


Figure 27: The beam survival probability as a function of acceleration time for 3 different intensities of U^{86+} ions. The injection of even 1.1×10^{11} ions gives a more than 99.95% beam survival.

5 Comparison of J-PARC-HI with heavy-ion projects in the world

In this section, we compare J-PARC-HI with other heavy-ion projects in the world which explore physics of dense matter in the energy range of $\sqrt{s_{NN}} = 2 - 10$ GeV.

In the past, there were fixed target experiments of heavy-ion collisions at the AGS at $\sqrt{s_{NN}} = 2 - 5$ GeV. However, the data-acquisition rate was limited to of the order of one hundred, Only basic properties of hadrons were studied. Neither dilepton nor event-by-event fluctuations was measured.

Figure 28 shows heavy-ion interaction rates as a function of $\sqrt{s_{NN}}$ for heavy-ion projects in the world [114]. It includes the CBM (Compressed Baryonic Matter) experiment with the SIS-100 synchrotron of FAIR [7] project at GSI, collider and fixed target experiments at NICA [9] in Dubna, Russia, NA61/SHINE experiment [115] at the SPS at CERN, and BES (Beam Energy Scan) II program [6] at RHIC at BNL. Table 2 summarizes the parameters of these projects.

Fixed target experiments (J-PARC-HI, SIS-100, and NA61/SHINE) have much higher interaction rates than the collider experiments (RHIC BES and NICA collider). RHIC BES covers a high energy range of $\sqrt{s_{NN}} = 7.7 - 200$ GeV. The first phase of the BES program (BES-I) ended in 2011, and the second phase (BES-II) is planned to start in 2019 with higher luminosity. Among these projects, the interaction rates of J-PARC-HI and the CBM are the highest. The interaction rate of the CBM will be around 5×10^6 Hz, with the average beam rate of 5×10^9 Hz.

J-PARC-HI aims at the world's highest interaction rate of 10^8 Hz, assuming the designed beam rate of 10^{11} Hz and a 0.1% interaction target, which surpasses the CBM by an order of magnitude. Note that this interaction rate does not consider experimental limitation, which should be investigated further.

The $\sqrt{s_{NN}}$ range at J-PARC-HI (2–6.2 GeV) is also wider than SIS-100 (2–5 GeV) at the highest energies, which is advantageous to search for phase structures. The CBM is scheduled to start in 2022, while J-PARC-HI aims to start earliest in 2025.

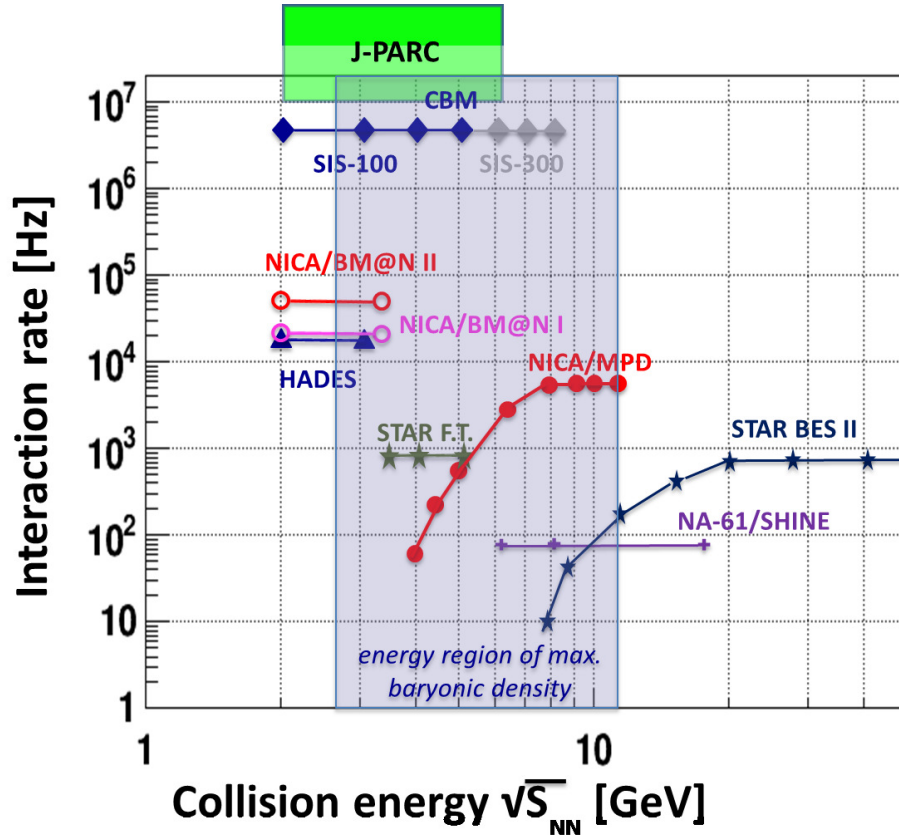


Figure 28: Interaction rates (Hz) as a function of $\sqrt{s_{NN}}$ (GeV) for heavy-ion programs in the world around the J-PARC energy range. [114]

Comparing experimental setups between the J-PARC Heavy-Ion Toroidal Spectrometer (JHITS) and the CBM spectrometer at SIS-100, the advantage of JHITS is the larger backward acceptance ($\theta < 100^\circ$) than that of the CBM ($\theta < 25^\circ$). Especially, it is advantageous for measurements of particles at low beam energies (less than 8 AGeV), event-by-event fluctuations, and target fragments. Another advantage of JHITS is simultaneous measurements of electrons and muons. In the CBM, both electrons and muons cannot be measured at the same time, since the detector configuration must be changed for electron measurements and muon measurements. The setup of JHITS can save beam time, and also some interesting studies with electron-muon correlations such as $D\bar{D}$ production may be possible. JHITS will also measure neutrons in addition to protons, which will improve the sensitivity to the baryon number fluctuations and the event selection with the baryon number.

At higher energies of $\sqrt{s_{NN}} \geq 200$ GeV, the heavy-ion colliders of RHIC and the LHC have studied QGP properties at high temperature and low baryon density in detail. At energies below a few AGeV/c, there are many heavy-ion facilities to study unstable nuclei to extend the nuclear chart for heaviest, neutron-rich, and proton-rich nuclei. Examples of accelerators with high intensity beams are the RIBF (RI Beam Factory) in Japan, the FRIB (Facility for Rare Isotope Beams) in USA, and the RISP

Table 2: Comparison of heavy-ion accelerators in the world. In the fifth column, luminosity is shown for collider experiments, and beam rates are shown for fixed target experiments.

Project	Collider or fixed target	Beam energy (AGeV)	$\sqrt{s_{\text{NN}}}$ (GeV)	Luminosity ($\text{cm}^{-2}\text{s}^{-1}$) or Beam rate (cycle^{-1})	Interaction rate(s^{-1})	Period
J-PARC-HI	fixed	1 – 20	1.9 – 6.2	10^{11}	10^8	2025-
BES-I	coll		7.7 – 200	10^{26} - 10^{27}	$10^1 - 10^3$	2004-2011
BES-II	coll		7.7 – 200	10^{26} - 10^{27}	$10^1 - 10^3$	2019-2020
NA61	fixed	13 – 158	5.1 – 17.3	10^6	10^2	2007-2018
NICA	coll	0.6 – 4.5	4 – 11	10^{27}	$10^2 - 10^3$	2019-
NICA	fixed	0.6 – 4.5	1.9 – 2.4	10^9	5×10^4	2017-
SIS-100	fixed	2 – 11	2 – 4.7	1.5×10^{10}	$10^5 - 10^7$	2022-

(Rare Isotope Science Project) in Korea.

6 Multi-purpose heavy-ion spectrometer (JHITS)

6.1 Physics goals and observables

The main goals of the multi-purpose heavy-ion spectrometer are summarized as follows;

1. Search for the QCD critical point by conserved-charge fluctuations
2. Search for the chiral phase transition from dilepton measurements
3. Study the equation of state of dense matter using collective flow and hyperon-nucleon and hyperon-hyperon correlations

In order to achieve these physics goals, the following observables will be measured in the spectrometer.

1. We will first measure identified hadrons with high statistics systematically in $\sqrt{s_{\text{NN}}} = 2-6.2$ GeV to measure chemical freezeout temperature and baryon chemical potentials. We will measure strange mesons and baryons in detail to study the lower side of peak structures of collision energy dependence of K/π and Λ/π yield ratios [36]. Also, we measure multi-strangeness baryons (Ξ and Ω) to study chemical equilibrium of strangeness. We search for the critical point by measuring event-by-event fluctuations of net-baryon, net-charge, and net-strangeness numbers.
2. We measure dileptons to study the chiral symmetry restoration and evaluate chiral condensate. We measure both dielectrons and dimuons which are complementary in their kinematic coverage. Dielectrons have large background by

external photon conversion by target and detector materials and pion Dalitz decays. Dimuons have large background by pion and kaon in-flight weak decays.

3. We measure direct photons from the hadronic phase and the QGP phase, with internal and external conversion into dileptons, and with real photons by EMCAL. We can examine if the measured temperature is above the critical temperature of the phase transition.
4. We will measure exotic hadrons and nuclei such as hypernuclei, pentaquarks, dibaryons, and kaonic nucleus. We will measure various light hypernuclei, and search for hypernuclei $S = -3$ and strangelets. Note that reconstruction of these exotic hadrons and hypernuclei requires precise secondary vertex resolution.
5. We will measure J/Ψ and D mesons to study their modifications of mass and yields to see the effect of chiral symmetry restoration. Reconstruction of D mesons require more precise secondary vertex resolution.

Fig. 29 summarizes expected multiplicity and production rates of particles and nuclei at J-PARC [7, 89, 116, 117]. At the AGS, only particles/nuclei at the multiplicity more than 10^{-2} were measured, down to antiprotons in charged hadrons, and only ${}^3_{\Lambda}\text{H}$ in hypernucleus. Neither dileptons nor charmed mesons were measured. Assuming the beam rate of 10^{11} Hz at J-PARC, a target with thickness of 0.1% interaction length, the interaction rate is 10^8 Hz. When we select 0.1% most central events, the trigger rate is 100 kHz. In one month of the experiment, we expected to measure $10^7 - 10^9$ dielectron decays of ρ , ω , ϕ , $10^5 - 10^6$ D and J/Ψ at the beam energy of 20 AGeV, and $10^5 - 10^{10}$ hypernuclei. We can also search for $|S| \geq 3$ hypernuclei, and light strangelets and might be able to observe some of them, utilizing the expected world's highest interaction rate of J-PARC-HI.

6.2 Detector requirements

Performance requirements for the heavy-ion spectrometer are listed as follows.

1. A high rate capability is required to cope with high rate beams. Fast detectors such as silicon trackers and MPGD (Micro-Pattern Gaseous Detector) trackers are required. Also, extremely fast readout electronics and a data acquisition system (DAQ) up to 10^8 Hz are indispensable. For such a high data rate, a triggerless DAQ is indispensable as adopted in ALICE and the CBM.
2. High granularity is required for trackers and other detectors in particular at forward angles, due to high multiplicity of charged particles (around 1000) in the central heavy-ion collisions at J-PARC. For instance, a pixel size less than $3 \times 3 \text{ mm}^2$ is necessary to keep the occupancy less than 10% at 1 m distance from the target at the polar angle less than 2° .
3. Large acceptance close to 4π is desired to maximize sensitivity for event-by-event fluctuations and backward physics in the target fragment region.

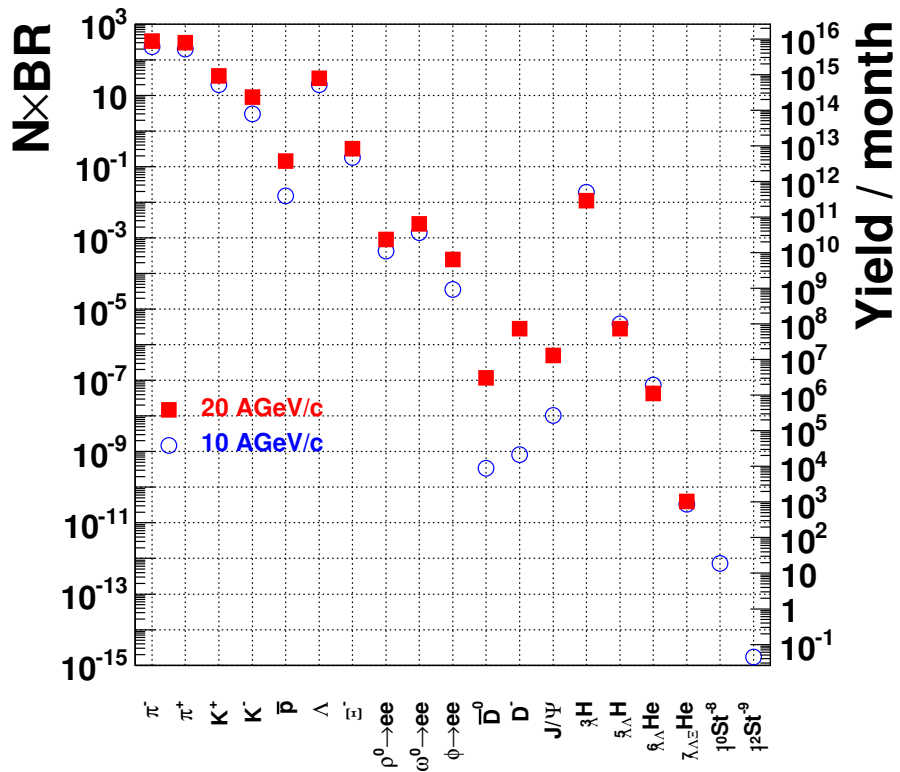


Figure 29: Multiplicity times branching ratio for various particles (left vertical axis) [7, 89, 116, 117] and expected yield at one-month running at J-PARC (right vertical axis) at 10 AGeV/c (blue circles), and 20 AGeV/c U+U collisions.

4. Magnetic-field free volume for the RICH (Ring Imaging Cherenkov detector) for electron identification.

Particle production properties in U+U collisions at the beam energies of 1, 5, and 10 AGeV/c are studied using the JAM model. The rapidity distributions of dN/dy at these energies are shown in Fig. 30. The charged particle multiplicity is about 1200 at 10 AGeV/c, about 930 at 5 AGeV/c, and about 460 at 1 AGeV/c. Note that no K^- is produced at 1 AGeV/c since it is below the energy threshold. The mid-rapidity is 0.5, 1.2, and 1.5 at 1, 5, and 10 AGeV/c.

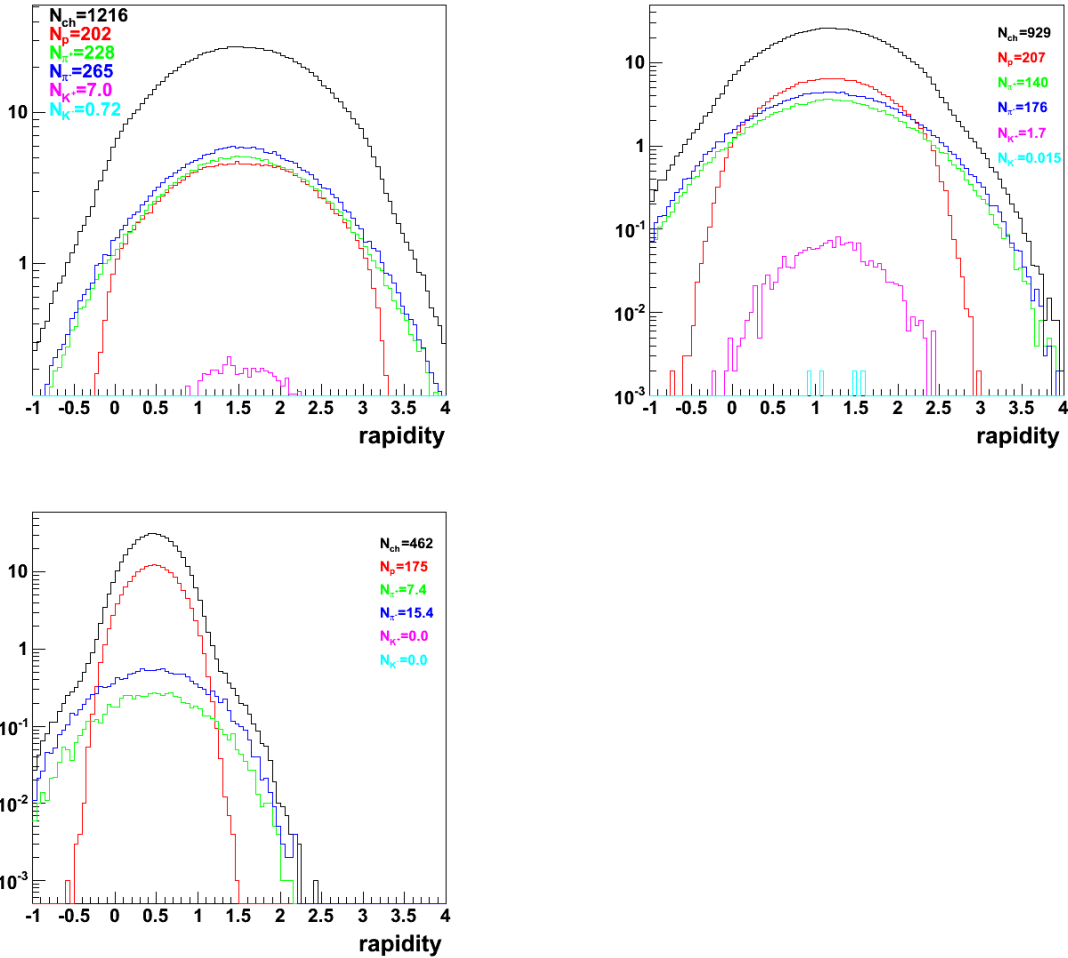


Figure 30: dN/dy of all charged particles (labeled “ch”), p , π^\pm , and K^\pm as a function of rapidity for U+U collisions at 10 AGeV/c (top left), 5 AGeV/c (top right), and 1 AGeV/c (bottom left) simulated by the JAM model.

We studied how much granularity is required for detectors. We calculated how much pixel size corresponds to the particle occupancy of 10% as a function of the polar angle and the results are shown in Table 3.

With J-PARC’s extremely high beam rates, detector operation rates become extremely high, and therefore we should use detectors which have high rate capability.

Table 3: The pad size corresponding to 10% occupancy in U+U collisions at 1, 5, and 10 AGeV/ c at different polar angles at $z = 1$ m downstream from the target.

Polar angle	Pad size at 1 AGeV/ c	5 AGeV/ c	10 AGeV/ c
2°	(15 mm) ²	(5 mm) ²	(3 mm) ²
4°	(15 mm) ²	(6 mm) ²	(4 mm) ²
30°	(25 mm) ²	(21 mm) ²	(19 mm) ²
60°	(53 mm) ²	(47 mm) ²	(46 mm) ²
90°	(140 mm) ²	(91 mm) ²	(91 mm) ²

The ion-ion interaction rate R_{INT} assuming a 0.1% interaction length target and 10^{10} Hz beam rate is 10^7 Hz. Using the estimated occupancy O of 10%/16 mm², the particle rate at the polar angle of 4° at 1 m distance from the target is 63 kHz/mm².

Typical maximum operation rates for a Silicon strip detector, a GEM tracker and a MRPC are 60 kHz/mm², 25 kHz/mm², and 10 kHz/mm² [118]. Depending on the rate capability of each detector and geometry configuration, the pixel size will be determined.

6.3 Spectrometer design

In order to cover large acceptance both for hadrons and leptons, and to make a magnetic-field free volume from the target to RICH, we adopt the spectrometer design based on a toroidal magnet as shown in Figs. 31 and 32 (J-PARC Heavy-Ion Toroidal Spectrometer (JHITS)). The toroidal magnet consists of twelve-fold symmetric thin coils. The coil design is based on that of the CLAS12 experiment at JLab [119]. Except for the dead area due to coils of $\sim 10\%$, the acceptance covers the whole azimuthal angle. Another important advantage of the toroidal magnet spectrometer is the magnetic field free area around the target region for RICH. There is no return yoke for the toroidal magnet, which provides us with the freedom to install detectors at backward angles.

The external conversion of photons by materials produces electron-positron pairs with very small opening angles, which is easily rejected without the magnetic field, where the opening angle is kept as its original value for a long distance. RICH is installed just after the target and silicon vertex trackers in order to minimize the external conversion. The short distance of RICH from the target also makes its dimensions small with a large solid angle coverage.

In the toroidal spectrometer, there are four layers of silicon vertex trackers (SVTs) of the end-cap type (forward SVT) and the barrel type (barrel SVT), respectively, around the target, which are followed by a RICH in front of the toroidal coils. After the toroidal coils, there is a Time-of-Flight counter (TOF) of MRPC (Multi-gap Resistive Plate Chamber), an electro-magnetic calorimeter (EMCAL) made of PbWO₄, and a muon tracker system (MUT) consisting of steel absorbers and GEM trackers. Also there are many GEM trackers between each detector. The detector systems are separated

into a forward section and a barrel section for SVTs, GEM trackers, TOF, EMCAL, and MUT.

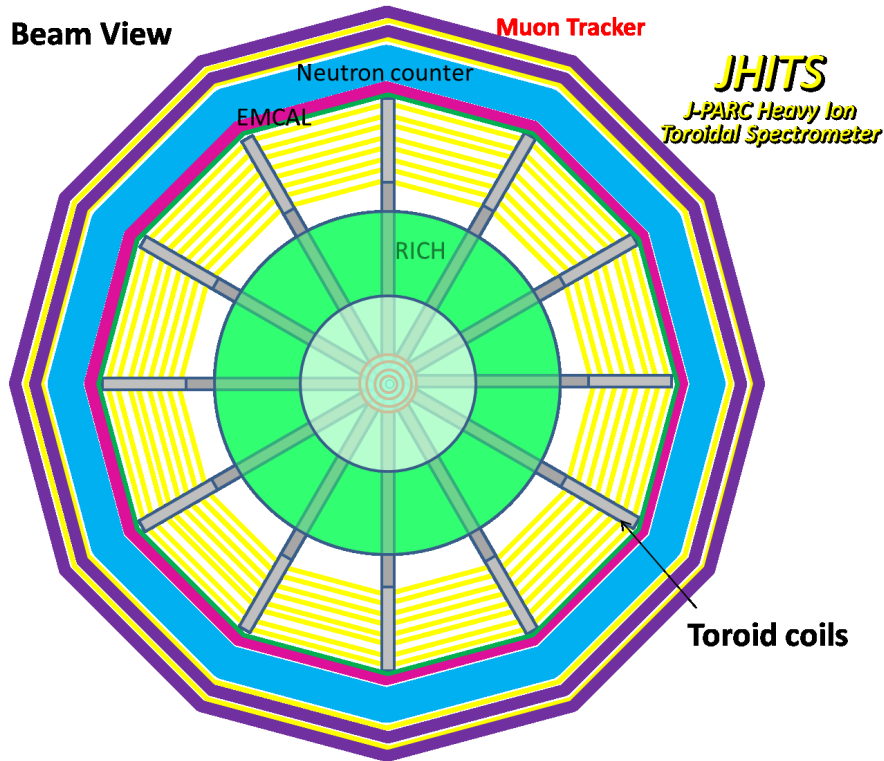


Figure 31: The beam view of the toroidal spectrometer (JHITS; J-PARC Heavy-Ion Toroidal Spectrometer).

The design of the toroidal magnet is based on the CLAS12 toroidal magnet with thin superconducting coils [119]. We choose a “L”-like coil shape, and combine 12 of them as shown in Figs. 31 and 32. In this configuration, the fraction of inactive regions is minimum (less than 10%) and there is a magnetic-field free volume which can accommodate the half-spherical RICH inside. The calculated magnetic-field (mostly in the B_ϕ component) distribution in the $x - y$ cross section is shown in Fig. 33. The B_ϕ has ϕ dependence, which is maximum at the coil center positions, and minimum at the middle of the adjacent coils. Around the middle z -position of the coils, the B_ϕ varies $\pm 20\%$ as shown in the bottom right plot of Fig. 33.

A possible disadvantage of the toroidal configuration is asymmetric acceptance for positive and negative particles, since particles are deflected in the polar angle direction. However, the effect is estimated to be small according to GEANT4 detector simulations. Also, the B_ϕ field is not uniform in the ϕ -direction, which requires precise B-field calculations and measurements.

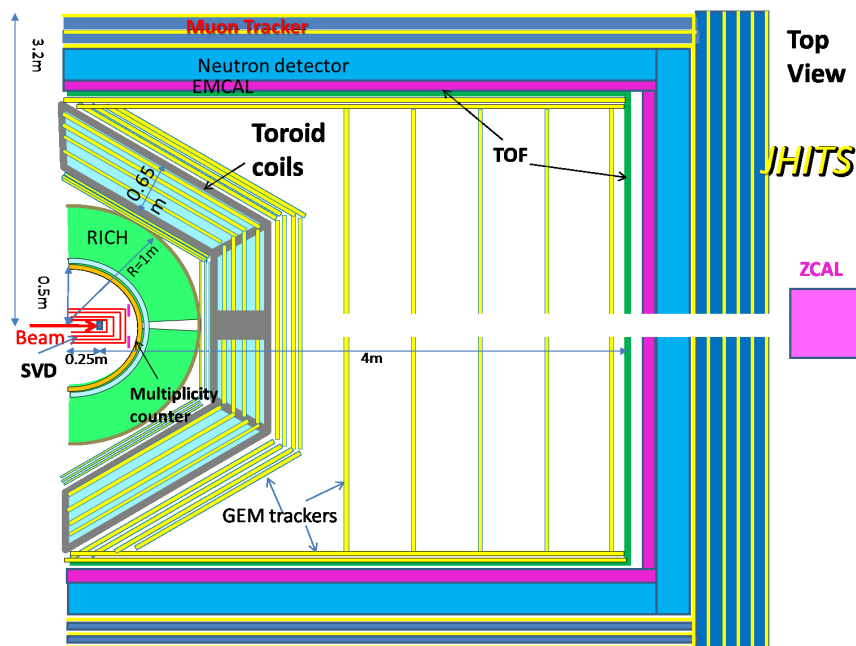


Figure 32: The top view of the toroidal spectrometer (JHITS; J-PARC Heavy-Ion Toroidal Spectrometer).

6.4 Silicon vertex trackers (SVT)

It is extremely important to measure a primary vertex position and secondary vertex positions precisely with the position resolution of several tens μm level, in order to reconstruct weak decay vertex of strange and charmed hadrons. Also, with high particle multiplicity of nucleus collisions, very high granularity of the detectors are required at the positions close to the target. The choice for the silicon vertex tracker (SVT) is naturally silicon pixel and strip detectors. It is very important for dielectron measurements to minimize the material budget of the detectors before RICH in order to suppress external photon conversion. Therefore the material budget of the silicon detectors must be minimized.

There are two examples of silicon vertex detectors for high-energy heavy-ion experiments in PHENIX and ALICE. The pixel size of the PHENIX vertex detector is $50 \mu\text{m} \times 425 \mu\text{m}$ and the material budget is 1.4% radiation length [120]. A sensor of 256×128 pixels with the area of $12.8 \text{ mm} \times 56.7 \text{ mm}$. More advanced silicon pixel detectors with finer pixels are under development for the ALICE upgrade project with $50 \mu\text{m}$ thick CMOS pixel sensors with a pixel pitch of about $30 \times 30 \mu\text{m}^2$ [121]. It is suitable for fine pixels required for J-PARC-HI.

6.5 GEM trackers

We require high-rate capable trackers instead of conventional wire chambers to cope with extremely high particle rates. For this purpose, we adopt a GEM (Micro-Pattern Gas Detector) tracker. We will design a GEM tracker based on the GEM tracker for

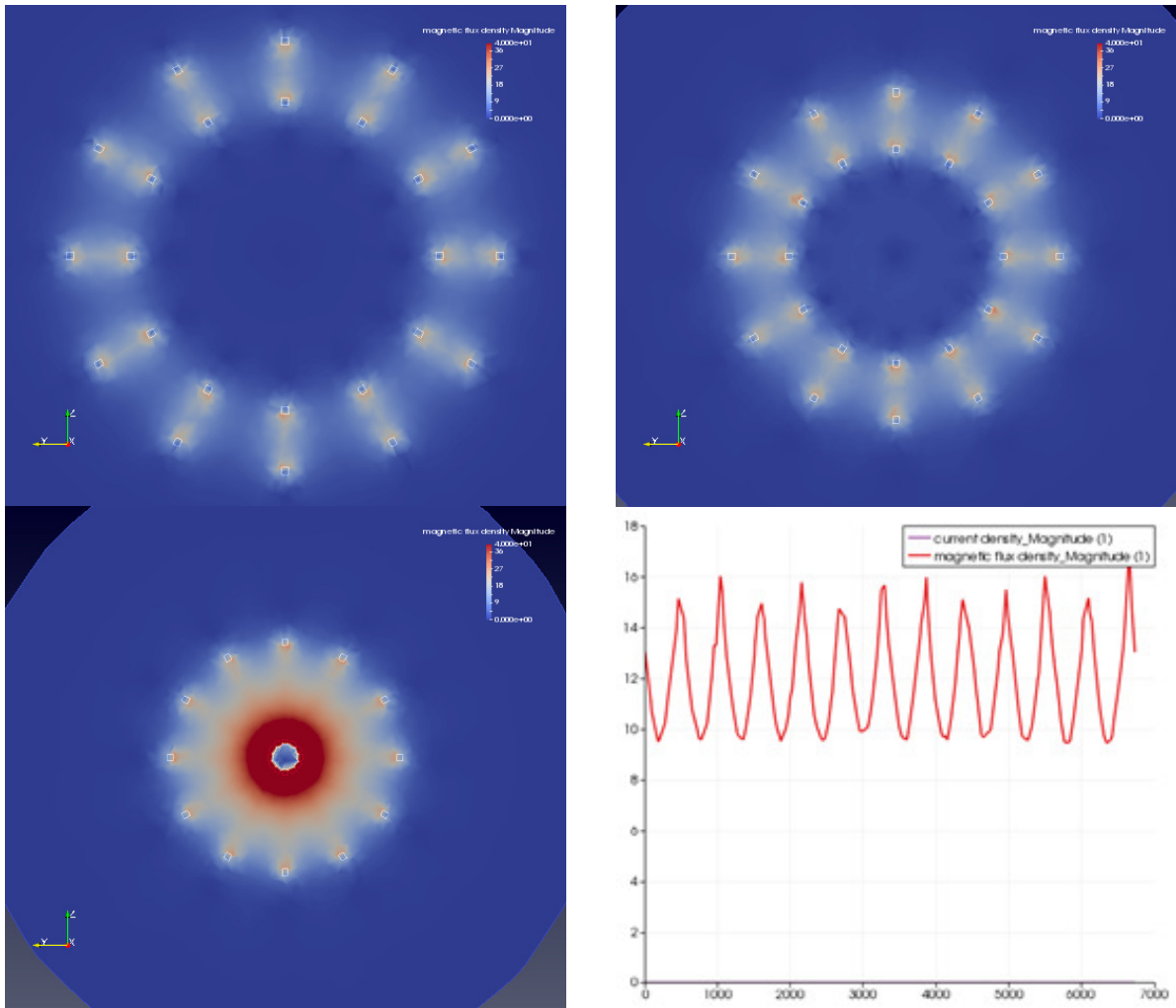


Figure 33: B-field magnitudes in the $x - y$ cross sections at the z -positions of 250 mm (top left), 750 mm (top right), and 1300 mm (bottom left) downstream from the front edge of the coils. The B_ϕ (T) as a function of ϕ (mrad) at the z -position 750 mm downstream from the front edge of the coil (bottom right).

J-PARC E16 experiment [87]. The structure of the E16 GEM tracker with three-layer GEM stack is shown in Fig. 34.

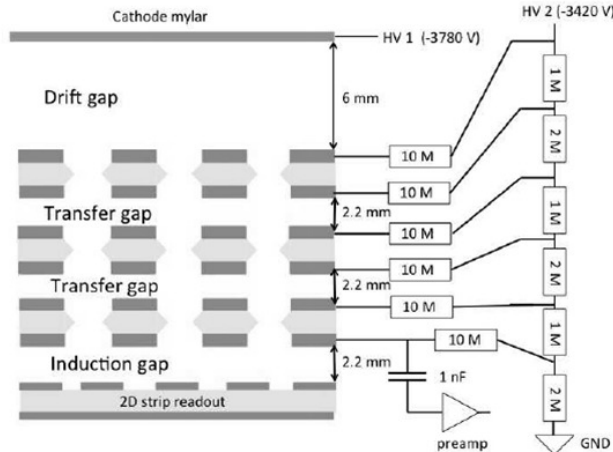


Figure 34: The structure of the E16 GEM tracker [122].

6.6 Ring-imaging Cherenkov counter (RICH)

RICH (Ring-Imaging Cherenkov counter) is the primary device for electron identification, and also muon identification at a low momentum, which is not covered by the muon tracker system. We designed a RICH, based on the concept of double radiators adopted in the HERMES RICH [123]. We adopted C_5F_{12} at 1 atm with the refractive index of 1.0020 as gas radiator with the thickness of 0.5 m, and silica aerogel radiator of 35 mm thickness with the refractive index of 1.030.

We designed a RICH with a spherical mirror with the radius of 1000 mm, arranged as shown in Fig. 35. The photon detector is on a half spherical surface with the radius of 500 mm. We assume a low material photon detector such as a GEM detector with a CsI photo-cathode. The radiator gas vessel is thus in a spherical shape with the radius of 500 – 1000 mm. The aerogel radiator is at the most upstream position, and radiator gas is filled in the rest volume. The center of the RICH system is positioned at the 250 mm downstream in z -position with respect to the target position, so that the reflected ring hits in a backward polar angle on the photon detector. This configuration is based on HADES RICH [124]. The θ and ϕ coverage of the RICH is $2^\circ < \theta < 80^\circ$, and $0^\circ < \phi < 360^\circ$, respectively.

The left plot of Fig. 36 shows calculated Cherenkov light cone angles as a function of particle momentum. Electron to pion separation is done with the C_5F_{12} radiator at $p < 3.1$ GeV/ c assuming 20 mrad angle separation. Muon to pion separation is done with the aerogel radiator at $p < 1.5$ GeV/ c assuming 20 mrad angle separation.

The number of photon-electrons is estimated empirically as follows.

$$N_p = N_0 Z^2 L \sin^2 \theta_c, \quad (4)$$

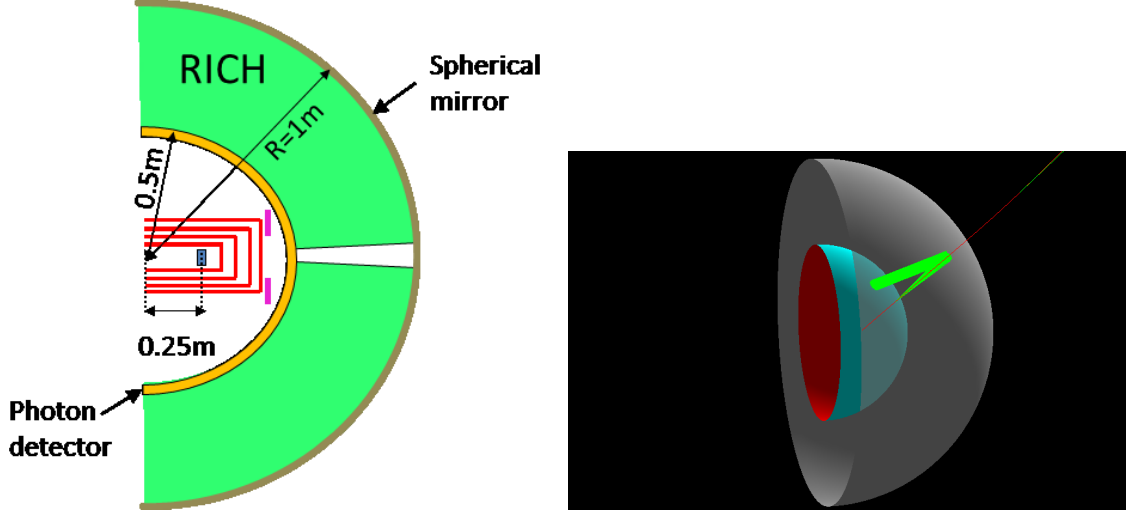


Figure 35: Left : The geometry configuration of the RICH. Right : A simulated event in the RICH with GEANT4. The incident electron at 3 GeV/ c is shown as a red line, and Cherenkov photons are shown as green lines.

where L is the radiator length (cm), Z is the charge number of the incident particle, and the Cherenkov angle θ_c can be calculated as follows.

$$\cos \theta_c = \frac{1}{n\beta}. \quad (5)$$

N_0 is the photon number per unit length (cm), which can be calculated as follows;

$$N_0 = (370\text{eV}^{-1}\text{cm}^{-1})\epsilon\Delta E, \quad (6)$$

where efficiency integral in energy $\epsilon\Delta E$ can be calculated as follows.

$$\epsilon\Delta E = \int (QTF)dE, \quad (7)$$

where Q is the quantum efficiency of the photon detector, T is the transmittance of the radiator, and R is the reflection efficiency of the mirror.

Table 4 summarizes the quantum efficiency of a photo-multiplier as a function of the photon wavelength, which is included in the simulation of the photon detectors. From them, we estimate roughly the $Q\Delta E$ to be 0.5, and T and R to be 1 and 0.9, respectively, which results in $N_0 = 167/\text{cm}$.

The number of photon-electrons as a function of momentum is calculated using the estimated N_0 in the right plot of Fig. 36.

The parameters of RICH are summarized in Table 5. For the aerogel radiator, threshold momenta for electrons, muons, and pions is 0.0021, 0.43, and 0.57 GeV/ c , respectively. The light cone angle is 0.242 rad and the mean number of photon-electrons per ring is 34 at $\beta = 1$. For the C_5F_{12} radiator, threshold momenta for electrons, muons, and pions are 0.0081, 1.7, and 2.2 GeV/ c , respectively. The light cone angle is 0.063 rad and the mean number of photon-electrons per ring is 33 at $\beta = 1$.

Table 4: The quantum efficiency included in the simulation of the photon detector.

λ range (nm)	quantum efficiency
269 – 300	0.15
300 – 350	0.22
350 – 400	0.25
400 – 500	0.23
500 – 600	0.10

Table 5: RICH properties, where n is the refractive index, N_p is the number of photo-electrons per ring at $\beta = 1$, and p_{th} is the threshold momentum for each particle.

Radiator	n	length(mm)	N_p	p_{th}^e (GeV/c)	p_{th}^μ	p_{th}^π
aerogel	1.030	35	34	0.0021	0.43	0.57
C ₅ F ₁₂	1.0020	500	33	0.0081	1.7	2.2

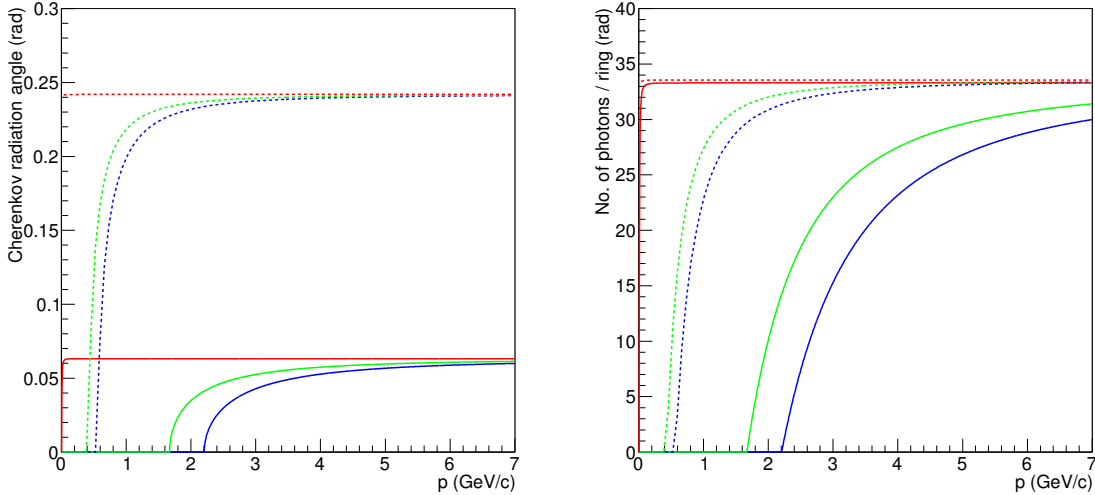


Figure 36: Left : Calculations of Cherenkov angles (rad) as a function of the momentum (GeV/c) for e^\pm (green), μ^\pm (red) and π^\pm (blue) in silica aerogel radiator with the refractive index of 1.030 (dashed lines), and in C₅F₁₂ gas radiator with the refractive index of 1.0020 (solid lines). Right : Calculations of the number of photo-electrons per ring as a function of the momentum (GeV/c) for e^\pm (red), μ^\pm (green) and π^\pm (blue). The solid curves are with the C₅F₁₂ radiator of 500 mm length, and the dashed curves are with the aerogel radiator with the radiator thickness of 35 mm.

6.7 Time-of-flight counters (TOF)

We require a Time-of-Flight counter (TOF) with the timing resolution better than 50 ps for good $\pi - K$ separation. Also, to separate muons from pions at momentum lower than 0.8 GeV/c, we require 30 ps resolution. Recently, a Multi-gap Resistive Plate Chamber (MRPC) has been developed as a TOF with very high resolution of 20 ps level [125]. The structure of the MRPC for the PHENIX TOF is shown in Fig. 37. We are developing a MRPC-TOF based on a small prototype, whose timing resolution of around 40 ps has been already achieved. We are going to test MRPC-TOF's in the J-PARC E16 experiment at the location shown in Fig. 38, and also aim to study hadron production such as $\phi \rightarrow K^+ K^-$.

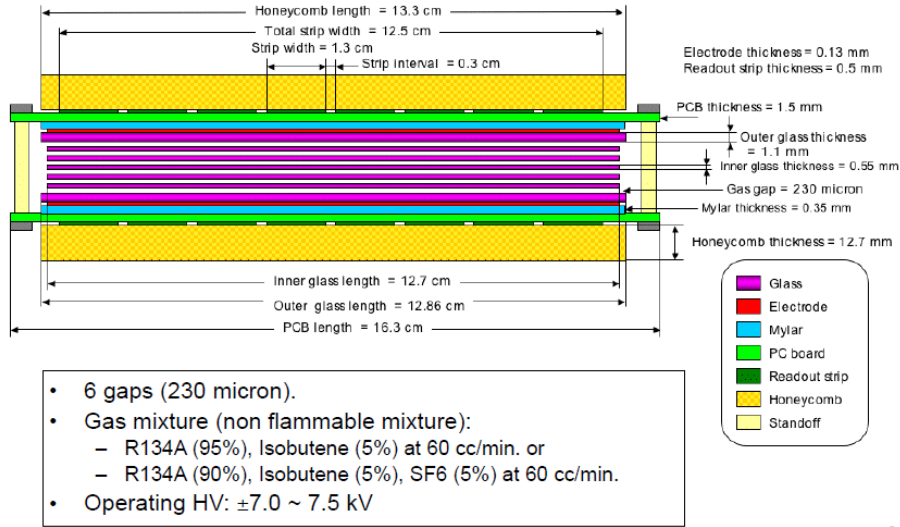


Figure 37: The structure of the MRPC for PHENIX TOF [126].

6.8 Electro-magnetic calorimeter (EMCAL)

The electro-magnetic calorimeter (EMCAL) is the primary device for measuring photons. The photons we observe will mainly come from decay of π^0 's and η 's, in addition to the direct photons from hadron-gas and QGP phase. If we assume the incident energy to be 10 GeV/c, the maximum energy of photons in the calorimeter will be no larger than 10 GeV.

The multiplicity of pions (π^0) in minimum bias U+U collisions at $E_{\text{lab}} = 10$ AGeV goes up to ~ 230 over the rapidity from $y = -0.5$ to -3.5 according to JAM simulation, implying that the detector will see ~ 460 photons at maximum. In addition to this, we have to detect π^0 's down to $p_T = 200$ MeV/c. If we apply the energy asymmetry cut $\alpha < 0.8$, where $\alpha = |E_1 - E_2| / (E_1 + E_2)$, the minimum photon energy that has to be detected will be 20 MeV in p_T or ~ 60 MeV in p . Therefore, the calorimeter has to fulfill the following requirements.

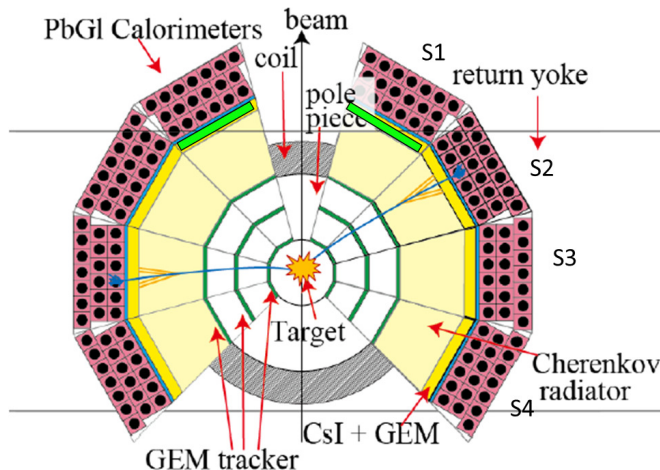


Figure 38: The location of MRPC-TOF's in J-PARC E16 experiment (shown as two green rectangles).

- Accommodate the photons of ~ 500 , meaning that the Moliere radius has to be very small.
- Detect photons with energies as low as 50 MeV, meaning that the calorimeter should have minimum dead layer at the entrance.

Taking these requirements into account, we choose PbWO_4 as a medium of the calorimeter. The PbWO_4 has a very high density ($\rho \simeq 8.3 \text{ g/cm}^3$), a short radiation length ($X_0 = 0.9 \text{ cm}$), and a small Moliere radius ($R_M \simeq 2 \text{ cm}$), and also can be made homogeneous. The thickness of the medium can be determined based on the calculation of longitudinal shower development. The thickness of $25X_0$ will contain most of the shower energies. However, since we employ homogeneous calorimeter, we can measure the energy of photons very precisely by measuring the 90% of their energy, which corresponds to $15X_0$ (14 cm) for 10 GeV photons. The best energy resolution from the statistical term only will be $\sigma_E/E = 2.4/\sqrt{E}$ (%). Since the leakage in the longitudinal direction affects the resolution quite a bit, we propose to install the calorimeter with the thickness of $18X_0$, or 16 cm. This corresponds to $0.8\lambda_{\text{int}}$.

6.9 Neutron and anti-neutron detector

The primary purpose of installing neutron and anti-neutron detectors is to measure baryon number fluctuations in heavy-ion collisions that are considered to be a sensitive probe to the critical point. The momentum of (anti-) neutrons of interest is as low as $300 \text{ MeV}/c$ (mean momentum at the J-PARC energy is expected to be $\sim 100 \text{ MeV}/c$ in p_T). Incorporating measurements of neutrons and anti-neutrons in the same detector needs devising. The neutrons with the energy can only be detected through their hadronic showers in the material of large interaction length with some kind of timing measurement, since they can not deposit energy through Coulomb scattering. The

anti-neutrons will produce some hadronic showers, but the process of annihilation with neutrons in detecting materials contributes significantly. The annihilation process produces two γ 's that can be detected electromagnetically with a photon detection device like a calorimeter.

EMCAL will have $0.8 \lambda_{\text{int}}$. Therefore, we can make use of EMCAL as a detector of (anti-) neutrons, albeit some inefficiency due to the short interaction length. We might need to increase the thickness of EMCAL by a factor of ~ 1.5 in order to let neutrons produce showers. We will place a charged veto detector in front of EMCAL so that the charged particles are tagged and removed from (anti-) neutron samples.

Table 6 shows the response of the detector to be used for (anti-) neutron detection. From this table, by using timing and shower shape information from EMCAL and the

Table 6: Response matrix of particles to the detectors that will be used for (anti-) neutron identification.

Particles	EMCAL shower shape	EMCAL timing	Veto counter
γ	electromagnetic (EM)	very fast	OFF
$\pi^{+/-}$	hadronic + MIP-like eloss	fast	ON
$K^{+/-}$	hadronic + MIP-like eloss	fast	ON
p	hadronic + MIP-like eloss	slow	ON
\bar{p}	hadronic+ MIP-like eloss + EM	slow	ON
n	hadronic	slow	OFF
\bar{n}	hadronic+EM	slow	OFF

signal from the charged veto counter, one can identify (anti-) neutrons. Note that for the fluctuation measurement purpose, the momentum of the (anti-) neutrons does not need to be precise as long as that we can identify the (anti-) neutrons much higher than their mean momentum, which is $1 \text{ GeV}/c$ in the total momentum (p) in our case. It is not very difficult to separate p, \bar{p}, n, \bar{n} from γ samples by timing information at the momentum of $1 \text{ GeV}/c$.

6.10 Muon tracker system (MUT)

The purpose of the muon tracker system (MUT) is to distinguish muons from charged pions by absorbing pions and detecting muons passing through hadron absorbers. We design the system as the combination of iron absorbers and trackers, which is commonly used configuration.

We require the π rejection power, which is defined as the probability that π 's are misidentified as μ 's, to be less than the μ/π yield ratio at the entrance of MUT. The entrance is defined as the upstream surface of EMCAL, which serves as the first absorber with about one interaction length. The μ/π ratio is estimated from the pion weak decay probability to be 0.044 at the EMCAL position of $z = 5 \text{ m}$ for the typical pion momentum of $2 \text{ GeV}/c$. We set the rejection power requirement to be $1/10$ of this value, namely 4.4×10^{-3} .

We studied how much absorber thickness is required to fulfill the rejection power requirement of 4.4×10^{-3} using GEANT4 simulation. We use an iron absorber of 16 cm which corresponds to one interaction length and studied how many absorbers are necessary. The left plot of Fig. 39 shows the survival probability of π^+ as a function of momentum after each absorber. The survival probability is defined as the ratio of the number of tracks after each absorber to the number of tracks after RICH. The rejection requirement is fulfilled with EMCAL and 6 iron absorbers. On the other hand, the survival probability for μ has low momentum cut-off depending on the absorber thickness and is $1.4 - 1.6 \text{ GeV}/c$ with EMCAL and $5 - 6$ iron absorbers as shown in the right plot of Fig. 39. The survival probability is almost flat as a function of momentum above the cut-off and is about 70% independent of the absorber thickness.

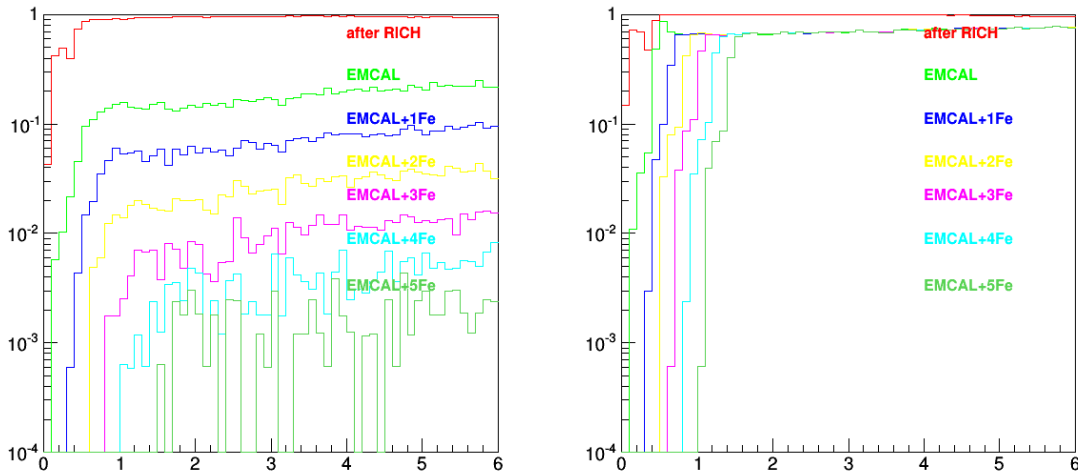


Figure 39: Left : π^+ survival probability as a function of momentum (GeV/c) after absorbers with different thickness. Right : μ^+ survival probability as a function of momentum (GeV/c) after absorbers with different thickness.

Since muons from weak decays are the main background for dimuon analysis, they should be rejected by searching for a kink due to the decay along the trajectory. This can be done by the consistency check with a primary track at as many detector positions as possible. We call it as a track matching cut. Since the decay center-of-mass momentum is $30 \text{ MeV}/c$ for pions and $236 \text{ MeV}/c$ for kaons, pion rejection is much harder than kaon rejection. Here we estimate roughly how much rejection power for weak decays is necessary. The signal to background ratio is defined as;

$$S/B \simeq N_{\mu^+\mu^-}/N_{\pi \rightarrow \mu}, \quad (8)$$

where $N_{\mu^+\mu^-}$ is the number of dimuon signals, and $N_{\pi \rightarrow \mu}$ is the pion weak decay yield. The ratio of the dimuon yield to the π yield is estimated to be 4.6×10^{-5} for the dominant signal of η Dalitz decay, from the product of η/π ratio of 0.15 [127], and the branching ratio of the Dalitz decay of 3.1×10^{-4} . The ratio of the dimuon combinatorial

background to the π yield is estimated as the square of the π weak decay probability before MUT to be 1.9×10^{-3} . Therefore, the signal to background ratio, S/B , is about 0.024. To make S/B to be 1, the weak decay should be suppressed to 15%.

We studied weak decay rejection performance for pions and kaons. In order to find weak decays in flight, track matching was examined in the sections shown in Fig. 40. At the target, we trace back tracks in the silicon trackers to the target z -position and check if the x - and y -positions are close to the target position. For other matching sections, we check consistency of projected x - and y - positions, and local vectors in x - and y - positions. The matching cuts are defined as momentum-dependent $\pm 3\sigma$ cuts using pion tracks except for $\pm 4\sigma$ cuts in the x - local vectors at the matching sections before and after the toroidal coils.

The left plot of Fig. 41 shows the survival probability of μ^+ from π^+ weak decay after the matching cuts as a function of momentum. The weak decay survival probability increases from 0% to 50% at the momentum of 0 – 5.5 GeV/ c . The right plot of Fig. 41 shows the survival probability of μ^+ from K^+ weak decay. The survival probability is 0 – 20% at 0 – 5.5 GeV/ c , which almost fulfills the required 15%. Figure 42 shows μ^+ efficiency after the matching cuts. The efficiency is about 85%.

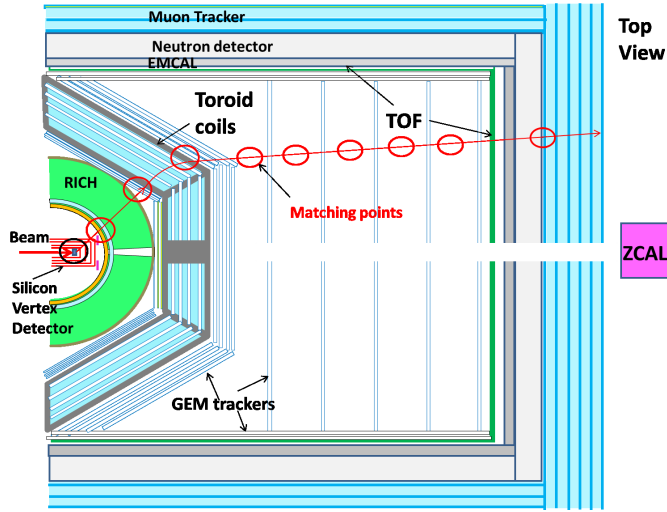


Figure 40: Track matching positions used for weak decay rejection in JHITS (shown as red circles).

6.11 Triggers and centrality counters

Since the event rate is extremely high at J-PARC-HI owing to the very high beam rate, we can select the events of interest motivated by physics. With 10^{11} Hz of the beam rate and 0.1% interaction length of the target, we expect to see the event rate of 10^8 Hz. Obviously, an efficient online/offline trigger for minimum bias events is the most basic and necessary one for measuring heavy-ion collision events. Therefore, we first show the idea of triggering minimum bias events as well as the scheme to determine the centrality of the collisions.

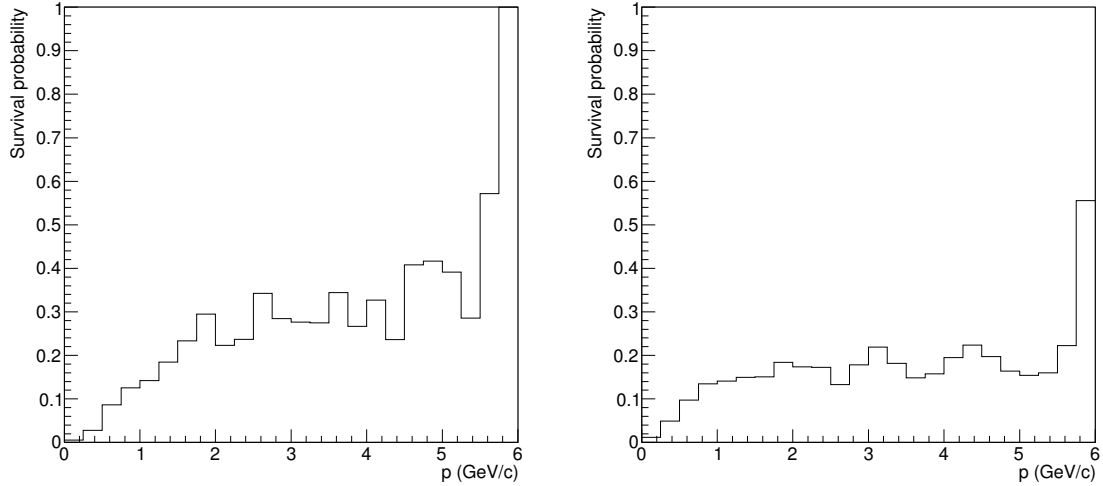


Figure 41: Left : Survival probability of μ^+ from π^+ weak decay as a function of momentum (GeV/c) after the matching cuts. Right : Survival probability of μ^+ from K^+ weak decay as a function of momentum (GeV/c) after the matching cuts.

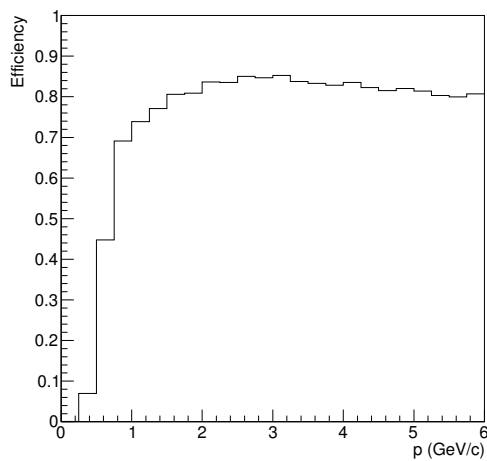


Figure 42: Efficiency of μ^+ as a function of momentum (GeV/c) after the matching cuts.

Physics trigger 1: Minimum bias trigger and centrality selection: Figure 43 shows the trigger setup for minimum bias events. A set of scintillation counters

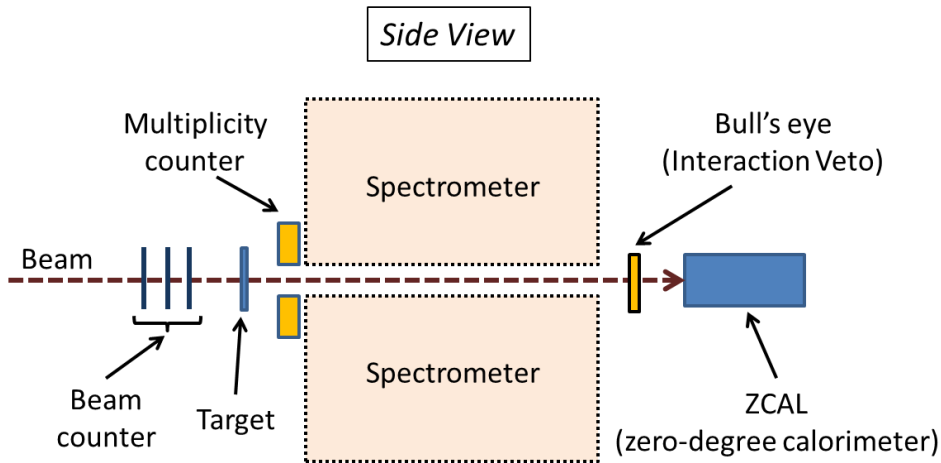


Figure 43: Triggering scheme for the heavy-ion experiment.

placed upstream of the target measure the beams. When a projectile nucleus interacts with a target nucleus, the event is characterized by the deposited energy in the multiplicity counter (MC) and the energy deposit in the zero-degree calorimeter (ZCAL). The interaction is assured by so-called Bull's eye [128] placed far down on the beam axis, followed by the ZCAL. The Bull's eye is a Cherenkov counter that detects the nuclear charge Z of the particles on the beam axis. If an interaction occurs, the Bull's eye should detect less charge compared to the one of the incident ions. The time-zero of an event is provided by the timing information from MC. After a collision, the participant nucleons or the particles produced by the participants will be scattered off the beam axis and deposit energies in MC. The spectator nucleons will fly to the end of the beam line and deposit energy in ZCAL. This scheme has been used in many fixed target experiments in the past. With these detectors, we can roughly measure the centrality and select events by centrality online as explained in the later paragraph. The fine centrality selection can be made offline by using the deposited energy in MC and ZCAL and/or their correlation as shown in Fig. 44. An advantage of the J-PARC fixed target experiment is that the direct measurement of spectator and participant nucleons is possible as opposed to collider experiments such as those in RHIC and the LHC.

Physics trigger 2: Collision geometry trigger: The Uranium is highly deformed in geometry (prolate) compared to the other heavy ions. If one can determine the orientation of an Uranium with respect to the other in a collision, one can control the collision geometry as well as the energy density of the collision system. In U+U collisions at RHIC, several studies were carried out in order to figure out whether or not we can distinguish body-body and tip-tip collisions as depicted in Fig. 45. A theoretical study suggested that one can distinguish two collision geometry by looking at the v_2 (elliptic flow) as a function of multiplicity for charged particles in each event [129]. As going to the higher multiplicity region, more tip-tip collisions will come in, and a kink

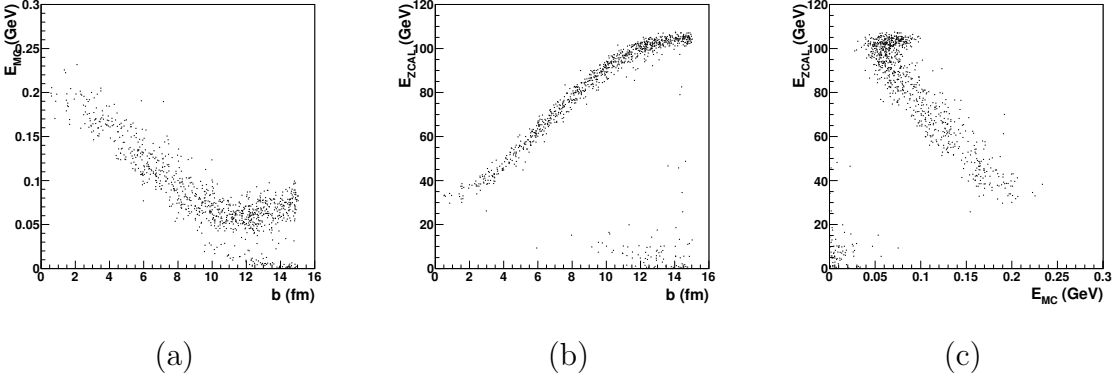


Figure 44: (a) Correlation between the deposited energy in the multiplicity counter ($4^\circ < \theta < 14^\circ$) and the impact parameter, b (fm), (b) correlation between the deposited energy in the ZCAL and b , and (c) correlation of the deposited energy in the ZCAL and the one in the multiplicity counter. Plots are produced with the JAM model [17] in RQMD/S mode that includes fragment production.

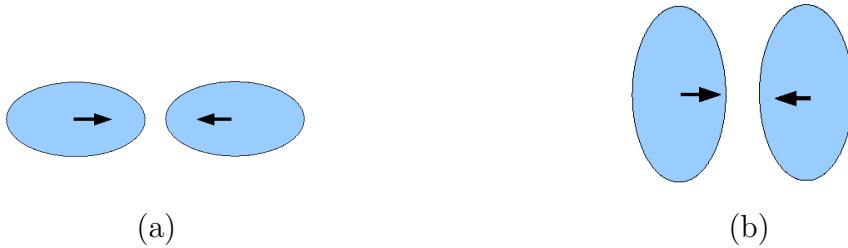


Figure 45: A schematic view of central U+U collisions: (a) tip-tip and (b) body-body.

in v_2 shows up, which is the result of the mixture of full overlap of body-body and tip-tip collisions. The STAR experiment has done also preliminary studies if these v_2 structure difference is seen between Au+Au and U+U collisions [130].

Physics trigger 3: K^- and \bar{p} trigger: One of the other triggers we may consider is a rare particle trigger. At the J-PARC energy, $\pi^{0/+/-}$, K^+ and p are copiously produced in every event, but K^- and \bar{p} are rarely produced. Using the timing information from the time-of-flight counter, one could define an online trigger, while it is challenging at high interaction rates due to event overlap and possible tracking confusions. The time-of-flight counter we are designing has sufficiently good timing resolution to identify K and p online (see Section 6.7).

Physics trigger 4: High p_T photon trigger: One can also consider a high p_T photon trigger. The purpose of the trigger is to measure hard photons even though the production cross-section is very low. Remember that the WA98 experiment has ambiguity of estimating thermal photon component due to lack of the hard photon measurement [131]. This measurement is statistics starved measurement, and suits to the experiment at J-PARC-HI.

Physics trigger 5: Dimuon trigger: We expect that muons from π^\pm decay are copiously produced every events mainly due to weak decays of π and K . However, if we trigger muon pairs with higher momentum ($p > 0.5 \text{ GeV}/c$), the number of events to be triggered will be reduced. The threshold of the momentum will be determined by a full detector simulation.

6.12 Readout electronics and data acquisition system

We estimate the data rates expected from detectors of JHITS. The number of charged particles per event (M_i), where i denotes an index for each detector, is estimated to be 900 ± 110 in a forward tracker at $\theta = 0^\circ - 30^\circ$, and 650 ± 130 in a barrel tracker at $\theta = 30^\circ - 110^\circ$ using JAM event generator and GEANT4 simulation. We also assume the acceptance A to be 80%, and the number of hit pads per particle (S_p) to be 2. If we assume to read 16-bit ADC and 16-bit TDC data including a channel number, the data size per pad hit (D) is 8 B. The interaction rate R_{INT} assuming a 0.1% interaction length target and 10^{10} Hz (10^{11} Hz) beam rate is 10^7 Hz (10^8 Hz). Thus, the data rate (R_D) is derived as;

$$R_D = R_i M_i A S_p D. \quad (9)$$

R_D is calculated to be 1.2 TB/s with the interaction rate of 10^7 Hz , and 12 TB/s at the interaction rate of 10^8 Hz . This raw data rate is in a similar scale as that of the ALICE Run 3 of 3.3 TB/s [132]. ALICE and CBM will reduce the raw data size by a factor of about 37 [132] and 100 before storing them in the final storage, respectively. If we assume the reduction factor of 100, the final data rate will be 12 – 120 GB/s with the interaction rate of $10^7 - 10^8 \text{ Hz}$.

ALICE and CBM adopt free-streaming triggerless DAQ system to take all the data without triggers, and then reduce the data as early as possible online. In J-PARC-HI, a similar scheme will be adopted.

The first stage of Fig. 46 shows the triggerless electronics. A single timing source distributes timing clocks to each detector electronics. The digitized data from each detector electronics is sent to the online computing system shown in the second and later stages of the figure.

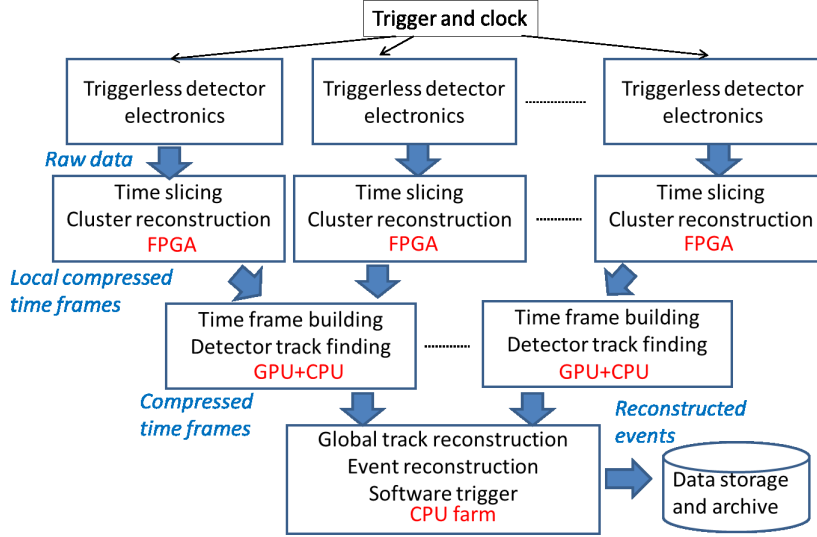


Figure 46: A scheme of triggerless electronics and the online and offline computing system.

The second and later stages of Fig. 46 show the scheme for the online and offline computing system. The design is based on recent performance progress of FPGA (Field-Programmable Gate Arrays) and GPU (Graphics Processing Unit), which replace a CPU and help reduce the total cost. According to ALICE O² (Online-Offline computing system), a GPU replaces 30 CPUs [133]. In the second stage, the raw data from each subsystem of triggerless electronics is split in each constant duration into time frames. Each frame data is tagged with an event number. Then local reconstruction such as cluster reconstruction is done and the data is compressed with a FPGA. In the third stage, a complete set of compressed time frames for a detector are combined (time frame building), and detector track finding is done with GPU and CPU. In the last stage, a complete set of detector data for the whole event are combined (event building), and the global track reconstruction is done in one of the PCs in the CPU farm. Then, in the same PC, event filtering (software trigger) is done according to the characteristics of the event. The filtered event data is stored in the disk and then archived in the tape system.

Assuming the data rate of 12 – 120 GB/s, we require the data storage of about 30 – 300 PB for one month data taking. ALICE will have a similar scale storage system of 60 PB [132].

Table 7: Radiation and fluence per month running time.

	Barrel SVT	Forward SVT	EMCAL
ΔE (MeV)	0.6	0.3	5.09×10^5
M	221.4	531.9	
ρ (g/cm ³)	2.329	2.329	8.300
V (cm ³)	1.15	2.76	1.35×10^6
S (cm ²)	2.45	58.9	9.00×10^4
R_{INT}		10^8	
t		2.6×10^6 s	
R_a (Mrad)	0.9	1.7	0.19
F (cm ⁻²)	2.26×10^{15}	2.26×10^{15}	

6.13 Radiation tolerance

With extremely high beam rates at J-PARC-HI, radiation damages of the detectors could be a serious problem. We estimated possible radiation damages on the detectors using GEANT4 simulation. Assuming interaction rate R_{INT} of 10^8 Hz (0.1% interaction length target and 10^{11} Hz beam rate), The radiation R_a (rad) is calculated as follows;

$$R_a = \frac{1}{C} \frac{\Delta E R_{\text{INT}} t}{W}, \quad (10)$$

where ΔE (MeV) is the total deposit energy to the detector, W (g) is the weight of the detector ($W = V\rho$ where V is the volume and ρ is the density of the detector), t (s) is the irradiated time, and $C = 6.24 \times 10^7$ MeV/g is the unit conversion factor from rad. The fluence F (cm⁻²) is defined as follows;

$$F = \frac{M R_{\text{INT}} t}{S}, \quad (11)$$

where M is the number of particles passing through the detector per event, and S is the area of the detector. The estimated radiations and fluences for an innermost barrel silicon vertex tracker, a most upstream forward silicon vertex tracker, and an electro-magnetic calorimeter as well as their parameters are summarized in Table 7. According to Particle Data Group [134], silicon detectors work normally at the fluence less than 10^{15} for minimum ionizing particles. SVT's of JHITS reach this limit for one month running. The fluence of silicon detectors at CBM for one month was estimated to be 0.5×10^{13} in the unit of the number of neutron equivalent/cm² at SIS-100 [7]. The fluence at CBM is a factor of 40 smaller than that at JHITS, assuming the number of minimum ionizing particle is equivalent to the number of neutrons.

The estimated average radiation at EMCAL of JHITS is comparable to the radiation of 1.0 Mrad for the CBM electro-magnetic calorimeter for one month at the closest location to the beam axis.

6.14 Beamline and experimental facility

The heavy-ion beams slowly extracted from the MR will be transported to the Hadron Experimental Facility through the high-momentum beamline which is originally built for primary proton beams. The experimental area of the E16 experiment (red rectangle) and more downstream space after the planned extension of the Hadron Experimental Facility (yellow rectangle) as shown in Fig. 47 are considered as a candidate location for the heavy-ion spectrometer.

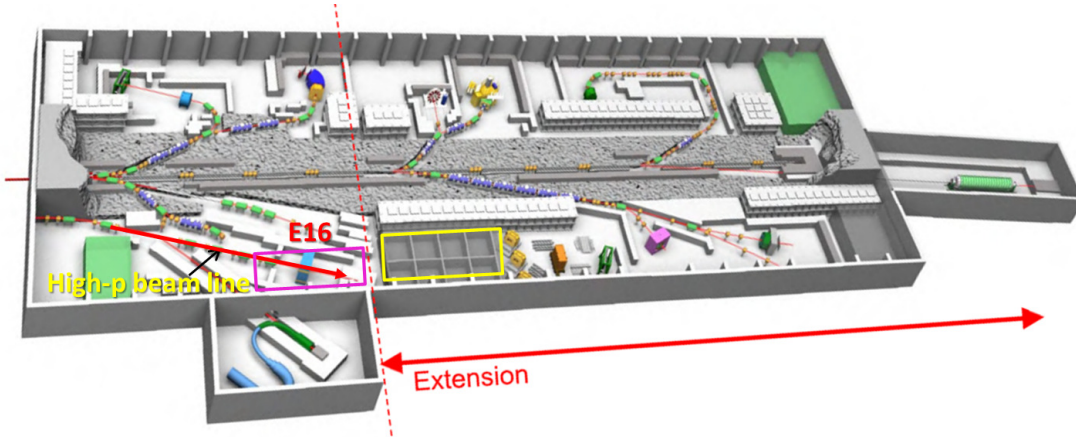


Figure 47: The layout of the J-PARC Hadron Experimental Facility and the high-momentum beamline. The red rectangle of the E16 experimental area, and the yellow rectangle show the candidate space for the J-PARC Heavy-Ion Toroidal Spectrometer.

7 Expected detector performance and physics results

We performed simulation studies in JHITS using GEANT4 and the JAM event generator in U+U collisions at 10 AGeV/ c . For simplicity, we assumed a half-spherical shape for toroidal coils, but we did not include insensitive areas due to the coils (the dead ϕ acceptance should be around 10%), and we assumed a uniform azimuthal magnetic-field. The geometry and material configuration for the trackers is summarized in Tables 8, 9, and 10.

Figure 48 shows acceptance distributions derived by the accepted number of tracks normalized by the generated number of tracks in $y - p_T$ plane for p , π^+ , π^- , and K^+ . Note that for π^+ , π^- , and K^+ , loss due to weak decays is included. Note that vertical grooves at $y = 0.1 - 1.2$ for p , $y = 0.8 - 1.3$ for π^+ , and $y = 1.7 - 2.4$ for π^- correspond to the boundaries between the forward and the barrel spectrometers.

Figure 49 shows the mass-square vs momentum distribution in the forward and the barrel TOF's, where the mass-square is calculated with reconstructed momentum, time-of-flight, and the path length. With the position resolution of SVT's of $14 - 23 \mu\text{m}$, and that of GEM trackers of $0.2 - 0.4 \text{ mm}$, the momentum resolution is evaluated

Table 8: The geometry and resolution of trackers in the barrel spectrometer.

Layer	Detector	$R(\text{mm})$	Pixel size($r\phi \times z$) (mm^2)	Position/timing resolution
1	Silicon pixel	25	0.04×0.12	$0.014 \times 0.12 \text{ mm}^2$
2		50	0.04×0.12	$0.014 \times 0.12 \text{ mm}^2$
3		100	0.08×0.24	$0.023 \times 0.29 \text{ mm}^2$
4		150	0.08×0.24	$0.023 \times 0.29 \text{ mm}^2$
5	GEM tracker	1900	1.9×5.7	$0.2 \times 0.6 \text{ mm}^2$
6		1910	1.9×5.7	$0.2 \times 0.6 \text{ mm}^2$
7	TOF	1920	1.9×5.7	50 ps

Table 9: The geometry and resolution of trackers in the toroidal spectrometer.

Layer	Detector	$R(\text{mm})$	Pixel size($r\phi \times z$) (mm^2)	Position resolution(mm^2)
1	GEM tracker	1050	1.1×1.1	0.1×0.1
2		1100	1.1×1.1	0.1×0.1
3		1150	1.2×1.2	0.1×0.1
4		1250	1.3×1.3	0.1×0.1
5		1450	1.5×1.5	0.2×0.2
6		1650	1.7×1.7	0.2×0.2
7		1850	1.9×1.9	0.2×0.2
8		1870	1.9×1.8	0.2×0.2
9		1880	1.9×1.9	0.2×0.2
10		1890	1.9×1.9	0.2×0.2

Table 10: The geometry and resolution of trackers in the forward spectrometer.

Layer	Detector	$z(\text{mm})$	Pixel size($x \times y$) (mm^2)	Position/timing resolution
1	Silicon pixel	25	0.04×0.04	$0.01 \times 0.01 \text{ mm}^2$
2		50	0.04×0.04	$0.01 \times 0.01 \text{ mm}^2$
3		100	0.08×0.08	$0.02 \times 0.02 \text{ mm}^2$
4		150	0.08×0.08	$0.02 \times 0.02 \text{ mm}^2$
5	Multiplicity counter	200	0.2×0.2	$0.06 \times 0.06 \text{ mm}^2$
6	GEM tracker	2100	2.1×2.1	$0.2 \times 0.2 \text{ mm}^2$
7		2550	2.6×2.6	$0.3 \times 0.3 \text{ mm}^2$
8		3000	3.0×3.0	$0.3 \times 0.3 \text{ mm}^2$
9		3900	3.9×3.9	$0.4 \times 0.4 \text{ mm}^2$
10		TOF	4000	4.0×4.0

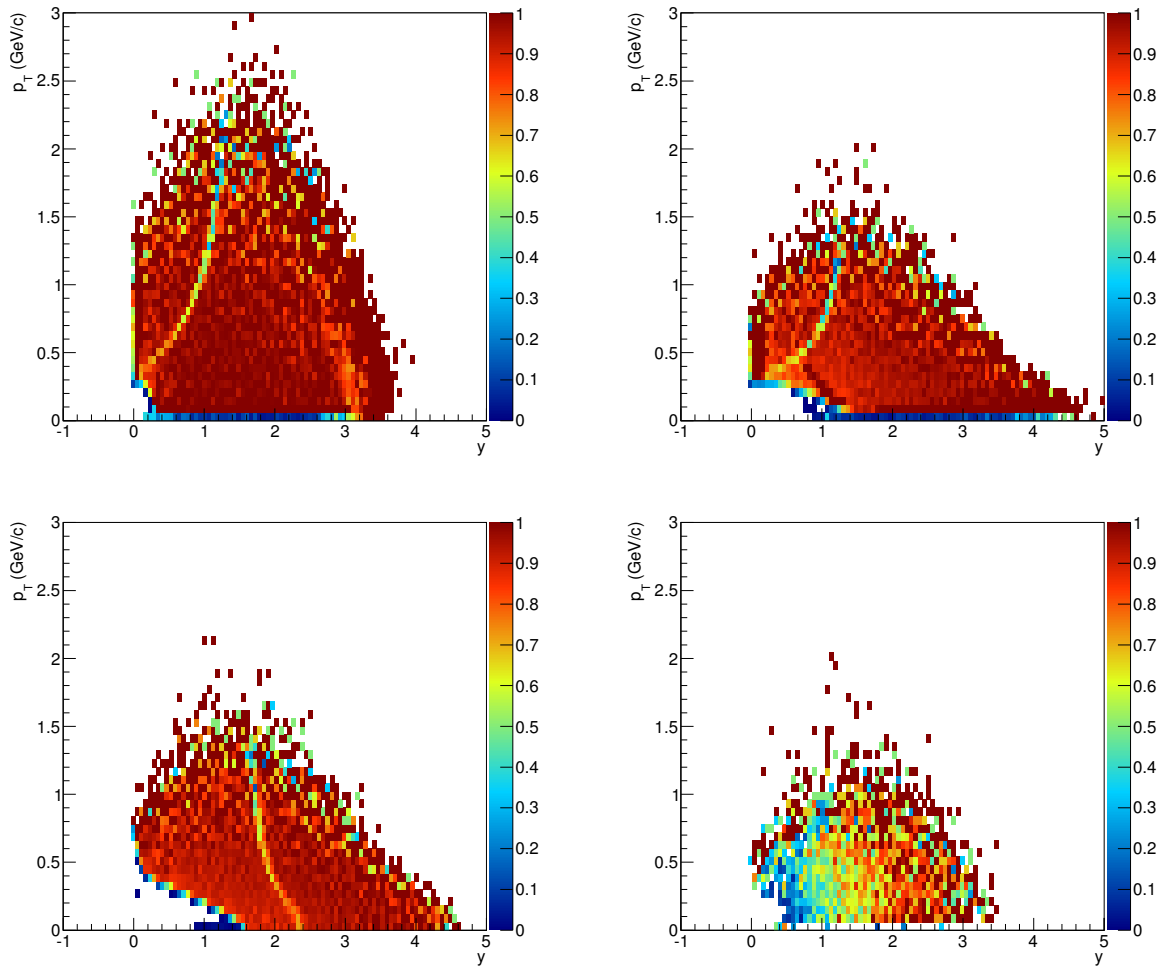


Figure 48: Acceptance distributions in the rapidity (y) - p_T plane for proton (top left), π^+ (top right), π^- (bottom left), and K^+ (bottom right) at 10 AGeV/c (top left) in the toroidal spectrometer.

to be around 1.3% in the barrel spectrometer, and $0.4\% \cdot p$ (GeV/c) in the forward spectrometer. Time resolution of 50 ps (rms) is assumed for TOF's. Clear separation among p , K^\pm and π^\pm is observed. The 2.5σ $\pi - K$ separation is up to 2.5 GeV/c for the forward TOF.

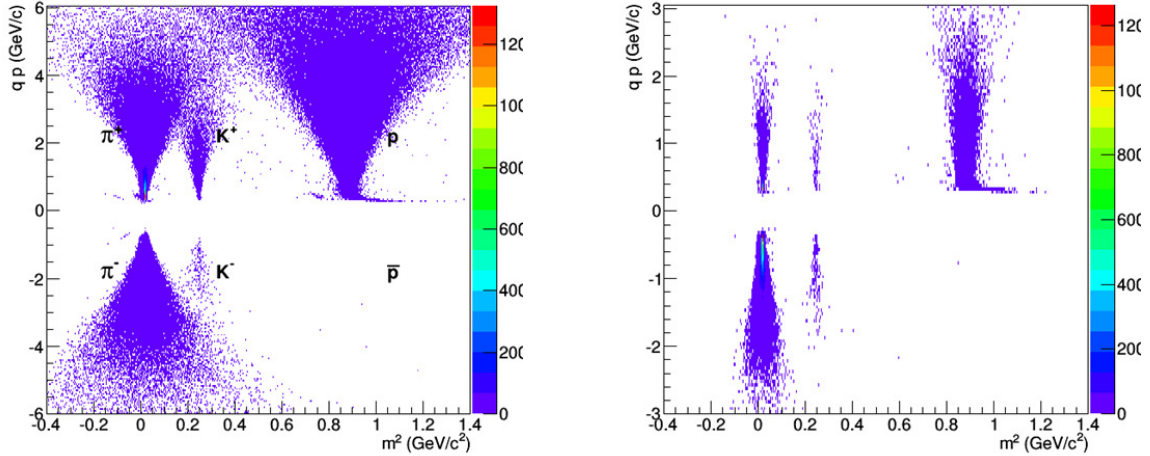


Figure 49: Reconstructed charge times momentum (GeV/c) vs m^2 ($(\text{GeV}/c^2)^2$) at $\theta < 10^\circ$ for the forward TOF (left) and the barrel TOF (right) with JAM events.

We estimated the vertex resolution by closest approach points of primary particles using SVT's as shown in Fig. 50. The estimated transverse resolution is 36 and 110 μm and the longitudinal resolution is 0.87 – 1.4 mm in the barrel and the forward SVT's, respectively. The longitudinal resolution is high enough to reconstruct the decay vertex of strange mesons/baryons, but may not be good enough for charmed mesons/baryons.

Figure 51 shows momentum resolution as a function of momentum for the toroidal spectrometer. High momentum resolution of 0.6 – 2.8% is obtained in the momentum range of 0.5 – 4.0 GeV/c. There is almost no dependence on the polar angle.

We have also performed full track reconstruction and analysis of electrons and muons to reproduce the generated cocktail spectra.

For electrons, we first apply a Hough transformation from pad hits of the photon detector of RICH. The Hough transformation is defined as a transformation of each pad hit into a ring with the radius of the Cherenkov ring radius for a $\beta = 1$ particle. The distribution of Hough transform amplitudes is shown in the left plot of Fig. 52. The local maxima of the distribution correspond to the ring centroids. Then, photoelectron hits belong to each ring are fitted by a circle around a the centroid as shown in the right plot of Fig. 52. Then, rings are associated with reconstructed charged particle tracks at the spherical mirror, where ring positions are projected back on the mirror.

For muons, we reconstruct tracks in MUT which is after EMCAL (1-interaction length) and 5 layer of iron absorbers (5-interaction length). The survival rate of π^\pm after the absorbers is 0.2%, and muon reconstruction efficiency is 80%, with the momentum cut-off of 1.5 GeV/c as shown in Fig. 42.

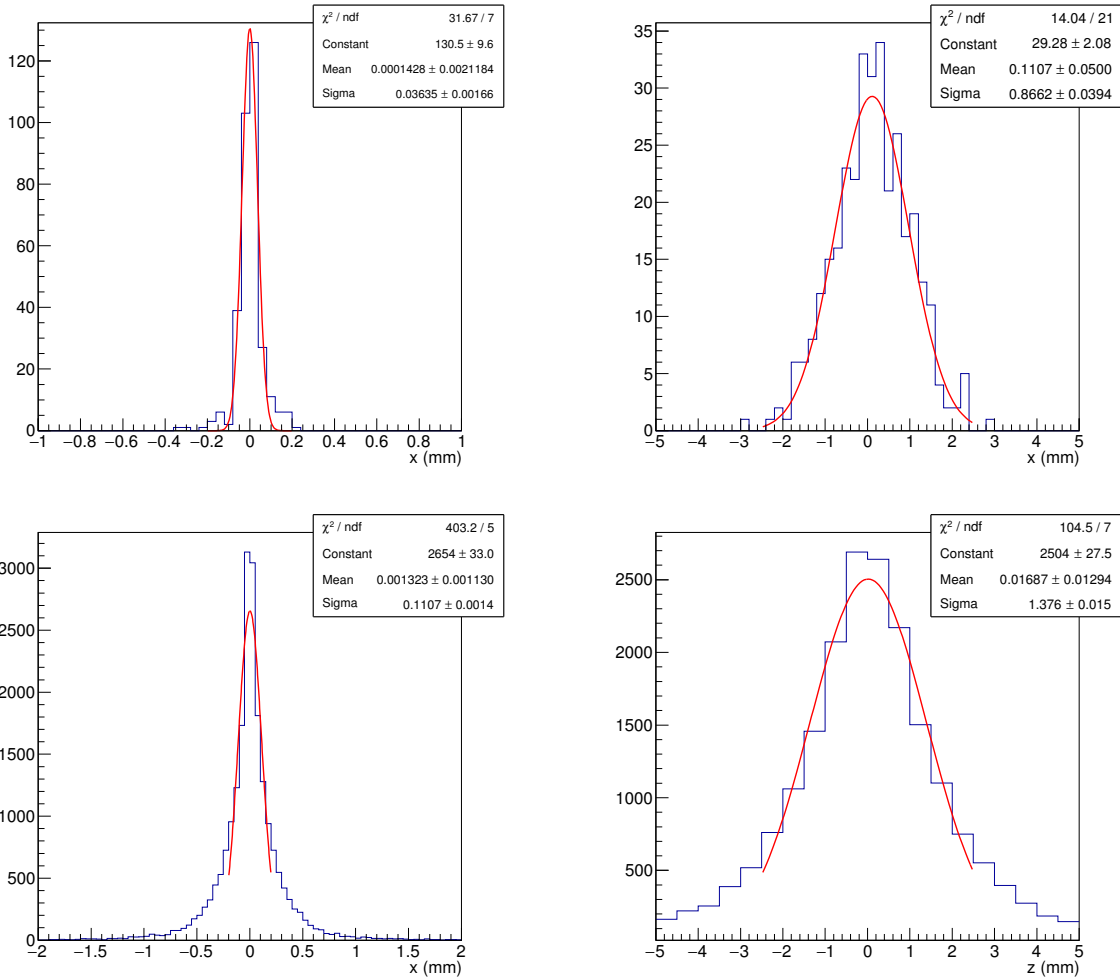


Figure 50: Reconstructed closest approach points using silicon vertex trackers in the x -direction (left) and z -direction (right) for the barrel SVT's (top) and the forward SVT's (bottom). Red lines show the Gaussian fit.

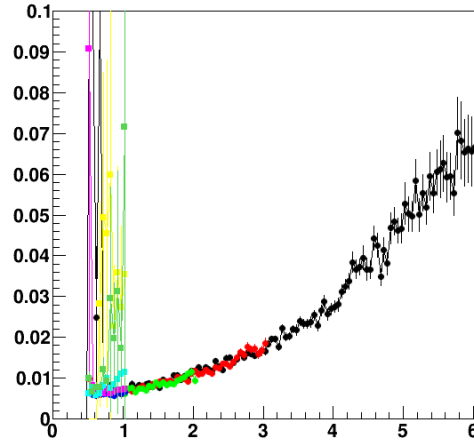


Figure 51: Momentum resolution as a function of momentum (GeV/c) in the toroidal spectrometer. Different colors show different polar angles.

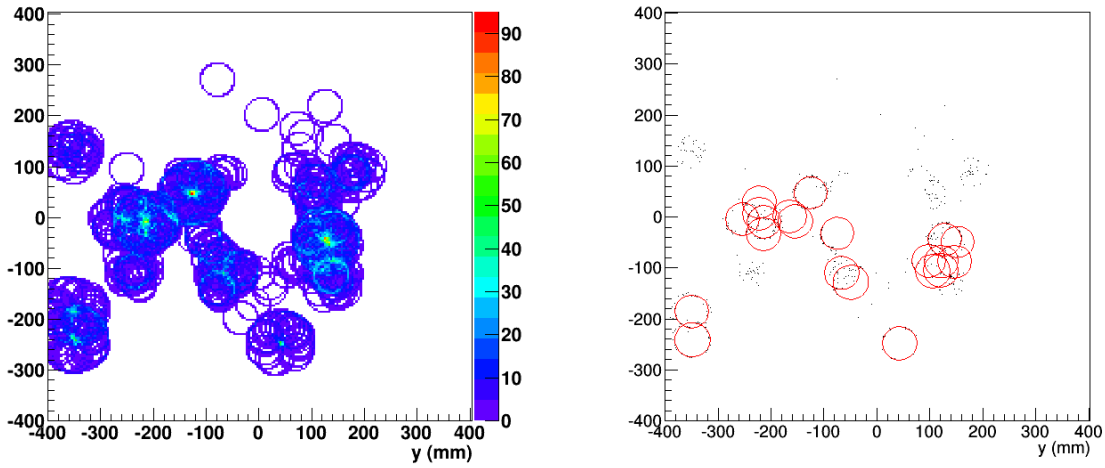


Figure 52: The Hough amplitude distribution (left) and the ring distribution (right) on the photon detector plane for an event.

The top plots of Fig. 53 show the dielectron cocktail spectrum and the reconstructed dielectron spectrum, respectively. The bottom plots of Fig. 53 show the dimuon cocktail spectrum and the reconstructed dimuon spectrum, respectively. The details of cuts are described in the figure caption. The signal spectrum was obtained by subtracting the like-sign mixed pair spectrum from the unlike-sign pair spectrum. Clear ρ and ω peaks are observed in the reconstructed spectra for both dielectrons and dimuons.

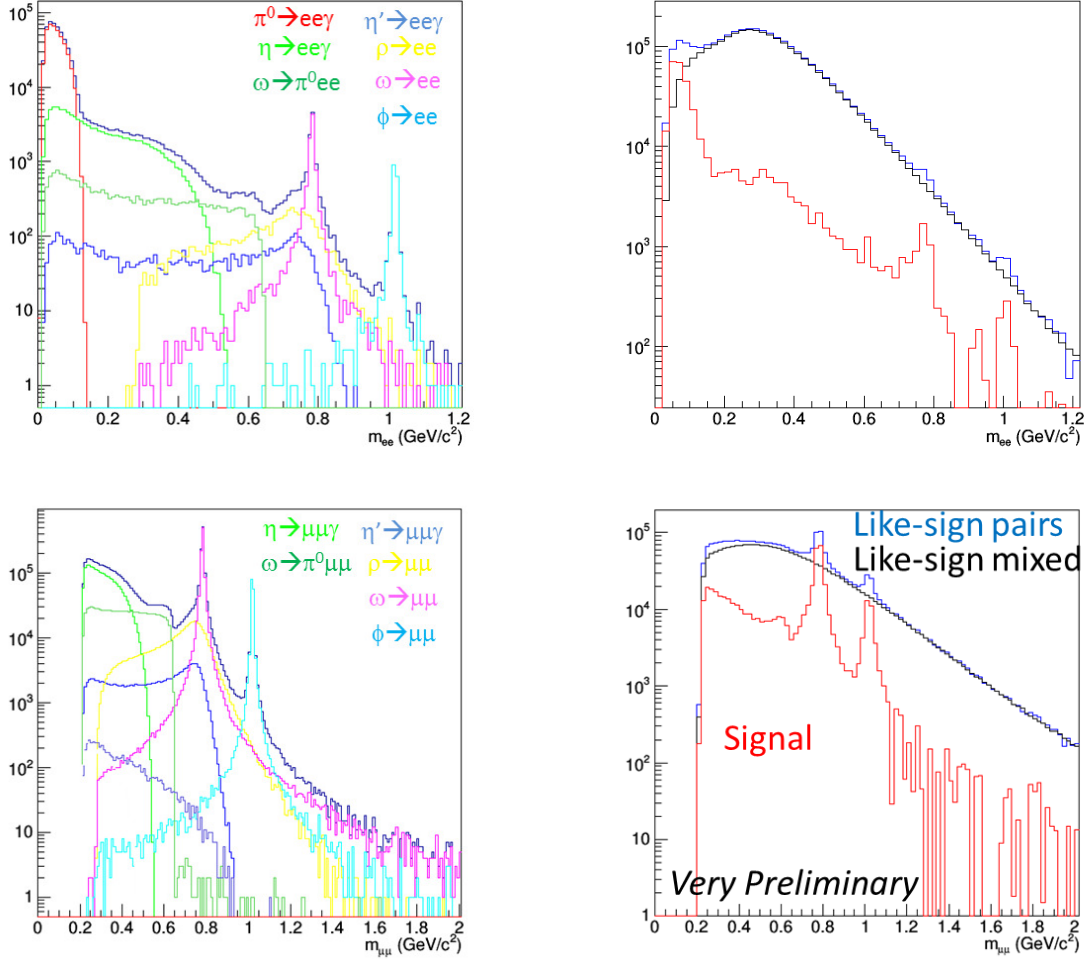


Figure 53: Invariant mass spectra of dielectrons (top) and dimuons (bottom). Left plots are for generated events, and right plots are for reconstructed events. For the dielectron spectra, 8.6 M dielectron cocktail events are used with the cuts for the pair opening angle of more than 5° , $2^\circ < \theta < 80^\circ$ for each electron and positron, and $p_T > 0.1$ GeV/c for each electron and positron. For the dimuon spectra, 500 M dimuon cocktail events are used with the cuts for the pair opening angle of more than 2° , $2^\circ < \theta < 80^\circ$ for each muon, and $p_T > 0.1$ GeV/c for each muon.

8 Project

8.1 International collaboration

As the cases for the other large scale experiments at RHIC and the LHC, the heavy-ion experiments at J-PARC proposed here will not be successful without forming an international collaboration where many institutions from all over the countries contribute for designing, developing, constructing, and operating the detector systems. The current collaboration has just set a ground for soliciting many more new collaborators.

We formed the J-PARC-HI collaboration in this stage with experimental physicists, theoretical physicists, and accelerator scientists including international collaborators, since this program requires the accelerator design, the experimental design, and physics discussions for best experimental observables to find QCD phase structures and properties of dense matter.

Since we have defined physics scopes and a conceptual design of accelerators and an experiment, we are going to define responsibility of each collaborator and each institution soon. We will also organize the collaboration more formally to strengthen the project developments, for example by composing a bylaw of the collaboration and by conducting an election of executive council members of the collaboration.

We have proposed several key detector and accelerator components needed to achieve essential physics goals, while the design is still a reference. We plan to hold several workshops for designing each components in detail, where we will also discuss about sharing responsibility of R&D and designing among institutions. We will also consider to collaborate with existing experiments and detector R&D works within J-PARC and in other experimental projects all over the world, in particular, planned physics programs such as NICA, CBM, and ALICE since there are similar detector requirements among them.

8.2 Staging strategy and other spectrometer options

In case of limited budget and construction time, we may have to consider a staging strategy. We can build minimum components of the accelerators with 98 million dollars. Within this budget, at the initial stage when the beam rate is low, we will not build part of beam monitors and part of magnet power supplies for fine beam tuning. Then as the beam rate increases, we will add the remaining components step by step.

The following priority order should be taken for detectors.

1. The toroidal magnet, forward SVT and GEM trackers, and DAQ (a half scale)
2. Multiplicity counter and ZCAL
3. Forward MRPC-TOF
4. RICH
5. Forward MUT
6. Forward EMCAL

7. Barrel detectors and DAQ (the remaining half scale)

We can study identified charged hadrons at the second staging. As the staging proceeds, we can study electrons using RICH, muons with MUT, and photons with EMCAL. Splitting the construction of forward and barrel detectors is another staging strategy. The higher priority should be given to the forward spectrometer which covers the mid-rapidity at higher beam energies.

Besides staging of the main large spectrometer JHITS, we design also two alternative spectrometers which are more compact with lower cost but with limited physics scopes.

A Hypernuclear spectrometer (Appendix A) aims to measure hypernuclei in the beam rapidity region, by sweeping out other charged hadrons with a strong dipole magnet and stopping them at a collimator. The weak decay of hypernuclei is reconstructed with a TPC in the second dipole magnet. Precise measurement of hypernuclear lifetime as well as the first measurement of the magnetic moment of a hypernucleus may be possible with current detector and data-acquisition techniques.

A dedicated muon spectrometer (Appendix B) consists of only silicon pixel trackers and a muon tracker system with a dipole magnet in order to measure charged particles and muons. The dipole magnet for the J-PARC E16 experiment may be utilized to save the cost.

Actually, these two compact spectrometers could be combined into one spectrometer, and they can be installed in the downstream of JHITS. Therefore, one scenario is to build one of these compact spectrometers first, and then build JHITS.

We also consider to upgrade the dielectron spectrometer of J-PARC-E16 for heavy-ion collisions as an alternative low-cost solution, by adding silicon vertex trackers around the target, and upgrading GEM trackers and the DAQ system for high multiplicity capability. A fast time-of-flight counter for hadron identification, and a muon tracker system for muon identification will enhance its physics capability.

8.3 Cost estimation

The main cost for the proposed heavy-ion acceleration scheme in J-PARC is due to the construction of the heavy-ion linac and the heavy-ion booster ring. Although the final cost would depend on the detailed designing of the accelerators, the total cost at the present stage including the linac, the booster ring, and the addition of the heavy-ion injection system to the RCS is estimated to be about 120 million dollars. The cost of each part is summarized in Table 11. The minimum cost excluding some part of magnets and magnet power supplies, and beam monitors at the initial stage would be 98 million dollars.

The cost for JHITS is not yet clear since detailed design has been not finished. However, by scaling the costs of similar detectors in other large heavy-ion experiments with detector sensitive areas and numbers of channels, a very rough cost is estimated to be 65 million dollars as shown in Table 12. The minimum cost at the initial stage would be 25 million dollars that includes the costs for the toroidal magnet, the forward tracker system (SVT's and GEM trackers), ZCAL, and a half of the DAQ system.

Table 11: The rough cost estimation of the accelerator upgrade for heavy-ion beams.

Item	Cost (1 M dollars)
Building	20
Linac	20
Magnets	30
RF system	10
Vacuum system and beam monitors	10
Power supplies	20
Utilities	10
Total	120

Table 12: The rough cost estimation of detectors in JHITS.

Item	Cost (1 M dollars)
Toroidal magnet	16.5
SVT	2
GEM trackers	11
DAQ	12
ZCAL	0.5
TOF	4.5
RICH	4.5
MUT	2
EMCAL	12
Total	65

The cost of the two alternative spectrometer options and one option involving an upgrade of J-PARC E16 should be much inexpensive than JHITS (an order of a few to several million dollars).

8.4 Schedule and R&D plan

We discuss here the earliest possible schedule for J-PARC-HI. We already released the white paper of J-PARC-HI [135] in June 2016. After submitting this LOI to J-PARC PAC in the end of June 2016, we will start discussion on J-PARC-HI within J-PARC, Japanese Nuclear Physics Community, and Scientific Council of Japan, in close consultation with the international institutions and executive council members of the collaboration. If the project is listed in the master plan of Science Council of Japan in 2019, we will be able to request the construction funding from MEXT (Minister of Education, Culture, Sports, Science and Technology, Japan) in 2020, which can be approved in 2021 at earliest. Following the scenario, we should be able to construct the heavy-ion injector and modify RCS for the heavy-ion injection system in 2021-2023,

and start commissioning beam in 2023-2024. We will also construct the spectrometer by 2024.

Thus, the earliest possible year of the first collision in the experiment is 2025. Note that this schedule highly depends on when the funding is approved.

We need significant R&D efforts for accelerators and detectors to achieve the designed performance of heavy-ion beams and the experiment. For accelerators, we need to develop a high intensity ion source, a linac, and a booster ring with the charge-exchange injection scheme. In order to operate detectors with extremely high rate heavy-ion beams at J-PARC, we need to develop a triggerless data acquisition system, a fine pixel silicon tracker, a Ring Imaging Cherenkov Counter, GEM trackers with fine pads, an electromagnetic calorimeter, and a muon tracker system.

For detector R&D, we will collaborate with experiments which share the J-PARC high-momentum beam line, namely, E16 [87] and E50 [136] experiments. For example, E16 developed GEM trackers, and E50 is planning to develop a triggerless DAQ, double-radiator RICH, a muon tracker system, and an MRPC-TOF.

Since the ALICE upgrade for Run 3 and the CBM experiment at FAIR aim at similar data rates to JHITS of 1 TB/s, there will be great advantage to share R&D efforts with them. Some of JAEA and KEK collaborators are going to join ALICE experiment as an associate collaboration member in July 2016 to contribute to ALICE O² (Online-Offline Computing) Project [132], aiming at future applications to E50 and J-PARC-HI. Significant data rate reduction will be done in O² with online cluster and track reconstruction, which is one of the most important part of the ALICE DAQ system.

Also, R&D of a MRPC-TOF aiming at 40 ps timing resolution has been started by collaborators of JAEA, University of Tsukuba and KEK, and that of a triggerless fast DAQ system has been started by collaborators of JAEA and Nagasaki IAS.

9 Summary

The physics of dense matter beyond the normal nuclear density has recently began to attract increasing interest as a means of exploring the phase structures of the QCD phase diagram. In addition, studies of dense matter can provide insights into how heavy neutron stars with two solar mass can exist, which is one of the most crucial problems in hadron and nuclear physics.

Heavy-ion collisions at nucleon-nucleon center-of-mass energies of a few to several tens of GeV produce the highest density matter with 5 – 10 times the normal nuclear density; this region represents the ideal experimental condition for the study of the relevant physics.

We propose a heavy-ion program at J-PARC wherein we will explore the QCD phase structures and study modifications of hadrons and nuclei in dense matter with a baryon density 5 – 10 times the normal nuclear density.

Heavy-ion beams up to uranium will be accelerated to 20 AGeV possibly at the world's highest beam rate of 10¹¹ Hz. The accelerator design has been developed to incorporate a new heavy-ion linac and booster synchrotron into the existing RCS and

MR synchrotrons. Slowly extracted ion beams from the MR would be transported via a high-momentum beamline to the Hadron Experimental Facility at which the heavy-ion experiments will be performed.

Dileptons will be measured to study medium modifications of vector mesons in the low-mass region to aid in the search for the signature of chiral restoration and for QGP thermal radiation in the intermediate mass region. We will measure event-by-event fluctuations to search for the critical point. In addition, important hadron/nuclear physics at high density will be studied, particularly those related to neutron star cores. The EoS will be studied using collective flow and hadron-hadron interactions based on two-particle momentum correlations, and we will search for $|S| \geq 3$ hypernuclei and strangelets that may exist in the interior of neutron stars. These measurements will be performed at high statistics or, for very rare events, utilizing the high-interaction rates of J-PARC-HI.

We have designed a multi-purpose large acceptance toroidal spectrometer for performing the measurements discussed above. The spectrometer will have large polar angle acceptance and almost full azimuthal coverage. It will comprise silicon vertex trackers, a ring-imaging Cherenkov detector, a time-of-flight counter, an electromagnetic calorimeter, and a muon tracker system. The centrality will be defined by a multiplicity counter and a zero-degree calorimeter. The spectrometer can measure electrons, muons, photons, hadrons, and neutrons, and it has been shown to be able to successfully reconstruct fully simulated dielectron and dimuon spectra.

To achieve the design goals of this program, we will develop accelerator technologies for an ion source, a heavy-ion linac, and a booster ring to produce 10^{11} Hz beams as well as technologies for high-rate capable detectors and a fast data acquisition system that aspires to achieve an experimental data rate of up to 10^8 Hz heavy-ion interactions.

We intend to prepare a budget request plan for construction of the accelerators and the spectrometer by 2018 in order to meet the budget proposal in 2019, for an anticipated first experiment in 2025.

A An alternative experimental plan : Hypernuclear closed geometry spectrometer

We design here a spectrometer for hypernuclear studies at the beam rapidity region, based on the idea shown in Section 2.8. Figure 54 shows the design of the hypernuclear spectrometer to measure hypernuclei at the beam rapidity.

It consists of a first dipole magnet which sweeps out most of produced hadrons and stops at the tungsten collimator. The second dipole contains a TPC which measures hypernuclear weak decays. For instance, a ${}^3_{\Lambda}\text{H}$ decays into ${}^3\text{He}$ and π^- . The π^- is tagged with a trigger counter. The downstream time-of-flight counter identifies π^- . The magnetic moment can be measured by the spin precession of a hypernucleus. A hypernucleus can be polarized by selecting one with some emission angle with respect to the beam. The polarization can be measured by decay event planes of π^- and a nucleus from a hypernucleus. Using the relation of the polarization and the decay position, the magnetic moment of a hypernucleus can be measured.

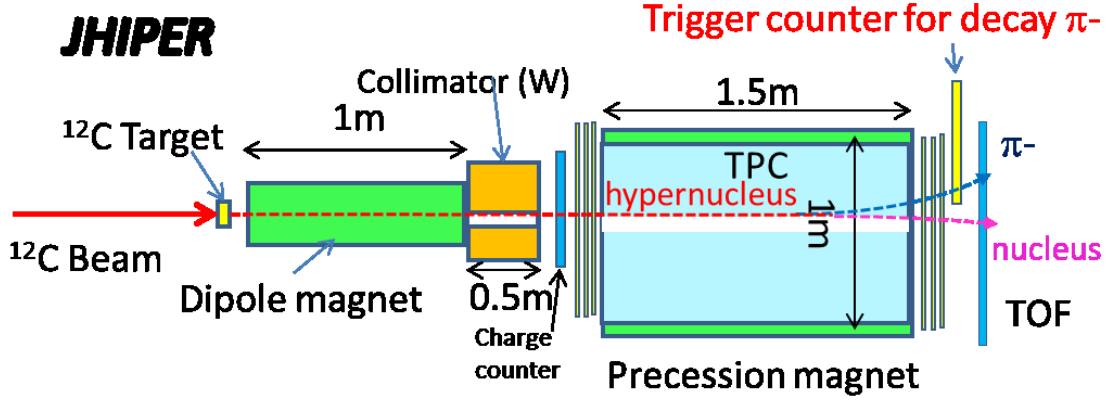


Figure 54: A conceptual design of the hypernuclear spectrometer (JHIPER; J-PARC Heavy-Ion hyperNuclear experiment) at J-PARC.

We simulated fragments and hypernuclei using JAM version 1.622 in RQMD/S mode. We generated minimum bias C+C collision events at $15 \text{ AGeV}/c$. This model can produce fragments and hypernuclear fragments formed in the coalescence mechanism. Hypernuclei with Λ and Σ can be produced. According to the $y-p_T$ distributions of fragments, heavier fragments are produced more around the target and the beam rapidities.

Figure 55 shows Z/A vs x (horizontal position) for fragments. A clear anti-correlation is observed especially after the collimator in the TPC. By selecting the x -position, fragments of a particular Z/A can be selected.

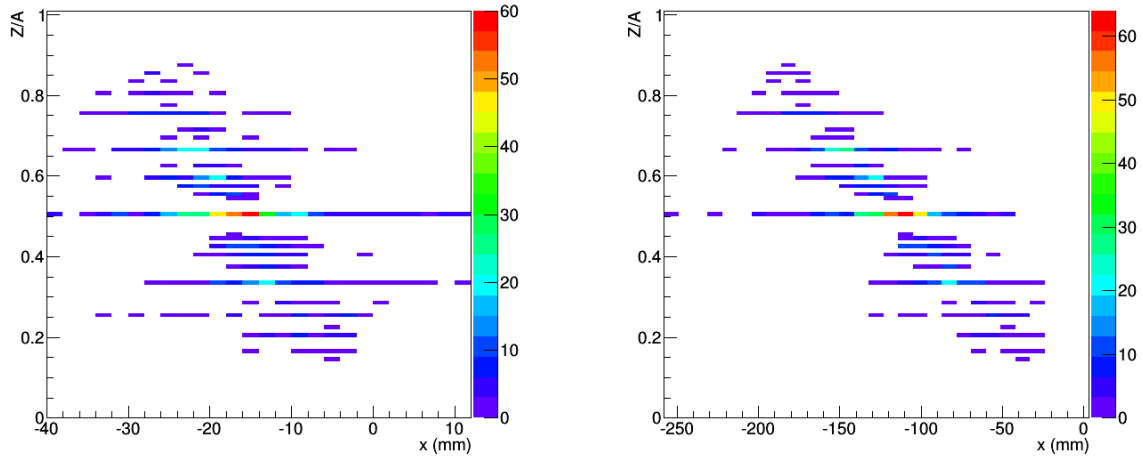


Figure 55: Z/A vs the horizontal (x) position for produced fragments at the z position (along the beam) before the collimator (left), and at the end of the TPC (right).

We simulated $^3\text{H} \rightarrow ^3\text{He} + \pi^-$ decay. The distributions of them are shown in Fig. 56. Since π^- has a large x -position, it can be triggered by a counter with the acceptance of

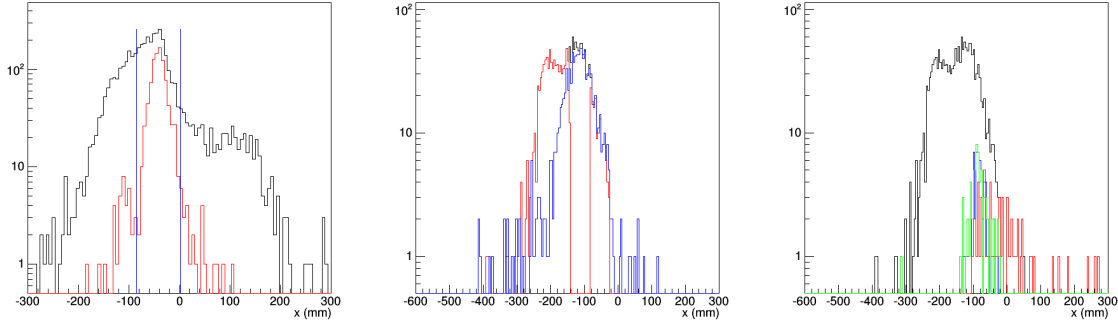


Figure 56: Left : The horizontal (x) position distributions for fragments (red) and all charged particles (black) at the entrance of the collimator. The two vertical lines represent the collimator hole. Middle : The horizontal (x) position distributions for fragments (blue), and fragments and all charged particles (red) measured in the TPC at the entrance of the exit of the TPC. The TPC has an insensitive hole for beams. Right : The horizontal (x) position distributions for all charged particles and fragments (black), compared to the ${}^3_{\Lambda}\text{H}$ (blue), and ${}^3\text{He}$ (green) and π^- (red) from ${}^3_{\Lambda}\text{H}$ decay.

$x = 0 - 300$ (mm). We estimated the trigger rate and particle rates at the TPC. The number of tracks in the TPC is $0.94 / \text{event}$. The weak decay trigger efficiency is 36%. The weak decay probability of ${}^3_{\Lambda}\text{H}$ in the TPC is 11%, assuming the life time of Λ of $c\tau = 7.8$ cm. We estimated from JAM the ratio of the hypernuclei (dominantly ${}^3_{\Lambda}\text{H}$) to be 1%. Then, we derive the trigger rate to be $3 \times 10^{-4} / \text{event}$. Assuming the 10^8 interaction rate, the track rate in the TPC is 10^8 tracks/s which spread over different drift volume in the TPC, and the hypernuclear trigger rate is 3×10^4 Hz. Both rates are feasible with the current TPC and DAQ technology.

B An alternative experimental plan : Dedicated dimuon spectrometer

Although we can measure dimuons in JHITS (See Section 7), we can consider also a dedicated dimuon spectrometer with a much lower cost, which can utilize the full beam rate. We designed the dimuon spectrometer as shown in Fig. 57. The spectrometer consists of silicon vertex trackers around the target, which is inside a dipole magnet, and backward muon trackers which are sandwiched by iron return yokes of the dipole magnet, and forward muon trackers and iron absorbers. The spectrometer can measure charge particles and identify muons in almost full 4π solid angle. We estimated the track rates using GEANT4 simulation with U+U events generated by JAM at $10 \text{ AGeV}/c$. The dimuon trigger is defined as an event with a positive and a negative particles after 7-interaction length iron absorbers.

Assuming the interaction rate of 10^8 Hz, the dimuon trigger rate is estimated to be 3×10^5 mainly from π , K weak decay background at the forward muon trackers of

$\theta < 33^\circ$. On the other hand, the signal dimuon rate is estimated to be around 10^5 Hz. Therefore, the experiment with the full beam rate should be feasible.

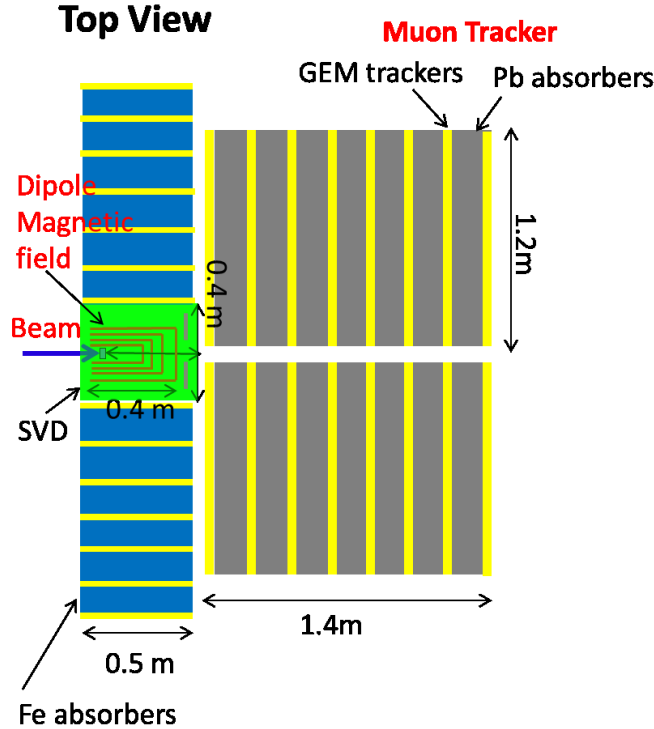


Figure 57: A schematic view of the dimuon spectrometer at J-PARC (top view).

References

- [1] Misha A. Stephanov, K. Rajagopal, and Edward V. Shuryak. Signatures of the tricritical point in QCD. *Phys. Rev. Lett.*, 81:4816–4819, 1998.
- [2] K. Adcox et al. Formation of dense partonic matter in relativistic nucleus-nucleus collisions at RHIC: Experimental evaluation by the PHENIX collaboration. *Nucl. Phys.*, A757:184–283, 2005.
- [3] John Adams et al. Experimental and theoretical challenges in the search for the quark gluon plasma: The STAR Collaboration’s critical assessment of the evidence from RHIC collisions. *Nucl. Phys.*, A757:102–183, 2005.
- [4] H. Hamagaki. The final lecture at University of Tokyo, 2015.
- [5] The STAR Collaboration. Experimental Study of the QCD Phase Diagram & Search for the Critical Point: Selected Arguments for the Run-10 Beam Energy Scan, 2009. STAR Notes SN0493.

- [6] The STAR Collaboration. Studying the Phase Diagram of QCD Matter at RHIC, 2014. STAR Notes SN0598.
- [7] FAIR baseline technical report, 2006. <http://www.fair-center.eu/for-users/publications/fair-publications.html>.
- [8] R. Rapp et al. In-medium excitations. Lect. Notes Phys., 814:335–529, 2011.
- [9] Design and construction of nucleotron-based ion collider facility (NICA) conceptual design report, 2008. http://nica.jinr.ru/files/NICA_CDR.pdf.
- [10] Heng-Tong Ding, Frithjof Karsch, and Swagato Mukherjee. Thermodynamics of strong-interaction matter from Lattice QCD. Int. J. Mod. Phys., E24(10):1530007, 2015.
- [11] Kenji Fukushima and Tetsuo Hatsuda. The phase diagram of dense QCD. Rept. Prog. Phys., 74:014001, 2011.
- [12] Mark G. Alford, Andreas Schmitt, Krishna Rajagopal, and Thomas Schfer. Color superconductivity in dense quark matter. Rev. Mod. Phys., 80:1455–1515, 2008.
- [13] E. Nakano and T. Tatsumi. Chiral symmetry and density wave in quark matter. Phys. Rev., D71:114006, 2005.
- [14] Philippe de Forcrand, Mikhail A. Stephanov, and Urs Wenger. On the phase diagram of QCD at finite isospin density. PoS, LAT2007:237, 2007.
- [15] Lokesh Kumar. STAR Results from the RHIC Beam Energy Scan-I. Nucl. Phys., A904-905:256c–263c, 2013.
- [16] I. G. Bearden et al. Nuclear stopping in Au + Au collisions at $\sqrt{s_{NN}} = 200$ -GeV. Phys. Rev. Lett., 93:102301, 2004.
- [17] Y. Nara, N. Otuka, A. Ohnishi, K. Niita, and S. Chiba. Study of relativistic nuclear collisions at AGS energies from p + Be to Au + Au with hadronic cascade model. Phys. Rev., C61:024901, 2000.
- [18] Y. Nara. private communication.
- [19] J. Randrup and J. Cleymans. Maximum freeze-out baryon density in nuclear collisions. Phys. Rev., C74:047901, 2006.
- [20] Stuart L. Shapiro. Head on collision of neutron stars as a thought experiment. Phys. Rev., D58:103002, 1998.
- [21] B. P. Abbott et al. Observation of Gravitational Waves from a Binary Black Hole Merger. Phys. Rev. Lett., 116(6):061102, 2016.
- [22] O. Korobkin, S. Rosswog, A. Arcones, and C. Winteler. On the astrophysical robustness of neutron star merger r-process. Mon. Not. Roy. Astron. Soc., 426:1940, 2012.

- [23] Pisin Chen and Lance Labun. Electromagnetic signal of the QCD phase transition in neutron star mergers. Phys. Rev., D88:083006, 2013.
- [24] Akira Ohnishi. Physics of heavy-ion collisions at JHF. Proceedings of the 2nd theory workshop on JHF nuclear physics, 2002. KEK-PROC-2002-13 <http://www2.yukawa.kyoto-u.ac.jp/~akira.ohnishi/Src/Misc/KEK-JHF-Ohnishi2002.pdf>.
- [25] Akira Ohnishi. Approaches to QCD phase diagram; effective models, strong-coupling lattice QCD, and compact stars. J. Phys. Conf. Ser., 668(1):012004, 2016.
- [26] Takao Sakaguchi. Photon and dilepton production in high energy heavy ion collisions. Pramana, 84(5):845–859, 2015.
- [27] A. Adare et al. Enhanced production of direct photons in Au+Au collisions at $\sqrt{s_{NN}} = 200$ GeV and implications for the initial temperature. Phys. Rev. Lett., 104:132301, 2010.
- [28] Martin Wilde. Measurement of Direct Photons in pp and Pb-Pb Collisions with ALICE. Nucl. Phys., A904-905:573c–576c, 2013.
- [29] A. Adare et al. Centrality dependence of low-momentum direct-photon production in Au+Au collisions at $\sqrt{s_{NN}} = 200$ GeV. arXiv:1405.3940 [nucl-ex], 2014.
- [30] Ralf Rapp and Jochen Wambach. Low mass dileptons at the CERN SPS: Evidence for chiral restoration? Eur. Phys. J., A6:415–420, 1999.
- [31] Frank Geurts. The STAR Dilepton Physics Program. Nucl. Phys., A904-905:217c–224c, 2013.
- [32] G. Agakichiev et al. $e^+ e^-$ pair production in Pb - Au collisions at 158-GeV per nucleon. Eur. Phys. J., C41:475–513, 2005.
- [33] E.L. Bratkovskaya and W. Cassing. Dilepton production from AGS to SPS energies within a relativistic transport approach. Nucl. Phys. A, 619(3-4):413 – 446, 1997.
- [34] Stephan Endres, Hendrik van Hees, and Marcus Bleicher. Photon and dilepton production at FAIR and RHIC-BES energies using coarse-grained microscopic transport simulations. arXiv:1512.06549, 2015.
- [35] Ryugo S. Hayano and Tetsuo Hatsuda. Hadron properties in the nuclear medium. Rev. Mod. Phys., 82:2949, 2010.
- [36] A. Andronic, D. Blaschke, P. Braun-Munzinger, J. Cleymans, K. Fukushima, et al. Hadron Production in Ultra-relativistic Nuclear Collisions: Quarkyonic Matter and a Triple Point in the Phase Diagram of QCD. Nucl. Phys., A837:65–86, 2010.

- [37] Chiho Nonaka and Masayuki Asakawa. Hydrodynamical evolution near the QCD critical end point. Phys. Rev., C71:044904, 2005.
- [38] E. Nakano, B. J. Schaefer, B. Stokic, B. Friman, and K. Redlich. Fluctuations and isentropes near the chiral critical endpoint. Phys. Lett., B682:401–407, 2010.
- [39] Volker Koch. Hadronic Fluctuations and Correlations. In Chapter of the book Relativistic Heavy Ion Physics, R. Stock (Ed.), Springer, Heidelberg, 2010, p. 626–652. (Landolt-Boernstein New Series I, v. 23). (ISBN: 978-3-642-01538-0, 978-3-642-01539-7 (eBook)), pages 626–652. 2010.
- [40] Masayuki Asakawa and Masakiyo Kitazawa. Fluctuations of conserved charges in relativistic heavy ion collisions: An introduction. arXiv:1512.05038 [nucl-th], 2015.
- [41] Xiaofeng Luo. Exploring the QCD Phase Structure with Beam Energy Scan in Heavy-ion Collisions. In 25th International Conference on Ultra-Relativistic Nucleus-Nucleus Collisions (Quark Matter 2015) Kobe, Japan, September 27-October 3, 2015, 2015.
- [42] M. A. Stephanov. Sign of kurtosis near the qcd critical point. Phys. Rev. Lett., 107:052301, Jul 2011.
- [43] Xiaofeng Luo. Energy Dependence of Moments of Net-Proton and Net-Charge Multiplicity Distributions at STAR. PoS, CPOD2014:019, 2015.
- [44] Atsushi Nakamura and Keitaro Nagata. What are multiplicity distributions telling us about the qcd phase diagram? Nucl. Phys. A, 931:825 – 830, 2014. QUARK MATTER 2014 XXIV International Conference on Ultrarelativistic Nucleus-Nucleus Collisions.
- [45] Xiaofeng Luo. Unified Description of Efficiency Correction and Error Estimation for Moments of Conserved Quantities in Heavy-Ion Collisions. Phys. Rev., C91(3):034907, 2015.
- [46] Masakiyo Kitazawa and Masayuki Asakawa. Relation between baryon number fluctuations and experimentally observed proton number fluctuations in relativistic heavy ion collisions. Phys. Rev., C86:024904, 2012. [Erratum: Phys. Rev.C86,069902(2012)].
- [47] Gerson Goldhaber, William B. Fowler, Sulamith Goldhaber, and T. F. Hoang. Pion-pion correlations in antiproton annihilation events. Phys. Rev. Lett., 3:181–183, 1959.
- [48] C. M. Hung and Edward V. Shuryak. Hydrodynamics near the QCD phase transition: Looking for the longest lived fireball. Phys. Rev. Lett., 75:4003–4006, 1995.

- [49] Dirk H. Rischke and Miklos Gyulassy. The Time delay signature of quark - gluon plasma formation in relativistic nuclear collisions. Nucl. Phys., A608:479–512, 1996.
- [50] Roy A. Lacey. Indications for a Critical End Point in the Phase Diagram for Hot and Dense Nuclear Matter. Phys. Rev. Lett., 114(14):142301, 2015.
- [51] M. Csanad. Measurement and analysis of two- and three-particle correlations. Nucl. Phys., A774:611–614, 2006.
- [52] Tamas Csorgo. Critical Opalescence: An Optical Signature for a QCD Critical Point. PoS, CPOD2009:035, 2009.
- [53] L. Adamczyk et al. $\Lambda\Lambda$ Correlation Function in Au+Au collisions at $\sqrt{s_{NN}} = 200$ GeV. Phys. Rev. Lett., 114(2):022301, 2015.
- [54] L. Adamczyk et al. Beam-Energy Dependence of the Directed Flow of Protons, Antiprotons, and Pions in Au+Au Collisions. Phys. Rev. Lett., 112(16):162301, 2014.
- [55] Dirk H. Rischke, Yaris Pursun, Joachim A. Maruhn, Horst Stoecker, and Walter Greiner. The Phase transition to the quark - gluon plasma and its effects on hydrodynamic flow. Heavy Ion Phys., 1:309–322, 1995.
- [56] M. Isse, A. Ohnishi, N. Otuka, P. K. Sahu, and Y. Nara. Mean-field effects on collective flows in high-energy heavy-ion collisions from AGS to SPS energies. Phys. Rev., C72:064908, 2005.
- [57] Yasushi Nara, Akira Ohnishi, and Horst Stoecker. Directed flow as a signature of the softest point of the equation of state in QCD matter. arXiv:1601.07692, 2016.
- [58] Md. Nasim, Lokesh Kumar, Pawan Kumar Netrakanti, and Bedangadas Mohanty. Energy dependence of elliptic flow from heavy-ion collision models. Phys. Rev. C, 82:054908, Nov 2010.
- [59] R. J. Fries, Berndt Muller, C. Nonaka, and S. A. Bass. Hadron production in heavy ion collisions: Fragmentation and recombination from a dense parton phase. Phys. Rev., C68:044902, 2003.
- [60] L. Adamczyk et al. Observation of an Energy-Dependent Difference in Elliptic Flow between Particles and Antiparticles in Relativistic Heavy Ion Collisions. Phys. Rev. Lett., 110(14):142301, 2013.
- [61] Pawel Danielewicz, Roy Lacey, and William G. Lynch. Determination of the equation of state of dense matter. Science, 298:1592–1596, 2002.
- [62] V. Skokov, A. Yu. Illarionov, and V. Toneev. Estimate of the magnetic field strength in heavy-ion collisions. Int. J. Mod. Phys., A24:5925–5932, 2009.

- [63] Kirill Tuchin. Particle production in strong electromagnetic fields in relativistic heavy-ion collisions. Adv. High Energy Phys., 2013:490495, 2013.
- [64] Dmitri E. Kharzeev, Larry D. McLerran, and Harmen J. Warringa. The Effects of topological charge change in heavy ion collisions: 'Event by event P and CP violation'. Nucl. Phys., A803:227–253, 2008.
- [65] Sergei A. Voloshin. Parity violation in hot qcd: How to detect it. Phys. Rev. C, 70:057901, Nov 2004.
- [66] B. I. Abelev et al. Observation of charge-dependent azimuthal correlations and possible local strong parity violation in heavy-ion collisions. Phys. Rev. C, 81:054908, May 2010.
- [67] B. I. Abelev et al. Azimuthal charged-particle correlations and possible local strong parity violation. Phys. Rev. Lett., 103:251601, Dec 2009.
- [68] Yannis Burnier, Dmitri E. Kharzeev, Jinfeng Liao, and Ho-Ung Yee. Chiral magnetic wave at finite baryon density and the electric quadrupole moment of the quark-gluon plasma. Phys. Rev. Lett., 107:052303, Jul 2011.
- [69] Dmitri E. Kharzeev and Dam T. Son. Testing the chiral magnetic and chiral vortical effects in heavy ion collisions. Phys. Rev. Lett., 106:062301, Feb 2011.
- [70] L. Adamczyk et al. Beam-energy dependence of charge separation along the magnetic field in Au + Au collisions at rhic. Phys. Rev. Lett., 113:052302, Jul 2014.
- [71] L. Adamczyk et al. Observation of charge asymmetry dependence of pion elliptic flow and the possible chiral magnetic wave in heavy-ion collisions. Phys. Rev. Lett., 114:252302, Jun 2015.
- [72] B. Abelev et al. Charge separation relative to the reaction plane in pb-pb collisions at $\sqrt{s_{NN}}=2.76$ TeV. Phys. Rev. Lett., 110:012301, Jan 2013.
- [73] Aaron Park, Philipp Gubler, Masayasu Harada, Su Houng Lee, Chiho Nonaka, and Woosung Park. Mass of heavy-light mesons in a constituent quark picture with partially restored chiral symmetry. Phys. Rev., D93(5):054035, 2016.
- [74] T. O. Yamamoto et al. Observation of Spin-Dependent Charge Symmetry Breaking in ΛN Interaction: Gamma-Ray Spectroscopy of ${}^4_{\Lambda}\text{He}$. Phys. Rev. Lett., 115(22):222501, 2015.
- [75] T. Gogami et al. High resolution spectroscopic study of ${}^1_0\Lambda\text{Be}$. Phys. Rev., C93(3):034314, 2016.
- [76] C. Rappold et al. Search for evidence of ${}^3_{\Lambda}n$ by observing $d + \pi^-$ and $t + \pi^-$ final states in the reaction of ${}^6\text{Li} + {}^{12}\text{C}$ at 2A GeV. Phys. Rev., C88(4):041001, 2013.

- [77] Yudai Ichikawa et al. Observation of the " K^-pp "-like structure in the $d(\pi^+, K^+)$ reaction at 1.69 GeV/ c . Prog. Theor. Exp. Phys., 2015(2):021D01, 2015.
- [78] T. Hashimoto et al. Search for the deeply bound K^-pp state from the semi-inclusive forward-neutron spectrum in the in-flight K^- reaction on helium-3. Prog. Theor. Exp. Phys., 2015(6):061D01, 2014.
- [79] Y. Sada et al. Structure near K^-+p+p threshold in the in-flight ${}^3\text{He}(K^-, \Lambda p)n$ reaction. arXiv:1601.06876, 2016.
- [80] Toshimitsu Yamazaki, Yoshinori Akaishi, and Maryam Hassanvand. New Way to Produce Dense Double-Antikaonic Dibaryon System, $\bar{K}\bar{K}NN$, through $\Lambda(1405)$ -Doorway Sticking in $p+p$ Collisions. Proc. Japan Acad. A Math. Sci., B87:362–370, 2011.
- [81] H. Noumi. Spectroscopic study of hyperon resonances below $\bar{K}N$ threshold via the (K^-, n) reaction on Deuteron. Proposal for J-PARC E31.
- [82] K. Shirotori et al. Search for the Θ^+ pentaquark via the $\pi^-p \rightarrow K^-X$ reaction at 1.92 GeV/ c . Phys. Rev. Lett., 109:132002, 2012.
- [83] M. Moritsu et al. High-resolution search for the Θ^+ pentaquark via a pion-induced reaction at J-PARC. Phys. Rev., C90(3):035205, 2014.
- [84] J.K. Ahn and K. Imai. Search for H-Dibaryon with a Large Acceptance Hyperon Spectrometer. Proposal for E42.
- [85] P. Adlarson et al. Evidence for a New Resonance from Polarized Neutron-Proton Scattering. Phys. Rev. Lett., 112(20):202301, 2014.
- [86] Faisal Etminan, Hidekatsu Nemura, Sinya Aoki, Takumi Doi, Tetsuo Hatsuda, Yoichi Ikeda, Takashi Inoue, Noriyoshi Ishii, Keiko Murano, and Kenji Sasaki. Spin-2 $N\Omega$ dibaryon from Lattice QCD. Nucl. Phys., A928:89–98, 2014.
- [87] S. Yokkaichi et al. Proposal Electron pair spectrometer at the J-PARC 50-GeV PS to explore the chiral symmetry in QCD, 2006. Proposal for J-PARC E16.
- [88] Edward Farhi and R. L. Jaffe. Strange Matter. Phys. Rev., D30:2379, 1984.
- [89] A. Andronic, P. Braun-Munzinger, J. Stachel, and H. Stocker. Production of light nuclei, hypernuclei and their antiparticles in relativistic nuclear collisions. Phys. Lett., B697:203–207, 2011.
- [90] A. J. Baltz, C. B. Dover, S. H. Kahana, Y. Pang, T. J. Schlagel, and E. Schneidermann. Strange cluster formation in relativistic heavy ion collisions. Phys. Lett., B325:7–12, 1994.
- [91] K. Kisamori et al. Candidate Resonant Tetraneutron State Populated by the ${}^4\text{He}({}^8\text{He}, {}^8\text{Be})$ Reaction. Phys. Rev. Lett., 116(5):052501, 2016.

- [92] Jean-Marc Richard, Qian Wang, and Qiang Zhao. Lightest neutral hypernuclei with strangeness 1 and 2. Phys. Rev., C91(1):014003, 2015.
- [93] E. Hiyama, S. Ohnishi, B. F. Gibson, and Th. A. Rijken. Three-body structure of the $nn\Lambda$ system with $\Lambda N - \Sigma N$ coupling. Phys. Rev., C89(6):061302, 2014.
- [94] A. R. Bodmer. Collapsed nuclei. Phys. Rev., D4:1601–1606, 1971.
- [95] Edward Witten. Cosmic Separation of Phases. Phys. Rev., D30:272–285, 1984.
- [96] J. Sandweiss. Overview of strangelet searches and Alpha Magnetic Spectrometer: When will we stop searching? J. Phys., G30:S51–S59, 2004.
- [97] Z. T. Lu, R. J. Holt, P. Mueller, T. P. O’Connor, J. P. Schiffer, and L. B. Wang. Searches for stable strangelets in ordinary matter: Overview and a recent example. Nucl. Phys., A754:361–368, 2005.
- [98] A. Rusek et al. Strangelet search and light nucleus production in relativistic Si + Pt and Au + Pt collisions. Phys. Rev., C54:15–19, 1996.
- [99] R. Arsenescu et al. The NA52 strangelet search. J. Phys., G27:487–493, 2001.
- [100] B. I. Abelev et al. Strangelet search at RHIC. Phys. Rev., C76:011901, 2007.
- [101] A. Andronic, P. Braun-Munzinger, and K. Redlich. Statistical production of antikaon nuclear bound states in heavy ion collisions. Nucl. Phys., A765:211–225, 2006.
- [102] Tadafumi Kishimoto. Kaonic nuclei excited by the (K^-, N) reaction. Phys. Rev. Lett., 83:4701–4704, 1999.
- [103] Yoshinori Akaishi and Toshimitsu Yamazaki. Nuclear anti-K bound states in light nuclei. Phys. Rev., C65:044005, 2002.
- [104] T. Yamazaki and Y. Akaishi. (K^-, π^-) production of nuclear anti-K bound states in proton-rich systems via Λ^* doorways. Phys. Lett., B535:70–76, 2002.
- [105] Sungtae Cho et al. Multi-quark hadrons from Heavy Ion Collisions. Phys. Rev. Lett., 106:212001, 2011.
- [106] Sungtae Cho et al. Studying Exotic Hadrons in Heavy Ion Collisions. Phys. Rev., C84:064910, 2011.
- [107] A. Ohnishi et al. Exotic hadrons and hadron-hadron interactions in heavy ion collisions. Nucl. Phys., A914:377–386, 2013.
- [108] J-PARC home page. <http://j-parc.jp>.
- [109] Y. Yamazaki, K. Hasegawa, M. Ikegami, Y. Irie, T. Kato, H. Kobayashi, S. Machida, Y. Mori, F. Noda, H. Suzuki, et al. Accelerator technical design report for J-PARC. 2003.

- [110] Hideaki Hotchi. Recent Progress of J-PARC RCS Beam Commissioning - Toward Realizing the 1-MW Output Beam Power. In Proceedings, 6th International Particle Accelerator Conference (IPAC 2015), page TUBB3, 2015.
- [111] J. A. Holmes, V. Danilov, J. Galambos, A. Shishlo, S. Cousineau, W. Chou, Leo P. Michelotti, F. Ostiguy, and J. Wei. ORBIT: Beam dynamics calculations for high-intensity rings. In Proceedings, 8th European Conference, EPAC 2002, Paris, France, June 3-7, 2002, pages 1022–1024, 2002.
- [112] Pranab Saha, Hiroyuki Harada, Naoki Hayashi, Hideaki Hotchi, Yoshihiro Shobuda, Fumihiko Tamura, and Masanobu Yamamoto. Comparison between Measurements and Orbit Code Simulations for Beam Instabilities due to Kicker Impedance in the 3-GeV RCS of J-PARC. In Proceedings, 5th International Particle Accelerator Conference (IPAC 2014), page TUPRI051, 2014.
- [113] L. J. Laslett. On Intensity Limitations Imposed by Transverse Space-Charge Effects in Circular Particle Accelerators. eConf, C630610:324, 1963.
- [114] V.D. Kekelidze et al. Prospects for the dense baryonic matter research at NICA. In Proceedings, Quark Matter 2015, 2015. the J-PARC point was added by H. Sako.
- [115] M. Gazdzicki, Z. Fedor, and G Vesztegombi. Study of Hadron Production in Hadron-Nucleus and Nucleus-Nucleus Collisions at the CERN SPS, 2006. Proposal for NA61/SHINE.
- [116] L. Ahle et al. Anti-proton production in Au + Au collisions at 11.7-A-GeV/c. Phys. Rev. Lett., 81:2650–2654, 1998.
- [117] P. Braun-Munzinger and J. Stachel. Production of strange clusters and strange matter in nucleus-nucleus collisions at the AGS. J. Phys., G21:L17–L20, 1995.
- [118] A. Laso Garcia, M. Kaspar, B. Kampfer, R. Kotte, L. Naumann, et al. Extreme high-rate capable timing resistive plate chambers with ceramic electrodes. JINST, 7:P10012, 2012.
- [119] CLAS12 Collaboration. CLAS12 Technical Design Report, Jul 2008. <https://www.jlab.org/Hall-B/clas12.tdr.pdf>.
- [120] A. Taketani. Silicon vertex tracker for PHENIX detector at the central rapidity region. Nucl. Instrum. Meth., A541:137–143, 2005.
- [121] B Abelev et al. Technical Design Report for the Upgrade of the ALICE Inner Tracking System. J. Phys., G41:087002, 2014.

- [122] Yusuke Komatsu et al. Development of the GEM tracker for the J-PARC E16 experiment. Nucl. Instrum. Meth., A732:241–244, 2013.
- [123] D. Ryckbosch. The HERMES RICH detector. Nucl. Instrum. Meth., A433:98–103, 1999.
- [124] K. Zeitelhack et al. The HADES RICH detector. Nucl. Instrum. Meth., A433:201–206, 1999.
- [125] S. An, Y. K. Jo, J. S. Kim, M. M. Kim, D. Hatzifotiadou, M. C. S. Williams, A. Zichichi, and R. Zuyeuski. A 20-ps timing device: A Multigap Resistive Plate Chamber with 24 gas gaps. Nucl. Instrum. Meth., A594:39–43, 2008.
- [126] T. Nonaka. Master’s thesis (in japanese). Master’s thesis, University of Tsukuba, 2014. ”https://dl.dropboxusercontent.com/u/70486402/2015/to_Sako_san/m_thesis_nonaka.pdf”.
- [127] A. Lebedev et al. Comparison of π^0 and eta spectrum from S + Au collisions at 200-GeV/c. Nucl. Phys., A566:355C–358C, 1994.
- [128] R. Debbe, C. Muntz, and J. B. Cumming. A high-resolution quartz Cherenkov detector for relativistic heavy ion beams. Nucl. Instrum. Meth., A403:256–262, 1998.
- [129] Sergei A. Voloshin. Testing the Chiral Magnetic Effect with Central U+U collisions. Phys. Rev. Lett., 105:172301, 2010.
- [130] Ante Bilandzic, Raimond Snellings, and Sergei Voloshin. Flow analysis with cumulants: Direct calculations. Phys. Rev., C83:044913, 2011.
- [131] M. M. Aggarwal et al. Observation of direct photons in central 158-A-GeV $^{208}\text{Pb} + ^{208}\text{Pb}$ collisions. Phys. Rev. Lett., 85:3595–3599, 2000.
- [132] P Buncic, M Krzewicki, and P Vande Vyvre. Technical Design Report for the Upgrade of the Online-Offline Computing System, Apr 2015. <https://cds.cern.ch/record/2011297>.
- [133] P Antonioli, A Kluge, and W Riegler. Upgrade of the ALICE Readout & Trigger System, Sep 2013. <https://cds.cern.ch/record/1603472>.
- [134] K. A. Olive et al. Review of Particle Physics. Chin. Phys., C38:090001, 2014.
- [135] J-PARC-HI White Paper. <http://asrc.jaea.go.jp/soshiki/gr/hadron/jparc-hi/index.html>.
- [136] H. Noumi. Charmed Baryon Spectroscopy via the (π, D) reaction. Proposal for J-PARC E50.